In-Situ Real-Time Solids Content Measurement of Settling Oil Sands Tailings Based on a Light Scattering Technique

by

Jiangwen Zhang

A thesis submitted in partial fulfillment of the requirements for the degree of

Master of Science

in

Photonics and Plasmas

Department of Electrical and Computer Engineering
University of Alberta

Abstract

Subsurface solids content measurement of oil sands tailings ponds is essential for tailings management and land reclamation activities. Currently, solids content is primarily measured by manual sampling and offline analytical methods. Light scattering can be used to determine particle sizes and concentration in solutions, which can be an alternative technique for solids content measurement. The focus of this thesis is to develop an in-situ subsurface solids content monitoring system based on light scattering technique to monitor the settling process and solids concentration of FFT (Fluid Fine Tailings) in oil sands tailings ponds at different depths.

An optical sensor prototype consisting of laser diodes and photodiodes was constructed to conduct experiment using a lab-scale settling tank with both visible (405nm & 658nm) and near-infrared (980nm & 1550nm) wavelengths. The setup was used to determine the settling process. Kaolin was used as a model material as well as FFT samples with different solids concentrations were measured. Both visible and near-infrared wavelength results indicate that the scattered light signal decreased responding to the decrease in solids content.

Light scattering technique can provide relative changes in solids content but not the absolute solids content. Several calibration measurements were then conducted to convert the scattered light signal into absolute solids content. A ring setup and a calibration tank were built to conduct measurements for calibration. Because of the differences in power of laser diodes and the differences in sensitivity of photodiodes, correction factors were obtained to correct the calibration tank and settling tank results. Calibration functions were obtained to convert the scattered light signal into

absolute sample concentration in weight percent. With a proper calibration procedure, the light scattering technique can be used to determine solids content with good sensitivity of 1 to 2.5 weight percent in different solids content ranges. A gamma-ray sensor was also developed in our research group to measure solids content. The results of solids content measurement using both optical and gamma-ray sensor agree well in the settling tank experiments. The good agreement suggested that the gamma-ray sensor can be used to provide in-situ calibration for the optical sensor.

Preface

I was responsible for optical sensor system design and components testing shown in chapter 2. Allen Feng and Dr. M.Zahurul Islam assisted with the optical system design. Allen Feng and Dr. Tulika Srivastava assisted with the components testing. The design of experiment setups was done by the project group.

The wavelength optimization of chapter3 was published as Tulika Srivastava, Jiangwen Zhang, Bo Yu, Abu Junaid, Andrea Sedgwick, Robert Fedosejevs, Manisha Gupta, Ying Tsui,"A real time in situ light-scattering technique for tailings solids content measurement: NIR versus visible wavelengths". Dr.Tulika Srivastava was responsible for data collection and results analysis and all authors contributed to manuscript editing. Additional settling tank experiments includes sample preparation, data collection and results analysis are my original work. Dr.Tulika Srivastava assisted with the settling tank experiment results analysis.

Light scattering measurements with different solids content concentration at backscatter angle of 20°, shown in chapter 4, were done by Dr.Tulika Srivastava. The data collection and analysis of gamma-ray sensor in settling tank experiments and gamma-ray sensor calibration were done by Bo Yu. Dr. Tulika Srivastava assisted with the calibration tank experiments data collection and analysis. Additional experiments, calculations, and results analysis in chapter 4 are my original work.

In Chapter 5, experiments and results analysis of optical window fouling were done by Xiaoxuan Liu and Dr. Tulika Srivastava. Gamma-ray sensor design was done by Bo Yu. Dr. Robert Fedosejevs assisted with the amplifier circuit design for fiber optic system. Testing and results analysis of the fiber optic system are my original work.

The experiment setup, method, and data collection of power and communication unit were done by Capstone project group includes Allen Feng, Junlong Pan, Shyam Patel and Dillon Sweene. Dr. Robert Fedosejevs, Dr. Manisha Gupta, and Dr. Ying Tsui were involved in the conception of the project and are supervisors.

Acknowledgments

First and foremost, I appreciate Professor Ying Tsui and Professor Manisha Gupta for offering me the opportunity to study in University of Alberta and join this interesting project. Thanks to Professor Rebort Fedosejevs and Dr.M.Zahurul Islam for all the suggestions and instructions. I also thanks to the help from my lab mates: Dr. Tulika Srivastava, Allen Feng, Bo Yu, Xiaoxuan Liu, Wei Wang and Dr. Talwinder Kaur Sraw.

Thank you to Dr. Junaid and Andrea for providing the samples, and sharing ideas and techniques in this project.

Most of the experimental setups were built by the ECE machine shop. Thank you to all machinists for your patience, helpful discussions and outstanding work.

Finally, I would like to thank my family and friends, especially my boyfriend, Xinze Lyu, for their endless love and support and standing by me during this difficult time.

Financial support of this work was provided by the Natural Sciences and Engineering Research Council of Canada, the Institute of Oil Sands Innovation, and the Canada's Oil Sands Innovation Alliance.

Table of Contents

1 Introduction **1**

1.1 Tailing ponds 2

1.2 Existed techniques for solids content measurement in oil sands 3

1.2.1 Standard laboratory methods 3

1.2.2 Real time method 5

1.3 Light scattering technique 7

1.4 Main components of the optical solids content sensor 10

1.4.1 Laser diode 10

1.4.2 Photodiode 10

1.5 Description of the project 11

2 Experimental setup and optical sensor system **12**

2.1 Ring setup 12

2.2 Settling tank setup 14

2.3 Calibration tank 14

2.4 Optical sensor system 16

2.4.1 Previous work 16

2.4.2 Overall design 17

2.4.3 Laser diode system 17

2.4.4 Photodiode system 29

2.4.5 Cost of the optical sensor system 32

2.5 Summary 32

3 Settling Tank Studies **34**

3.1 Slurry samples 34

3.1.1 Kaolin sample 34

3.1.2 FFT sample 35

3.2 Visible wavelength (658nm & 405nm) experimental results and discussions 35

3.2.1 Kaolin sample experiment results and discussions 36

3.2.2 FFT sample experiment results and discussions 38

3.2.3 Comparison with previous work 41

3.3 Near-infrared wavelength (980nm & 1550nm) experimental results and discussions 43

3.3.1 Wavelength optimization 43

3.3.2 Kaolin sample experiment results and discussions 48

3.3.3 FFT sample experiment results and discussions 49

4 Calibration **58**

4.1 Calibrtion ring 58

4.1.1 Angular distribution of laser scattered light intensity measurements 59

4.1.2 Light scattering measurements with different solids content at backscattering angle of 20° 61

4.2 Correction factors for settling tank and calibration tank setups 64

4.2.1 LD power test 64

4.2.2 PD sensitivity test 65

4.2.3 Teflon test 68

4.2.4 Correction factors 69

4.2.5 Correction for FFT-C sample settling experiment results . . . 73

4.3 Calibration of the optical sensor 75

4.3.1 Calibration tank measurements 75
4.3.2 Calibration functions 76
4.3.3 Comparison of calibration tank and calibration ring results . . 78
4.3.4 Application of 1550nm calibration function in the FFT-C sample settling experiment results 80
4.4 Sensitivity of optical measurements 84
4.5 Correlation of gamma ray and optical 1550nm measurements 86
4.6 Summary 91

5 Description of whole project 92
5.1 Optical window fouling 92
5.2 Calibration 94
5.3 Preliminary fiber optic system 95
5.4 Power and Communication 96
5.5 Full design of the real-time in-situ subsurface solids contents analyzer 99

6 Conclusion and Future Directions 101
6.1 Summary 101
6.2 Future Considerations 102

Bibliography 104

Appendix A: Codes 108
A.1 Arduino code for signal channel selecting 108
A.2 Matlab code for data processing 110

Appendix B: Calibration tank results of circuit2 112

List of Tables

2.1 The four types of laser diodes used in the project and select properties 18

2.2 Comparison of laser diode characteristics before and after soldering . 26

2.3 Price of components used for the optical instrument 32

3.1 FFT samples used in the thesis 35

4.1 Results of LDs power test: (a) 1550nm, (b) 980nm. Power test 1 was conducted before FFT-C sample settling tank measurement and power test 2 was conducted before Teflon test. 66

4.2 Results of 6 levels PD sensitivity test using 1550nm laser diode with output power of 2.5mW 68

4.3 Results of Teflon test using setup shown in Figure 4.5 with 1550nm and 980nm LD 70

4.4 LD correction factors of (a) 1550nm and (b) 980nm from level 1 to 6 using data from table4.1 71

4.5 Teflon test results corrected by LD and PD correction factors: (a) 1550nm results, (b) 980nm results. 72

4.6 Growth percentage between two concentrations of FFT-C sample 1550nm calibration results. 77

4.7 The corresponding PD signal change per 1wt% in different solids content range. 85

4.8 1550nm wavelength sensitivity in different solids content range. 85

List of Figures

1.1 Tailings storage facility.[10] 2

1.2 A cross-sectional view of a tailings pond.[10] 3

1.3 Schematic of light scattering geometry. The scattering angle is measured with respect to the direction of unimpeded light. 8

2.1 Ring setup: (a) schematic showing the laser diode and one of the detectors at an angle from the laser axis. (b) picture of the ring setup. . 13

2.2 Settling tank setup (a) schematics of the settling column; (b) picture of the settling tank; (c) insertion column; (d) metal sensor tube. . . . 15

2.3 Picture of the calibration setup. The left picture shows the 3 litre volume tank with an insert tube. The right picture shows the 3 level optical sensors. 16

2.4 Block diagram for the overall circuit design. 18

2.5 Detailed laser diode circuit1 with all components. 19

2.6 Laser driver: (a) FL591FL[34] (b) MLD203P2E[35] 20

2.7 Laser diode current monitor circuits: (a) FL591FL laser driver[34] (b) MLD203P2E laser driver[35] 22

2.8 Constant power mode reliability test for 405nm, 658nm, 980nm and 1550nm LDs (a)results of 405nm LDs (b)results of 658nm LDs (c)results of 980nm LDs (d)results of 1550nm LDs. 23

2.9 LDs power measurement. Black symbols show 405nm LDs power, red symbols show 658nm LDs power, blue symbols show 980nm LDs power, and green symbols show 1550nm LDs power. 24
2.10 Laser diodes I-Power curve: (a)results of 405nm LDs (b)results of 658nm LDs (c)results of 980nm LDs (d)results of 1550nm LDs. 25
2.11 The change before and after adding the bypass capacitor 27
2.12 Improved laser diode system circuit2 : (a) 980nm laser diode system (b) 1550nm laser diode system. 28
2.13 MLD203P1E laser driver for 980nm laser diodes[36] 28
2.14 Photodiode biased circuit[37] 30
2.15 Photodiode responsivity: (a) SM05PD1A[37] (b) SM05PD5A[38] . . . 30
2.16 Relationship between laser diode operating current and photodiode signal: (a) SM05PD1A (b) SM05PD5A 31

3.1 Visible wavelengths (405nm & 658nm) LD water test in settling tank (a) extracted data (b) original data (photodiode signal versus time) . 36
3.2 Settling process correlate to the 658nm relative scattering signal changes in 15wt% Kaolin sample measurement 38
3.3 15wt% Kaolin sample with 600nm particle size settling tank experiments results: (a)658nm LDs 18-hour test, (b)405nm LDs 18-hour test, (c)658nm LDs 24-hour test, (d)405nm LDs 24-hour test. This measurement was conducted by circuit1. 39
3.4 18.2wt% and 21.7wt% FFT sample settling tank experiment results: (a)658nm LD 18.2wt% FFT test, (b)405nm LD 18.2wt% FFT test. This measurement was conducted by circuit1. 42
3.5 Water-solid position during the 18.2wt% FFT-B sample measurements. 658nm and 405nm LDs were used. 43

3.6 Measurement using 405nm laser diode at heights of 1 cm, 6cm, 11 cm and 17 cm from top respectively and measurement angle was at 20°. (a) Kaolin 33wt% starting solids content of hours elapsed versus relative signal strength. (b)TUT 35wt% starting solids content measurement.[6] 44

3.7 Relative change in light scattering intensity with the change in the solids content of (a) FFT-A diluted to different concentrations: (i) 405nm, 520nm and 658nm wavelengths results, (ii) 980nm, 1310nm and 1550nm wavelengths results. And (b) mixtures of FFT-A and FFT-B at different ratios. In each row the measurements had been shown for experiments conducted with: (i) visible wavelengths, and (ii) NIR wavelengths. The 0 wt% solids content in (a) represents distilled water used to test the background noise generated from the effect of the room light.[31] 46

3.8 Effects of bitumen fouling on the measurement: (a) visual observations of the bitumen-fouled cuvettes (b) relative change in the light scattering intensity for as prepared and one week old bitumen-fouled samples for 405 and 1550 nm wavelengths, and (c) absorption spectra of raw and cold washed FFT-E (inset: absorption spectra of water).[31] . . . 47

3.9 NIR wavelengths (980nm & 1550nm) water test results by circuit1. . 48

3.10 NIR wavelengths 15wt% 600nm Kaolin test results: (a) 1550nm (b) 980nm. This measurement was conducted by circuit1. 50

3.11 21.7wt% FFT-A sample experiment results: (a)1550nm, (b)980nm, (c)1550nm-level1 detail result, (d)1550nm-level2 detail result. This measurement was conducted by circuit1. 51

3.12 LDs current moinitor data in 21.7wt% FFT-A test: (a) 1550nm (b) 980nm 53

3.13 NIR wavelengths (980nm & 1550nm) water test results by circuit2. . 53

3.14 18.5wt% FFT sample experiment results: (a)1550nm, (b)980nm, (c)1550nm-level1&2 detail results, (d)980nm-level1 detail results, (e)980nm-level2 detail results. This measurement was conducted by circuit2. 54
3.15 LDs current moinitor data in 18.5wt% FFT-C test: (a) 1550nm (b) 980nm 56
3.16 The picture of the insertion tube after the two months 18wt% FFT-C sample settling experiment. 57

4.1 Light scattering signals from slurry samples and water as a function of angle: (a) 25wt% 600nm Kaolin sample (b) 25wt% FFT-D sample (c) water (0wt%). Measurements were conducted using 405nm, 658nm, 980nm and 1550nm LDs. 60
4.2 Light scattering signals from slurry samples as a function of angle: (a) 25wt% 600nm Kaolin sample (b) 25wt% FFT-D sample. The black dot lines are cos fit curve. Measurements were conducted by 405nm, 658nm, 980nm and 1550nm LDs. 62
4.3 Relative changes in light scattering intensity with the change in the solids content at 20° backscattering angle (a) 600nm Kaolin sample (b) FFT-A sample. Measurements were conducted by 405nm, 658nm, 980nm and 1550nm LDs. 63
4.4 Schematic diagram illustrates the PD sensitivity test setup with a reference PD and one pair of the LD-PD: (a) Side view of the setup, (b) Top view of the setup. 67
4.5 Teflon test setup: (a) picture of the overall setup, (b) schematic diagram illustrates the test setup for one of the LD-PD pairs. 69

4.6 Corrected settling tank experiments (a) 1550nm (b) 980nm. Original settling tank experiments data (c) 1550nm (d) 980nm. FFT-C sample with initial solids content of 18.5wt% was measured. The tables in the figures show the starting value of each level. 74
4.7 FFT-C sample calibration results measured at 20°backscatter angle using circuit2: (a)1550nm laser diode, (d)980nm laser diode. The results are raw data from calibration tank measurements. 77
4.8 Scattering signal as a function of solids content. (a) The black symbols are data from 1550nm and the black curve is the 2nd order polynomial fit. (b) The red symbols are data from 980nm and the red curve is the 2nd order polynomial fit. The experiments are done by calibration tank. 79
4.9 Comparison of calibration tank results curve and calibration ring results curve after normalization: (a) 1550nm, (b) 980nm. 81
4.10 Relationship between sample solids content in wt% and scattered light signal in volt for 1550nm. Obtained from 1550nm calibration function4.1. 82
4.11 Temporal evolution of solids content in FFT-C sample settling experiment. (a)1550nm-level1 (b)1550nm-level2 (c)1550nm-level3 (d)1550nm level4 to level6 84
4.12 Optical scattering (1550 nm) signal versus gamma-ray signal at a depth 6.5 cm (level2) from the initial water surface for a 15wt% Kaolin sample.[41] 87
4.13 Optical scattering (1550nm) signal versus gamma-ray transmission signal at 2 different depths in the settling tank: (a) level2 (6.5cm below the water surface) and (b) level3 (11cm below the water surface). The settling tank was initially filled with 18.5 wt% FFT-C sample. . . . 88
4.14 Gamma ray calibration curve obtained by measuring different wt% of FFT-B for 10 minutes (* 5 times) in calibration tank with the same tube and distance as the settling tank.[41] 89

4.15 Temporal evolution of solids content varies for FFT-C sample at: (a)level2 (6.5cm below the water surface), (b)level3 (11cm below the water surface). The black symbols represent results calculated by the 1550nm calibration function and red symbol represent results calculated by the gamma-ray calibration function. 90

5.1 Effects of bitumen fouling on the measurement: (a) absorption spectra of raw and cold washed FFT-A, (b) (inset figure) absorption spectra of water).[31] 93

5.2 1550nm photos of: (a) plexiglass, (b) glass, (c) sapphire. All the three materials were immersed in the FFT-B sample for 3 months.[41] . . . 94

5.3 Simplistic diagram of the concept of the gamma-ray method. 96

5.4 Optical fiber initial test with 7mW 658nm LD and Teflon slice: (a) Experimental setup, (b) results of comparison between the signal received through optical fiber and the signal directly captured by PD, (c) 10 times amplifier circuit 97

5.5 System block diagram for power and communications unit. This shows the connection of the entire system and its various components.[42] . 98

5.6 Cartoon illustrating the overall concept for the subsurface solids content analyzer. The main components are (i) the gamma-ray system with gamma ray sources (blue objects in the insert tube) and gamma ray detectors (green objects in the insert tube); (ii) the optical system with laser diodes with different wavelengths (red and orange objects in the insert tube) and photodiodes (black objects in the insert tube); (iii) optical and gamma ray circuits above the tailing pond surface; and (iiii) the communication and power unit above the tailing pond surface. 100

B.1 FFT-C sample calibration results measured at 20°backscatter angle using circuit1 with 1550nm laser diode. 112

Abbreviations & Acronyms

CNRL Canadian Natural Resources.

CW Cold-washed.

DPHP Dual Probe Heat Pulse.

FBRM Focused Beam Reflectance Measurement.

FFT Fluid Fine Tailings.

GEANT4 GEometry ANd Tracking.

HTML HyperText Markup Language.

LD Laser diode.

MFT Mature Fine Tailings.

NIR Near-infrared.

NMR Nuclear Magnetic Resonance.

PD Photodiode.

PHP Hypertext Preprocessor.

TUT Thickened Underflow Tailings.

wt% Weight percent.

XRF X-ray fluorescence.

Chapter 1

Introduction

Canada has the world's largest oil sands reserves. Crude oil extraction through oil sands mining is one of Canada's largest industries and the key driver of the economy. Canada's oil sands reserves, mainly located in Alberta, are the world's third largest oil reserves, accounting for 9.6 percent of total proven reserves in the world.[1][2] The total in-place bitumen reserves are estimated to be over 1.7 trillion barrels, of which approximately 165 billion barrels can be recovered using existing technology.[1][3] However, some environmental issues arise in crude oil extraction. The extraction of bitumen from oil sands requires a significant amount of water, resulting in a large volume of tailings that end up stored in tailings ponds. Water recycling is critical because continuous freshwater intake is environmentally costly, and the primary challenge for the industry is the temporary storage and processing of tailings, as well as the reclamation of the tailings ponds.[4][5][6] By the end of 2013, the total amount of Fluid Fine Tailings (FFT) stored in tailings ponds in Canada was approximately 975.6 mm^3.[1] Currently, approximately 75% of the total processed water can be recycled, with the remaining 25% continued accumulating in tailings ponds. This equates to an usage of approximately 2.6 barrels of non-saline freshwater for every barrel of oil produced.[4] It would take decades for the stored tailings slurry to settle naturally[7], and after tailings settled, water in tailings ponds can then be recycled. Therefore, managing the oil sands tailings, processing them, and finally reclaiming

the tailings ponds are major challenges. The solids content is an essential parameter for monitoring and managing tailings storage, settling, treatment, dredging, and transportation. There is currently no non-contact in-situ instrument or technique that can monitor the settling process and solids concentration at different depths in tailings ponds in real time effectively, safely and economically. The light scattering technique was chosen in this thesis because it has the advantages of being safe, clean, non-destructive and relatively low cost. In this thesis, the development of an in-situ, real-time, low-cost and safe optical sensor for solids content measurement with multiple depths monitor capability based on light scattering technique will be described. The next several sections in this chapter will discuss the details of tailings ponds, existing technologies for solids content measurement and their gaps, light scattering technique, major components, and a description of this project.

1.1 Tailing ponds

Tailings are slurry mixtures of sand, silt, clay (37%) and water (58%-62%) which contain small amounts of residual bitumen (1%-5%) from the extraction process. The tailings that remain in the ponds following water recovery, generally known as Fluid Fine Tailings (FFT), can take decades to settle.[8][6][9] Figure 1.1 shows the tailings storage facility[10].

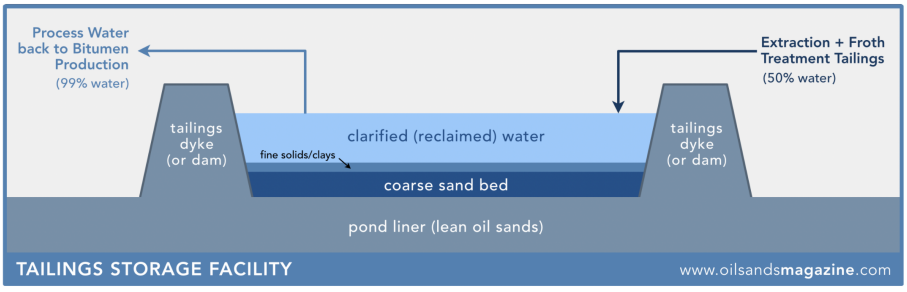

Figure 1.1: Tailings storage facility.[10]

One challenge with tailings treatment and management is that the composition of tailings can vary substantially at different positions and depths, even in the same

tailing ponds. A cross-sectional view of a tailings pond is shown in Figure 1.2[10]. The fine solids that remain suspended in the water are referred to as Fine Fluid Tailings (FFT). FFT eventually degrades into Mature Fine Tailings (MFT) if left undisturbed for several years. It has been studied that at different depths, the solids content, bitumen content, and grain size distribution are all different.[11] Therefore, there are needs to make real-time in-situ measurements of the solids content of the oil sands tailings at different depths and locations to improve operations in managing the oil sands tailings ponds.

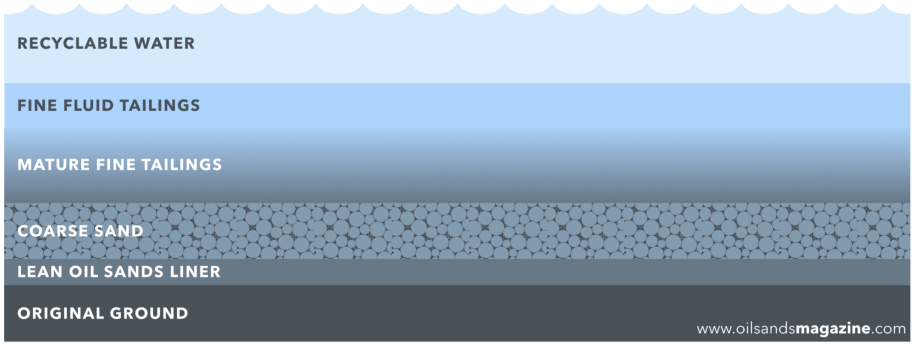

Figure 1.2: A cross-sectional view of a tailings pond.[10]

1.2 Existed techniques for solids content measurement in oil sands

1.2.1 Standard laboratory methods

Several laboratory methods are currently used to determine the solids content in samples from oil sands tailing ponds.

1.2.1.1 Gravimetric method[12]

Gravimetric method determines the total solids of a slurry sample by weighing the sample before and after all the water has been evaporated.

1.2.1.2 Dean-Stark method[13]

The Dean-Stark method can determine solids content in oil sands by separating the solids of the original sample from the organics and water using the Dean-Stark apparatus. This method is time-consuming and generates waste that contains organic solvent.

1.2.1.3 X-ray based method[14]

A method based on X-ray fluorescence (XRF) spectroscopy was proposed by Xu Z. et al[14]. to measure potassium content could be used to determine the content of fines in oil sands samples. The XRF method determines the elemental composition by detecting the fluorescence X-ray emission of the sample when it is excited by an X-ray source. The XRF method is quick and nondestructive. However, high-voltage X-ray tube sources and high-resolution pulse height counting detectors are used, and the tests are typically performed in laboratories.

1.2.1.4 Gamma ray based method[15]

The dry bulk density, which is the dry solid mass in a unit volume of MFT, can be measured by the Gamma Ray Attenuation method to determine the solids content in oil sands. The gamma-ray intensity propagates through a sample with certain thickness and decreases exponentially with its mass density. A method was proposed by Costa et al[15]. for soil bulk density evaluation. However, typically the radioactive sources used are strong, leading to a system being expensive and requiring a high level of technical supervision, which is unsuitable for in-situ applications in tailings ponds due to cost and safety concerns.

Our group has developed a safe solids content measurement method [16] for in-situ real-time solids content measurement in tailing ponds based on radioactive sources with relatively weak strength. The strength used is below licensing limit similar to household smoke detector devices.

1.2.1.5 Neutron based method[17]

Pulsed neutron sources have also been proposed to measure bulk density. This technique is based on gamma scattering signatures induced by neutrons interacting with the surrounding solid media. However, the sources and detectors are expensive and complicated.

1.2.2 Real time method

In addition to the optical light scattering method described in this thesis, several methods can potentially be used for in-situ measurement.

1.2.2.1 Focused Beam Reflectance method[18][19]

Focused Beam Reflectance Measurement (FBRM) is an inline and real-time technology widely and commercially used to analyze particle size and count in slurry samples. The FBRM probe consists a laser that is focused in a focal plane outside its sapphire window. The laser rotates at a fixed speed, and the particles pass the focal plane backscatter the laser light. The particles can be counted by obtained backscattering signal. The FBRM technology can only effectively detect solids content in MFT specimens with relatively low concentrations. The FBRM technology show higher variability when detecting slurry sample with solids content beyond 13mg/mL.

1.2.2.2 Nuclear Magnetic Resonance method[9]

The low-field nuclear magnetic resonance (NMR) bimodal compositional detection method proposed by S. C. Motta Cabrera et al[9]. can be used to measure the bitumen and water contents in the oil sands. Furthermore, the spectra could be used to deduce the solids content in the samples. An NMR instrument polarises the protons in a fluid (oil or water) using magnetic fields and measures the time it takes for the protons to return to equilibrium (known as relaxation time). They produced a spectrum that shows the amplitude and relaxation time in relation to the quality and quantity of

the examined fluids (bitumen and water). The solids content then can be calculated using the contents of water and bitumen. The results can be obtained in 15 minutes and it can be considered as a potential application for determining the composition of tailings streams in real time. However, this technology is not specifically designed to monitor solids content and the minimal bitumen detection limit is 0.6g causing inaccurate solids content speculation.

1.2.2.3 Dual Probe Heat Pulse Method[20]

The solids percentage of Mature Fine Tailings (MFT) can be measured accurately by Dual Probe Heat Pulse (DPHP) method proposed by Min Li et al[20]. The DPHP method can measure the solids content in MFT samples by determining their thermal properties using sensor probes. This method is low-cost, accurate, and automated. Theoretically, the setup can be installed at different locations and depths in the tailings ponds. However, the wire probes are in direct contact with the MFT samples, and corrosion can become a big issue during long-term measurements. And it will be challenging to detect the degree Celsius change in the field rather than in laboratories to determine the thermal properties, and the implementation will be difficult. Only MFT samples with 20wt% to 70wt% are measured in this study. Whether this method can be applied to MFT samples with solids content less than 20wt% is uncertain. The free convection in MFT suspensions with low solids concentration will affect the accuracy of the experiment. To date, only MFT samples with certain solids percentage were tested and no settling experiments have been done.

The laboratory methods require manual sampling from various tailing ponds and depths, which is time-consuming, onerous, and cannot function as in-situ instruments. More importantly, manual sampling is often unrepresentative and prone to error. In summary, there is currently no non-contact in-situ instrument or technique that can effectively, safely, and low-costly monitor the settling process and solids content of samples with high concentrations in real time. Therefore, the primary goal of the

whole research project is to create a technology that can provide in-situ subsurface solids content analysis at various depths in tailings ponds in real time.

In this thesis, an optical sensor based on light scattering technique was developed to measure the settling process and solids content in oil sands tailings with an optimum laser wavelength chosen based on the effects of FFT variability and bitumen fouling. Light scattering technique has the advantages of being safe because we are only exposed to low-power laser light; clean because no by-products are produced in the measurement; and non-destructive because there is no need to destroy or disturb the sample. By design, it can be fully automated, transmit data online, and be available even in locations with harsh weather. A solids content sensor based on gamma-ray transmission was built by another graduate student in our research group to provide an absolute measurement of solids content at different depths for absolute calibration of the optical sensor system. With proper sample thickness and measurement time, comparable performance to existing techniques can be achieved by using low-level gamma-ray sources at a much lower cost and risks.[16]

1.3 Light scattering technique

Light scattering technique is used for a wide range of applications. The increased interest in its application is spreading beyond traditional areas like chemistry, biology, and physics [21] into new areas including health[22], food industry[23], and biomedical science[24]. Although light scattering technique is commercially used in industry for low concentration applications to determine particle size and concentration in solutions[25], it is a relatively new application in solids content measurement for oil sands tailings treatment.

When light passes through an atom that has no resonances at that energy, the electric field causes the oscillation of electron clouds around the atom. The light is elastically scattered when the oscillation occurs, causing re-emission with the same energy in a random direction.[26][27] The scattering angle is defined as the angle between the

vectors of incoming light and scattered light, as shown in Figure 1.3.

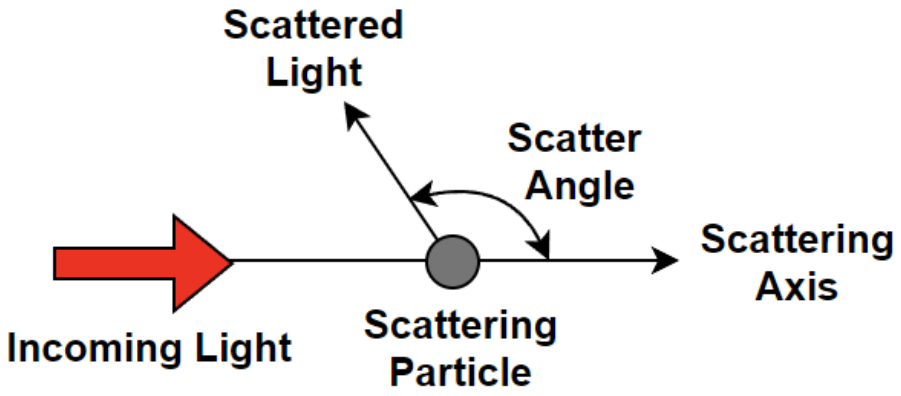

Figure 1.3: Schematic of light scattering geometry. The scattering angle is measured with respect to the direction of unimpeded light.

In our project, the scattering angle of interest is generally more than 90 degrees, known as backscattering. The oil sands samples are opaque due to their high solids concentration, hence backscattering is used. This also simplifies the device and operation, the laser and photodetector could be physically installed together, and no additional paraphernalia or alignment is required as in transmissive or absorptive measurements. However, the laser and detector must be configured to avoid specular reflection. The optimization of the backscattering angle was conducted and will be discussed in chapter4. Typically, more particles will scatter more light, which is the basis of how the solids content can be determined. Light scattering is complicated in dense samples by internal reflections and transmissions inside the particle and the interference of the light at the detector.[27]

The optical sensor system uses laser diodes as light sources and photodiodes as detectors for real-time in-situ measurement of solids content with no prior sample preparation. The amount of solids in tailings will be proportional to the scattered light intensity detected by the photodiode, and the relative change in scattering intensity will indicate the change in solids content at different depths. However, depending on the processing technique and features of the oil sands ores, tailings can have a wide

range of particle sizes and chemical compositions. Therefore, the choice of wavelength for solids content determination need to account for particle size and type of light scattering.

It is well known that the wavelength of incident light (λ) and particle size (φ) dictate the type of scattering. The three major regimes of light scattering are Rayleigh, Mie, and diffraction or geometric scattering. They are distinguished based on the wavelength to particle size ratio (λ/φ). Rayleigh scattering occurs when the particle diameter is much smaller than the excitation wavelength ($\lambda/\varphi>10$). When the particle size and wavelength of incident light are similar ($0.01>\lambda/\varphi<10$), Mie scattering occurs. Mie scattering can occur for arbitrary particle size, convergent to the limit of geometric optics for large particles, and is used mostly for spherical particle scattering systems. Geometric scattering occurs when the particle size is much larger than the excitation wavelength ($\lambda/\varphi>0.01$).[28][29] In tailing ponds, the particle size distribution can range from sub-micron to 100's of a micron. Particles with size $\varphi<44\mu$m are considered to be fine particles that are present in solids and clays that take significant time to settle. It has been reported that for solids content up to 55 wt%, the content of fine particles can range from 50% to 100%.[30] Therefore, significant light scattering will occur due to the large amount of fine particles in the oil sands tailings sample.

In this thesis, wavelengths ranging from visible wavelengths (405 nm and 658nm) to near-infrared wavelengths (980 nm and 1550nm) were used. Therefore, much of the scattering is in the geometric scattering regime and some of the scattering lies in the Mie scattering regime. Most of the wavelength optimization experiments were conducted by Dr.Tulika Srivastava in our research group. The results from the study indicated that the NIR wavelengths, especially 1550nm, can detect even small amount of solids content based on strong water absorption and also have the additional benefit of high transmission through bitumen coatings.[31]

1.4 Main components of the optical solids content sensor

The optical sensor system designed for real-time in-situ solids content measurement involves laser diodes as light sources and photodiodes as detectors. This section will introduce laser diode and photodiode, and the details of other components will discuss in chapter 2.

1.4.1 Laser diode

The commercial and industrial use of laser diodes has increased dramatically in recent years. Because of the optical properties, small size, and ruggedness of laser diodes, many new applications have been commercialized. These characteristics qualify the laser diodes for cable TV transmission, high definition television development, and medical applications. Considering their small size, laser diodes can produce a very high output. Today, laser diodes operating under continuous wave conditions in packages as small as a few cubic inches can produce hundreds of watts of power.[32] Another reason for choosing laser diodes as the light source is that they consume very little power compared to other types of lasers. Furthermore, laser diodes do not require fragile glass enclosures or mirror alignment because they are made of semiconductor materials. Therefore, laser diodes are robust enough to be used in harsh environments. The laser diodes used in this project are from Thorlabs due to their cost and compact form factor (5.6mm in diameter). As discussed in chapter 1.3, the chosen wavelengths are 405nm, 658nm, 980nm and 1550nm. The behavior of light scattering from slurry samples strongly depends on the wavelengths of the light.

1.4.2 Photodiode

The photodiode is a semiconductor device with a P-N junction that converts light into electrical current. A photodiode device is designed to operate under reverse bias. The photodiode is a high-quantum-efficiency, quick, highly linear device. Photodiodes

can be manufactured from materials such as Silicon, Germanium, Indium Gallium Arsenide etc. Using different materials, photodiodes will have different properties for wavelength range, high sensitivity, low noise levels, response speed, and cost savings. In this thesis, silicon photodiodes were used to measure light signal from visible range wavelengths (405nm and 658nm) LDs, while InGaAs photodiodes were chosen to measure light signal from NIR range wavelengths (980nm and 1550nm) LDs. These mounted photodiodes are from Thorlabs.

1.5 Description of the project

This thesis is focused on developing an inexpensive, efficient, safe, and dependable optical sensor to measure the solids content and monitor the settling of Fluid Fine Tailings in oil sands tailings ponds at different depths based on the light scattering technique. The technique involves laser diodes with different wavelengths (405nm, 658nm, 980nm and 1550nm) performing as light sources and photodiodes to detect the scattered light for real-time in-situ measurement of solids content with no need for prior sample preparation. The scattered light intensity detected by photodiodes is proportional to the amount of solids in tailings, and the relative change in scattering intensity provides information about the change in solids content at various depths. Once installed in the tailings ponds, it will require little maintenance.

Chapter 2 will introduce the detailed geometry of the experimental setups, preliminary tests, data processing method, and the light scattering sensor system. Chapter 3 will introduce the lab-scale settling tank studies. Chapter 4 will focus on the calibration methods. Chapter 5 will introduce the whole in-situ real-time subsurface solids content analyzer based on a hybrid of optical and safe gamma-ray methods with a communication and power unit above the tailing pond surface. Chapter 6 will give a summary of the current studies and proposes future directions.

Chapter 2

Experimental setup and optical sensor system

This chapter will introduce three different setups and an optical sensor system based on the light scattering technique designed to analyze solids content samples. A ring setup was designed to measure the angular distribution of backscattered light from the samples. A settling tank was designed to imitate the situation when the sensor system is submerged in a tailings pond. A calibration tank was developed for calibration. An optical sensor system prototype was developed to measure the relative change in the solids content at different depths.

2.1 Ring setup

In order to determine the optimum observation angle for the photodiodes and the relationship of the light scattering signal as a function of solids content, a ring setup was developed. The ring setup consists of a 24 cm polyvinyl chloride ring in diameter and 1.27 cm thick, which is shown in Fig 2.1. The hole for the laser diode with a particular wavelength is located at the 12 o'clock position in this figure. The laser light at a normal incident angle would go through the hole and focus on the sample. The sample would be placed in a cuvette and positioned at the center of the ring setup. Other holes were cut for photodiode from 10° to 90° both clockwise and counterclockwise. A beam dump was placed on the opposite side of the laser diode

to reduce background scattering light from the laser.

The light scattering intensity typically can be described by a $cos^n(\theta)$ law, where θ is the observation angle for light scattering measurement. The angle is defined respective to the laser propagation direction. The power law parameter n typical has a value between 1 to 2[6], which depends on the sample properties. When n = 1, the scattering light distribution is said to be Lambertian [33]. Angular measurements with several samples were conducted in this thesis, and they are reported in chapter 4. The backscattered light signal from the samples was measured at seven different angles from 10° to 80° incrementing by 10°. The optimum observation angle was chosen to be 20° which allows a high light backscattering signal with insignificant influence from the undesired specular reflection light[27].

This ring setup was also designed to conduct calibration measurements. The various solids content from 0 to around 40 wt% were prepared by diluting the sample with high concentration. In the calibration experiment, a photodiode was installed in the threaded hole at 20°. Results from this setup are reported in chapter 4.

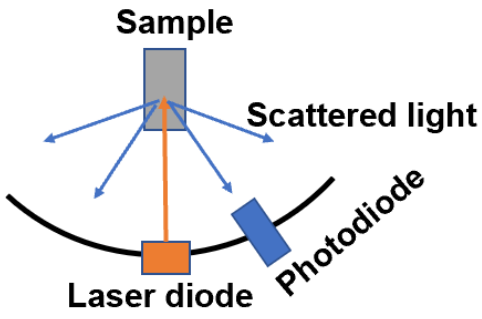

(a)

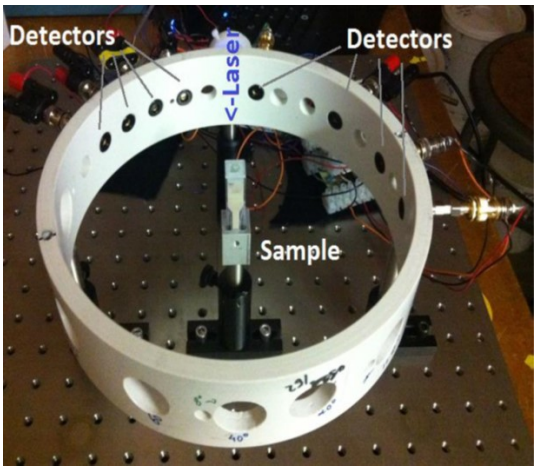

(b)

Figure 2.1: Ring setup: (a) schematic showing the laser diode and one of the detectors at an angle from the laser axis. (b) picture of the ring setup.

2.2 Settling tank setup

The device prototype consists of 4 components: settling tank, insertion column, insert metal tube, and gamma-ray source and detector tubes. The settling tank (shown in Fig 2.2(a)) is a cylindrical structure made of plexiglass covered by a lid. The insertion column (shown as Fig 2.2(c)) is a half cylinder made of plexiglass to protect the laser diodes and photodiodes from water and tailings samples. Insert metal tube (shown as Fig 2.2(d)) is designed to mount the laser diodes and photodiodes at six different depths. There are three holes at each level. The bigger hole in the middle is used to mount the photodiode, whereas the two adjacent smaller holes are used for laser diodes. The distance between the laser diode and photodiode is 1 cm. In such way, the light scattering angle can be set to 20°. This design can satisfy two different wavelengths of laser diodes used in one experiment. A low radioactive gamma-ray source is placed in a plexiglass tube, and a gamma-ray detector is placed in another plexiglass tube. The two plexiglass tubes are separated a few centimeters from each other. The gamma-ray source and detector can be moved vertically to determine the solids contents of the sample at various depths. The data can be used for the calibration of the optical sensors.

The settling tank design was developed to monitor the settling progress of oil sands tailings samples and estimate the solid content at six different depths. This setup was used for light scattering as well as gamma-ray techniques measurements. The relative changes of the light scattering signal as solids content sample settling were captured by photodiodes at six different depths. Gamma-ray measurements were carried out regularly, and the results were compared with the optical experiment.

2.3 Calibration tank

To verify the accuracy of the solids content measurements, a small tank was used, which is shown in Fig 2.3 for calibration experiments. This setup has a 2.8L small

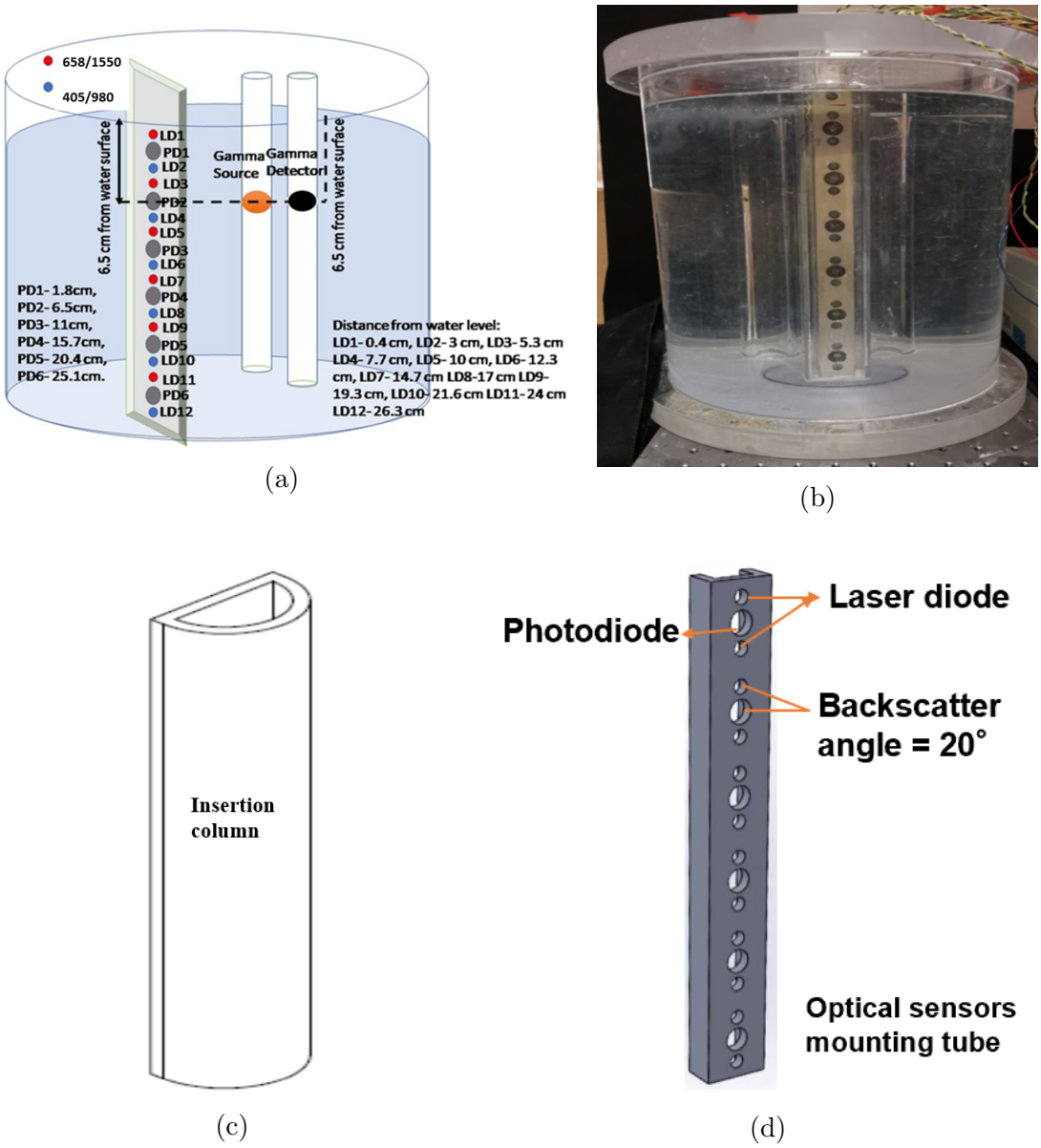

Figure 2.2: Settling tank setup (a) schematics of the settling column; (b) picture of the settling tank; (c) insertion column; (d) metal sensor tube.

volume which would not waste large quantity of sample and was easy to handle. Three LD-PD sensors were placed 10 cm, 20 cm and 30 cm from the bottom of the tank to confirm the sample was homogeneous. The tank was filled with a homogenous slurry sample with different concentrations (wt%), then the light scattering intensity was monitored by the photodiodes.

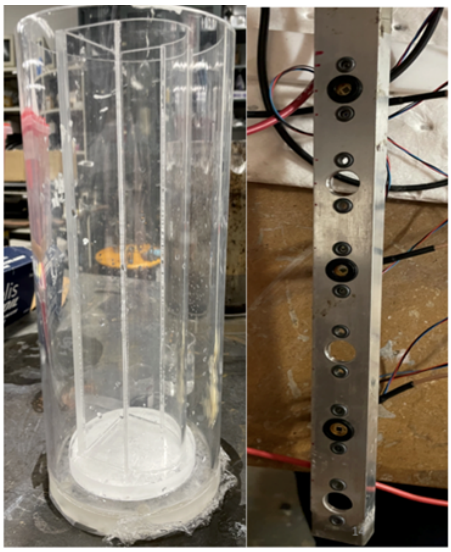

Figure 2.3: Picture of the calibration setup. The left picture shows the 3 litre volume tank with an insert tube. The right picture shows the 3 level optical sensors.

2.4 Optical sensor system

In this thesis, an optical sensor system was designed to monitor the settling process and solids content of the oil sands samples. The main components of the optical sensor includes a laser diode system with different wavelengths as the light source and a photodiode system as the light detection instrument. A circuit system was developed to drive laser diodes and photodiodes, and all components were tested.

2.4.1 Previous work

The lab group done jobs to create a laser diode pulsing circuit using a commercial laser driver FL500 from Team Wavelength. A 555 timer was used to create a square

wave signal with a 5Hz frequency to pulse the circuit. A voltage divider with a potentiometer was used to adjust the input signal to control the current flow through the laser diode. The major drawback of this design is that the FL500 laser driver is a constant current controller. Since the characteristic of each laser diode is different, the same laser diode current does not lead to the same output power. In addition, the output power can vary because of heating during the experiments. Therefore it is very difficult to set and maintain a constant output power of the laser diode.

2.4.2 Overall design

In this thesis, a new optical sensor circuit was developed. All the laser diodes would work under constant power mode in this design. A pulsed operation was used to avoid the overlap of light backscattering signal from other levels. Each output channel was on and lasted for 20s and switched to the next after a 10s gap. A photodiode system was designed to capture the laser light backscattering signal. Figure 2.4 shows the schematic of the overall circuit diagram. Details of the circuit and components testing will be introduced in the following sections.

2.4.3 Laser diode system

2.4.3.1 Design

The components of this laser diode control circuit (circuit1) include laser diodes with four different wavelengths (from Thorlabs), laser drivers (FL591FL from Digikey and MLD203P2E from Thorlabs), Arduino micro, and SN74CBT3251 multiplexers (from Digikey). The detailed circuit1 for visible wavelengths using all the components is shown in Figure 2.5. The same circuit1 was used to drive NIR wavelengths LDs only with a different laser driver for 1550nm LDs.

- **Laser diode**

Four models of laser diodes with different wavelengths were used, including 405nm, 658nm, 980nm and 1550nm (from Thorlabs). All laser diodes were under the oper-

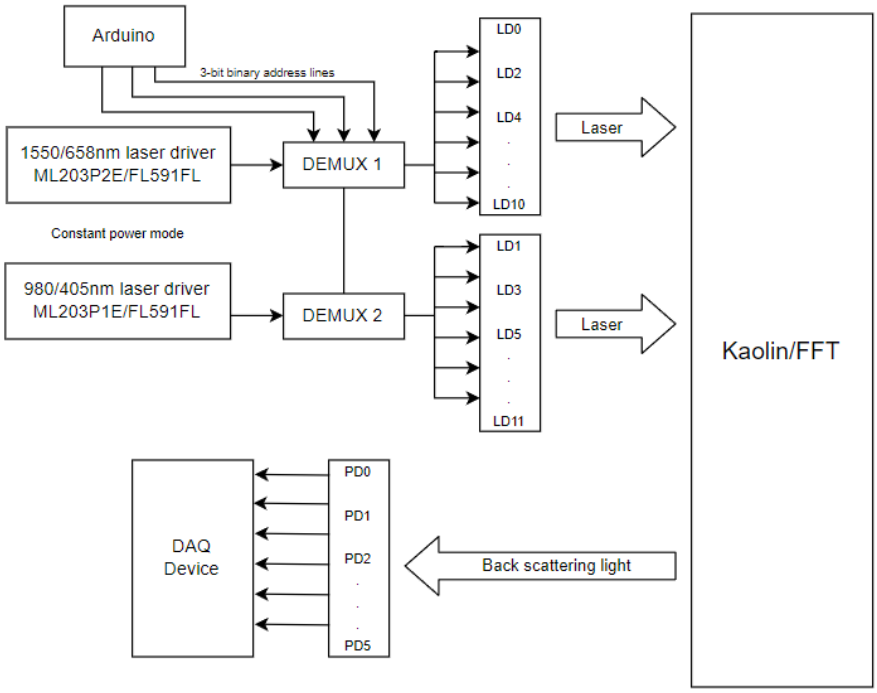

Figure 2.4: Block diagram for the overall circuit design.

ating range current and beyond the threshold. The specifications of 4 types of laser diodes are shown in Table 2.1.

Table 2.1: The four types of laser diodes used in the project and select properties

Wavelength	Thorlabs part number	Typical output power	Operation current range	Operation temperature range	Pincode
405nm	L405P020	20mW	20-55mA	0-75℃	Pincode B
658nm	L658P040	40mW	35-110mA	-10-50℃	Pincode A
980nm	L980P010	10mW	10-40mA	-10-50℃	Pincode A
1550nm	ML985B45F	5mW	10-50mA	-40-85℃	Pincode D

- **Laser driver**

A commercial laser driver board, FL591FL from Team Wavelength, can drive laser diodes with pincode A and B. It can work under both constant current and constant

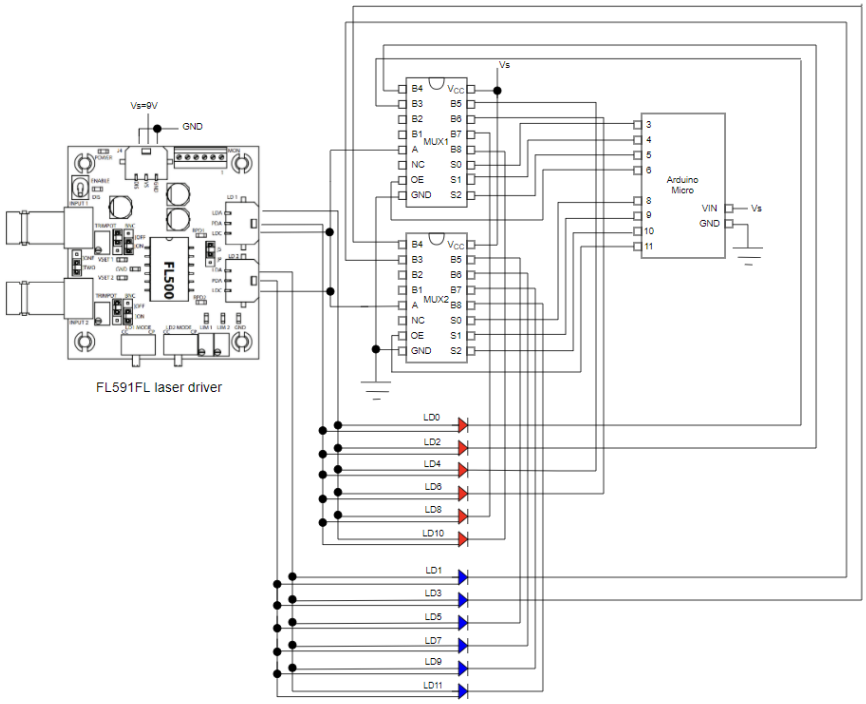

Figure 2.5: Detailed laser diode circuit1 with all components.

power mode. Therefore, the FL591FL laser driver was used to drive and control the power of the 405nm (pincode B), 658nm and 980nm (pincode A) laser diodes. A 9V supply was used to power the laser driver, and the laser driver was set to work under constant power mode. It consists of two output channels that can work separately. Each output can have a maximum of 250 mA LD current when working independently, which matches our LDs. Unlike the FL500 laser driver chip used before, the FL591FL laser driver board has a current limit and photodiode feedback for constant power operation. Under constant power mode, the PD current is used to determine the output power, which can be set by users. The driver adjusts the LD operating current to keep the PD current constant. Therefore, the LD current limit was set high (80% of maximum), and the output power could be adjusted by changing the PD current through the setpoint on the driver to give the desired constant power. Under constant power mode, the 405nm, 658nm and 980nm laser diodes typically worked around 25mA, 40mA and 25mA in the settling experiments, respectively.

MLD203P2E laser driver from Thorlabs was used to drive and control the power of 1550nm laser diodes. It is a constant power controller designed for pincode C and D (1550nm LD is pincode D), capable of driving up to 200mA LD current. A 5V power supply was used to power it under constant power mode. Moreover, the desired constant output power can be achieved by changing the resistor between pin PSET and pin VREF, as shown in Figure 2.6(b). Under constant power mode, the 1550nm laser diodes typically worked around 20mA in sample settling experiments.

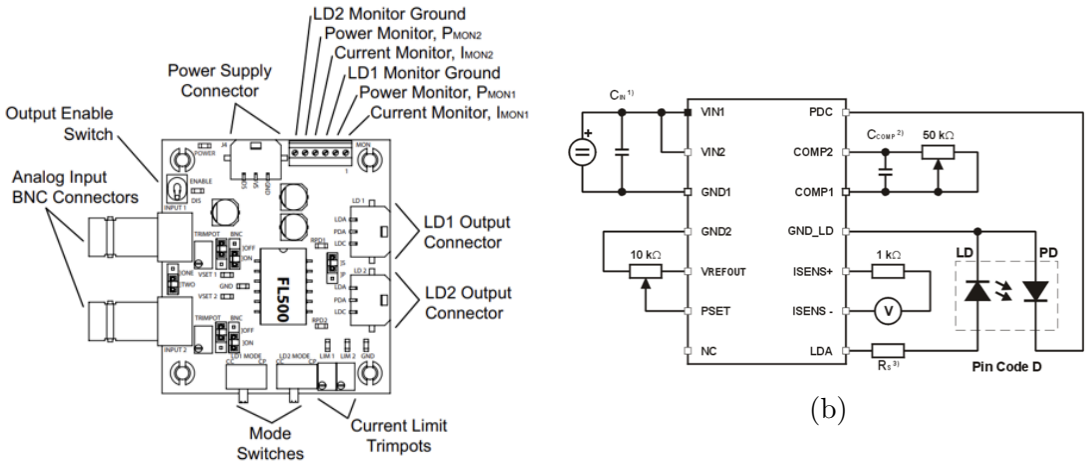

Figure 2.6: Laser driver: (a) FL591FL[34] (b) MLD203P2E[35]

• **Arduino Micro and multiplexer**

The pulsing operation of this laser diode system was performed by Arduino Micro and multiplexers. The Arduino Micro is a microcontroller board that has 20 digital input/output pins, a micro USB connection, and a reset button. The Micro Arduino can easily be controlled by programming to select the output pins. Therefore, in the LDs control circuit1, one Arduino Micro chip was used to control the selecting bits of the multiplexers through 3-bit binary address lines. The input voltage of the Micro Arduino chip is 10V. And the 5V operating voltage matches the input of the multiplexer. The code which was used to control the multiplexer signal selection is provided in Appendix A.1. Two SN74CBT3251 multiplexers from Digikey with 5V

operating voltage and 8 I/O pins, which were controlled by the Arduino Micro chip, were used to select signals between 12 laser diodes. A fixed 5V power supply was used to power the multiplexer. Each multiplexer provided 6 channels and in total 12 channels for 12 laser diodes. During an experiment, each output signal lasted for 20s and switched to the next. The frequency of 1 cycle of 12 laser diodes was then 4 minutes.

- **Current monitor**

In the NIR wavelength settling tank experiment, current monitors were added to monitor the current changes during the experiment of all the laser diodes to confirm they are working under the operation range. The detailed current monitor diagrams for FL591FL and MLD203P2E laser drivers are shown in Figure 2.7. The current signal was captured by the DAQ device, which will be introduced in the photodiode system section. For the FL591FL laser driver, the current monitor measure points provide a voltage proportional to the laser diode current. The transfer function is:

$$y = \frac{Vmon * 0.25A}{2V} \tag{2.1}$$

For the MLD203P2E laser driver, the voltage between the ISENS+ and ISENS- pins is proportional to the laser diode current and can be calculated by:

$$y = \frac{Vsens(V)}{1(k\Omega)} \tag{2.2}$$

In summary, the working principle of the pulsed laser diode system is: laser diodes run at constant power throughout the experiment period, and pulsed operation is used to get rid of the cross-talk backscattered light signal from other levels. The 405nm, 658nm, 980nm and 1550nm laser diodes are driven and controlled by FL591FL and MLD203P2E laser drivers. The pulsed operation is conducted by the combination of an Arduino Micro and two multiplexers. Different laser diode is selected sequentially

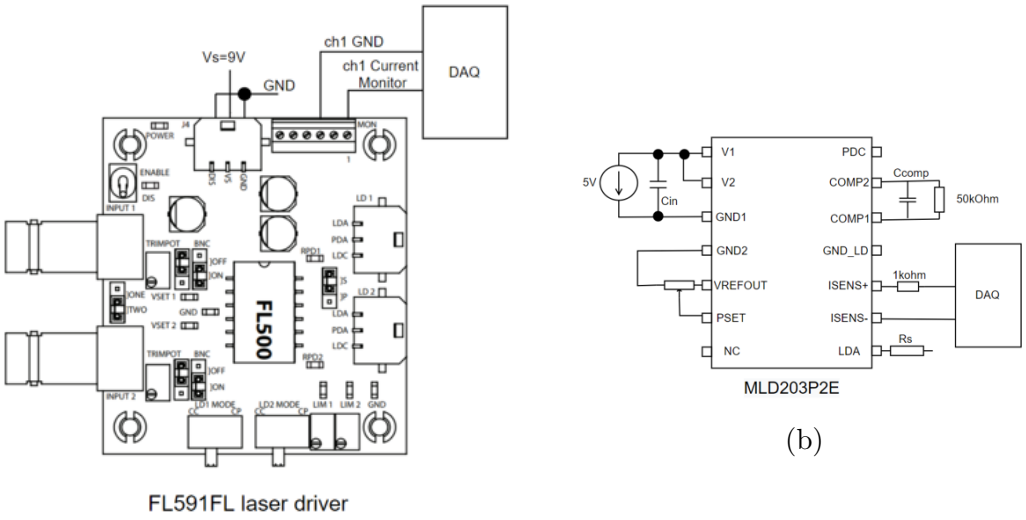

(a) (b)

Figure 2.7: Laser diode current monitor circuits: (a) FL591FL laser driver[34] (b) MLD203P2E laser driver[35]

through multiplexers which are controlled by the address lines of Arduino Micro. Each LD will be on and last for 20s and switch to the next. The time of 1 cycle of 12 laser diodes on and off is then 4 minutes. The detailed order is 658/1550nm LD0(20s) – 405/980nm LD1(20s) – 658/1550nm LD2(20s) – 405/980nm LD3(20s)– .....– 658/1550nm LD10(20s) – 405/980nm LD11(20s).

2.4.3.2 Testing

To verify the reliability of the constant mode of the commercial FL591FL and the MLD203P2E laser driver, six of each 405nm, 658nm, 980nm and 1550nm laser diode were tested. Constant power mode utilizes the laser's build-in PD current to regulate the intensity of the output power. Therefore, the PD current of six LDs was set to the same value. The laser current limitation was selected within the operating range. The results are shown in Figure 2.8 (a) to (d). The measured output power (Figure 2.9) was not exactly the same for each laser diode. The difference in output power was due to the different characteristics of each laser diode. The measured PD current of all the 6 laser diodes showed a slight difference, which was used to determine the

output power. The difference in output power was within 20%.

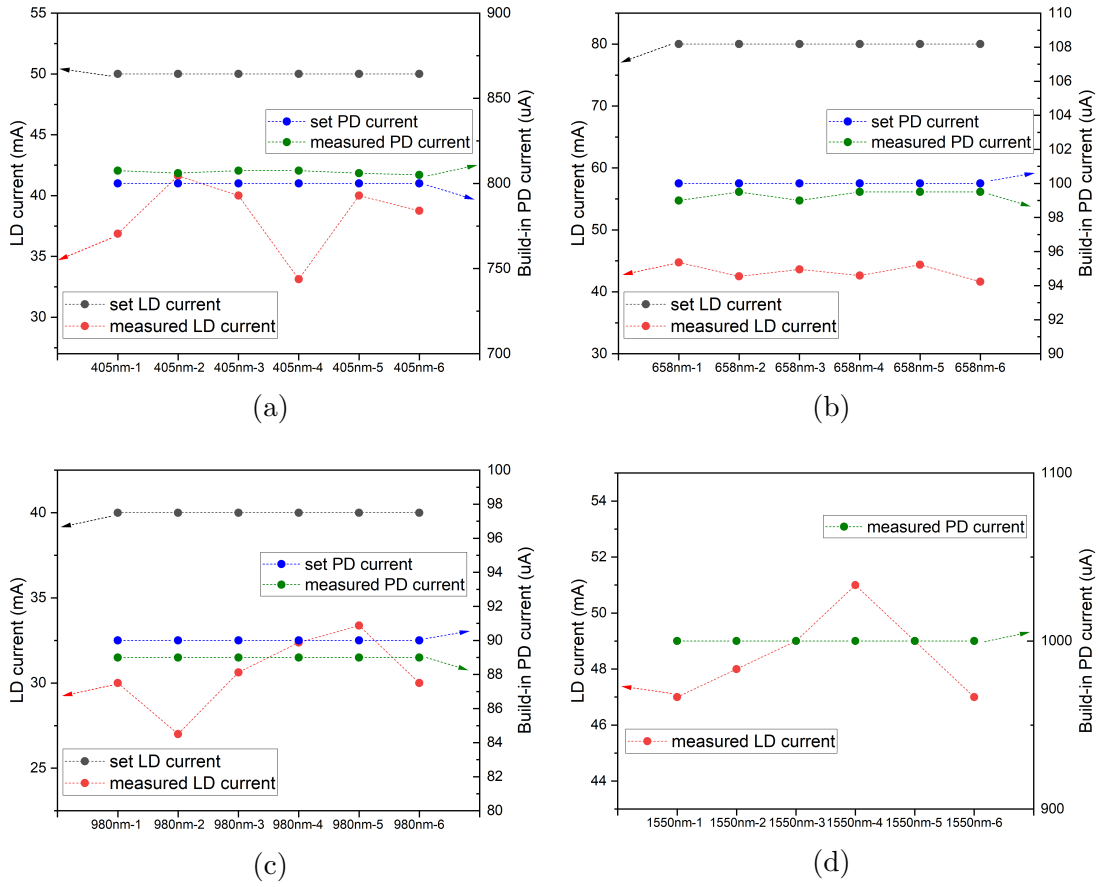

Figure 2.8: Constant power mode reliability test for 405nm, 658nm, 980nm and 1550nm LDs (a)results of 405nm LDs (b)results of 658nm LDs (c)results of 980nm LDs (d)results of 1550nm LDs.

To obtain the characteristics of the laser diodes, the relationship between laser diode current and output power was tested. A laser diode's output power is proportional to its operating current. One 405nm LD and one 658nm LD were tested, the results are shown in Figure 2.10 (a) and (b). As shown in Figure 2.10 (c) and (d), six of each 980nm and 1550nm LD were tested, each laser diode has slightly different characteristics. To ensure the validity of the experimental data, all the laser diodes should be operated in the linear range.

The laser diodes were soldered to the conductive wire and then connected to the circuit. To ensure no changes in the performance of laser diodes during the soldering

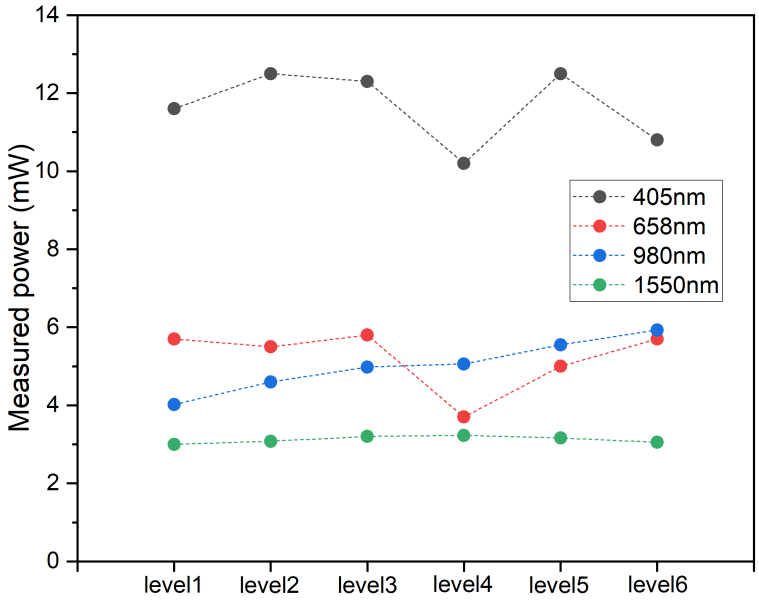

Figure 2.9: LDs power measurement. Black symbols show 405nm LDs power, red symbols show 658nm LDs power, blue symbols show 980nm LDs power, and green symbols show 1550nm LDs power.

process, the output power, PD current, and LD current before and after soldering were tested. The results are shown in Table 2.2. The performance of the laser diodes did not change significantly before and after soldering.

We faced a signal oscillation issue when testing the performance of circuit1 with a Teflon chip. The laser light signal would be totally reflected by the Teflon chip. The noise in the signal was from the power supply. The input voltage from the DC power supply always noisy and contains a lot of AC ripples. The problem was solved by adding a 0.1μF bypass capacitor across the multiplexers to short AC signals to the ground and produce a pure DC signal. The change before and after adding the bypass capacitor is shown in Figure 2.11.

2.4.3.3 Improvement

During the experiments, it was found that the average lifetime of six 980nm laser diodes was less than one month. And as time went by, all the six 1550nm laser diodes current showed a downward trend probably caused by thermal effect. In order to

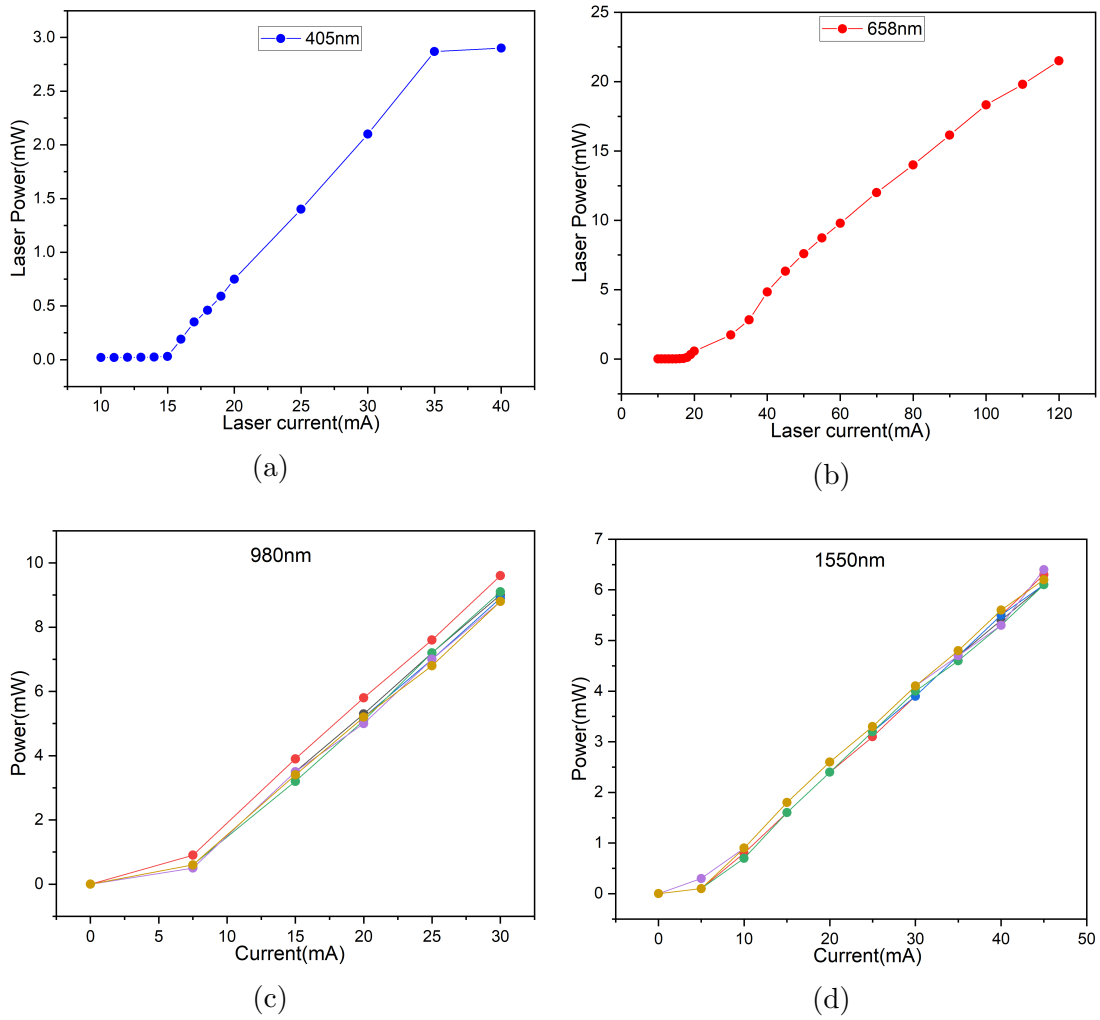

Figure 2.10: Laser diodes I-Power curve: (a)results of 405nm LDs (b)results of 658nm LDs (c)results of 980nm LDs (d)results of 1550nm LDs.

Table 2.2: Comparison of laser diode characteristics before and after soldering

NO.	Build-in PD current (A)	LD current (mA)	Output power (mW)
405nm-1	436	25	6.5
405nm-1	346	25	6.25
405nm-2	920	35	14.3
405nm-2	826	35	14.3
405nm-3	453	25	5.3
405nm-3	445	25	5.8
405nm-4	121	35	15
405nm-4	958	35	16

(a) Before soldering

NO.	Bulid-in PD current (A)	LD current (mA)	Output power (mW)
405nm-1	448	25	7
405nm-1	361	25	6.3
405nm-2	958	35	15
405nm-2	841	35	14.7
405nm-3	450	25	4.8
405nm-3	425	25	6.7
405nm-4	924	35	14.2
405nm-4	900	35	15.3

(b) After soldering

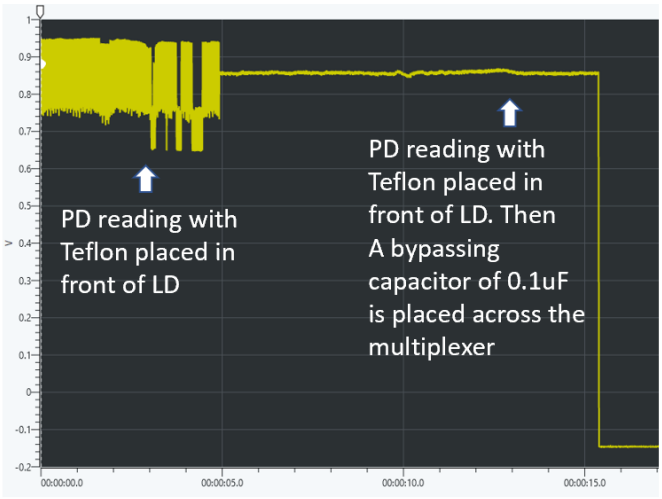

Figure 2.11: The change before and after adding the bypass capacitor

solve these problems, a second-generation NIR wavelength laser diode control circuit system (circuit2) was designed. The new circuits are shown in Figure 2.12. The difference between the two circuits was based on the different pin codes of 980nm and 1550nm LD.

Due to the unique manufacturing characteristic of 980nm LD, the laser driver for 980nm LDs was changed. The 980nm laser diode has a special case common-grounded pin, which does not match the FL591 laser driver used in circuit1. Therefore, the 980nm LDs were connected in the wrong configuration in the previous circuit. The laser driver was replaced by the MLD203P1E from Thorlabs, which matches the manufacturing characteristic of the 980nm LD and costs less. MLD203P1E is a constant power controller with the control range of Laser Current up to 200mA. A 5V supply was used to power the laser driver. The current limit can be adjusted by the Rs, and the output power can be adjusted by the resistance between pin PEST and VREF, shown in Figure 2.13. The current monitor circuit of the MLD203P1E laser driver is the same as MLD203P2E.

Demultiplexers, relays and flyback diodes were introduced to the improved system. Two SN74LV4051AN demultiplexers from Digikey were used to select signals between 12 laser diodes. The output paths of demultiplexers were controlled by Arduino Micro.

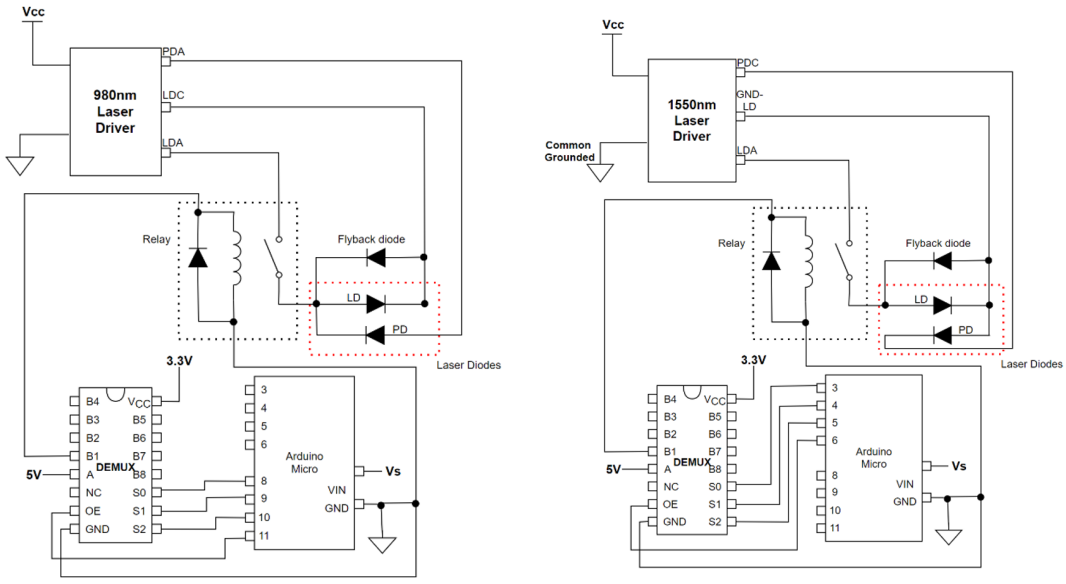

Figure 2.12: Improved laser diode system circuit2 : (a) 980nm laser diode system (b) 1550nm laser diode system.

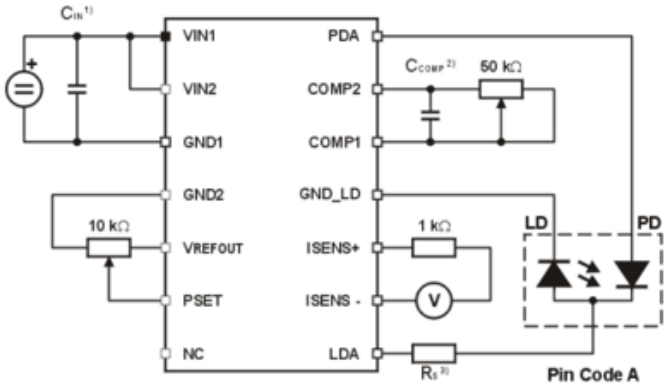

Figure 2.13: MLD203P1E laser driver for 980nm laser diodes[36]

A fixed 5V power supply was used to power the demultiplexers. Each demultiplexer provided 6 channels and in total 12 channels for 12 laser diodes. 3570-1331-053 relays from Digikey were operated as electronic switches to control the laser diodes on and off. The output voltage of the DEMUX was set at 5V, which matched the switch-on voltage of the relay. The RFUH20TF6SFHC9 diode from Digikey connected across the laser diode was used to eliminate flyback voltage, which is the sudden voltage spike seen across the laser diode when the current is suddenly reduced. The flyback diode was used to protect the laser diode. A 10s delay was added between the LD switching process to avoid the cross-talk of two LDs during the switching process. The components of circuit1 were not commonly grounded, which could introduce noise and even damage the components. In the new circuit2 design, all the components were commonly grounded.

For using this sensor system in oil sands tailings ponds, it is expected that the sensor system can continue operating for 6 months without the need for maintenance. The improved laser diode circuit2 is durable and expected to operate continuously for 6 months or more. The lifetime of the components in the optical sensor system is significantly longer than six months under proper operating conditions. The entire optical sensor system has been continuously operated multiple times for more than three months in the lab, giving good confidence that the 6 month lifetime requirement for tailings ponds operation can be met.

2.4.4 Photodiode system

2.4.4.1 Design

A six-level photodiode system was built to measure laser light scattering signal from the oil sands samples at different depths. The photodiode circuit is shown in Figure 2.14. The complete circuit is the unit circuit repeated by 6 times. The differences between the visible and NIR wavelength photodiode circuit are photodiode types and load resistance.

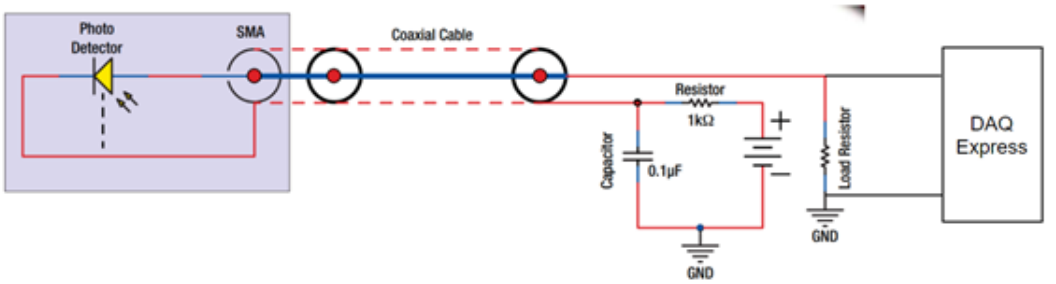

Figure 2.14: Photodiode biased circuit[37]

The SM05PD1A and SM05PD5A photodiodes from Thorlabs were used to capture the visible (405nm and 658nm) and NIR (980nm and 1550nm) light scattering signals from the samples, respectively. The circuits were biased to increase the saturation limit of the photodiode. A 10V reverse bias voltage and a load resistance of 3MΩ were used for the SM05PD1A photodiode circuit, while a 3V reverse bias voltage and 750Ω load resistance were used for the SM05PD5A photodiode circuit. The photodiode responsivity is shown in Figure 2.15.

The USB 6218 DAQ device was used to read the signal measured by the photodiodes at different depths simultaneously. The DAQ device can retrieve data from 16 different channels. The analog input resolution of this device is 16-bit, and the maximum sampling rate is 250k/s. The sapling rate used in this experiment was 1 data/s. The DAQ express software can be downloaded from the NI instrument website.

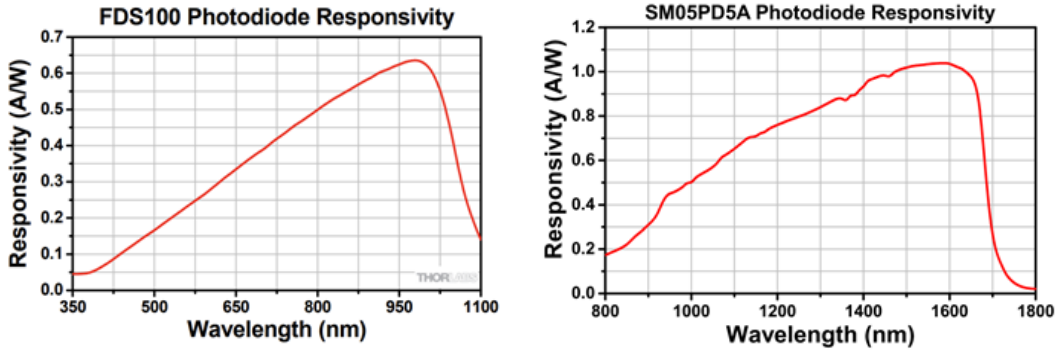

(a) (b)

Figure 2.15: Photodiode responsivity: (a) SM05PD1A[37] (b) SM05PD5A[38]

2.4.4.2 Testing

The power curves of SM05PD1A and SM05PD5A photodiode were measured to make sure the signal captured in experiments was within the linear range. The results are shown in Figure 2.16. Six SM05PD1A photodiodes were tested by a 405nm laser diode with 7mW output power, while six SM05PD5A photodiodes were tested by a 1550nm laser diode with 2.5mW output power. As shown in Figure 2.16, each PD did not behave exactly the same due to the different inherent characteristics.

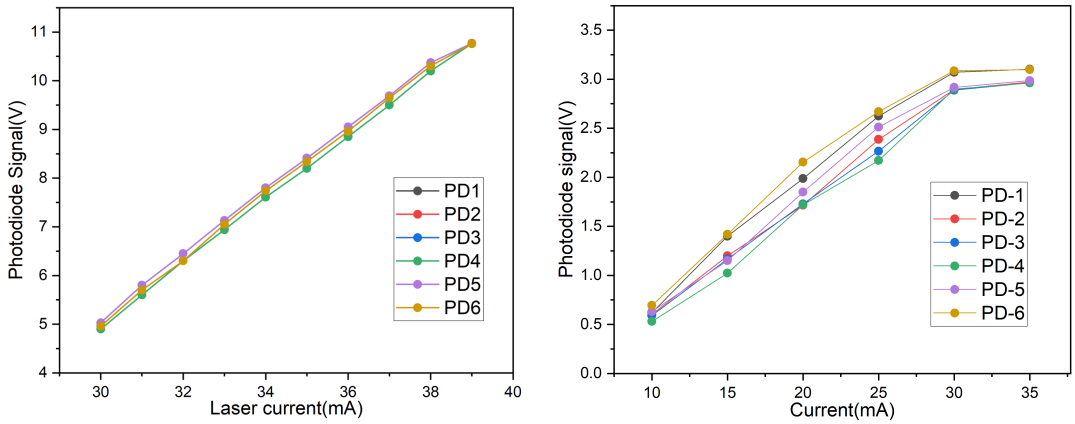

(a) (b)

Figure 2.16: Relationship between laser diode operating current and photodiode signal: (a) SM05PD1A (b) SM05PD5A

2.4.4.3 Data acquisition

Proper data selection must be performed to get the correct corresponding light scattering signal from all levels. The period of one laser diode to be on was 20s. The sampling rate of the DAQ device was selected to be 1 data/s, so 20 data points were collected during the time when the laser was on. To eliminate bad data points, the first and last three data points were removed. The average of the remaining 14 data points was taken as a representation of the light scattering intensity during the time when the laser was on. The time interval between the two data points was 6 minutes.

2.4.5 Cost of the optical sensor system

The optical sensor system based on light scattering (including a laser diode lasing system and a photodiode detecting system) is relatively low-cost, and the cost of the whole system is under 2500$. The price of each component described above for the optical instrument is listed in Table 2.3.

Table 2.3: Price of components used for the optical instrument

Components	Price
L405P20 405nm laser diodes	$53.02
L658P040 658nm laser diodes	$28.95
L980P010 980nm laser diodes	$28.95
ML985B45F 1550nm laser diodes	$52.48
FL591FL Laser Driver	$287
MLD203P1E Laser Driver	$50
MLD203P2E Laser Driver	$50
SN74LV4051AN 1-8 Demultiplexer	$1.39
Arduino Micro	$20.7
3570-1331-053 Relay	$1.71
RFUH20TF6SFHC9 flyback diode	$2.37
SM05PD1A Photodiode	$73.74
SM05PD5A Photodiode	$297.05

2.5 Summary

A ring setup was developed to conduct calibration measurements, and determine the light scattering angular distribution for observation angle optimization. A lab-scale settling tank setup was developed to imitate the situation when the analyzer is submerged in the tailing ponds. A small calibration tank setup was developed for

calibration. And a relatively low-cost optical sensor system based on light scattering (including a laser diode lasing system and a photodiode detecting system) was developed to analyze the solids content at different depths in sample settling experiments. The solids content analyzer is expected to operate continuously for 6 months or more before maintenance is required.

Chapter 3

Settling Tank Studies

This chapter focuses on lab-scale settling tank experiments using the optical sensor system (described in chapter 2). The goal is to monitor the settling behavior of slurry samples at different depths using LDs with visible (405 nm and 655 nm) and near-infrared (980nm and 1550 nm) wavelengths.

3.1 Slurry samples

Kaolin and FFT samples settling experiments were conducted in this study. Kaolinite is one of the major clay minerals in oil sands tailings, and therefore, commercial Kaolin samples with different particle sizes were used. In this thesis, the Kaolin was used as a surrogate sample due to its rapid settling behavior. The Fluid Fine Tailings (FFT) samples are mixtures of water, solids (almost entirely fines and clays), and residual bitumen that are generated as by-products of mine-based operations in the oil sands and then stored into mined or excavated pits generally termed as tailings ponds. It is crucial for this thesis to analyze the solids content in FFT samples. Therefore, FFT samples with different solids content were also used to perform settling experiments.

3.1.1 Kaolin sample

Commercially available Kaolin of different particle sizes (200 nm, 600 nm, and 2.5 microns) was purchased from BASF to perform the experiment. In this thesis, the

Kaolin sample with a particle size of 600nm was used to monitor the settling process and changes.

3.1.2 FFT sample

Different FFT samples with various solids and bitumen contents were procured from CNRL (see Table 3.1). To understand the effect of solids and bitumen contents, a study was conducted with different FFT samples. These samples label are used throughout the thesis.

Table 3.1: FFT samples used in the thesis

Bucket label	Water(wt%)	Bitumen(wt%)	Solid(wt%)
FFT-A	67.0	1.6	31.5
FFT-B	79.4	2.1	18.2
FFT-C	61.2	3.2	35.6
FFT-D	73.6	1.4	25.0
FFT-E	77.6	2.4	20.1

3.2 Visible wavelength (658nm & 405nm) experimental results and discussions

The settling tank experiment was carried out using two visible wavelengths (405nm & 658nm) LDs. The Kaolin with 600nm particle size and two FFT samples with different solids content were used. The arrangement and height of the LD-PD sensor at six levels are shown in Figure 2.1(a). The scattering angle was 20°. The visible wavelength experiments were conducted by circuit1 (see chapter 2.4.3). The DAQ device recorded the signal captured by PDs with a 1Hz sampling rate at six different depths simultaneously. A water test was done before conducting the sample settling experiments, and the data was used as a comparison to the results after the settling

process. Results of light scattering signal from water (0 wt% solids) for levels 1 to 3 are shown in Fig 3.1(a). The results were extracted from the raw data shown in Fig 3.1(b). The differences in the signals were due to the slight difference in LD output power at each level.

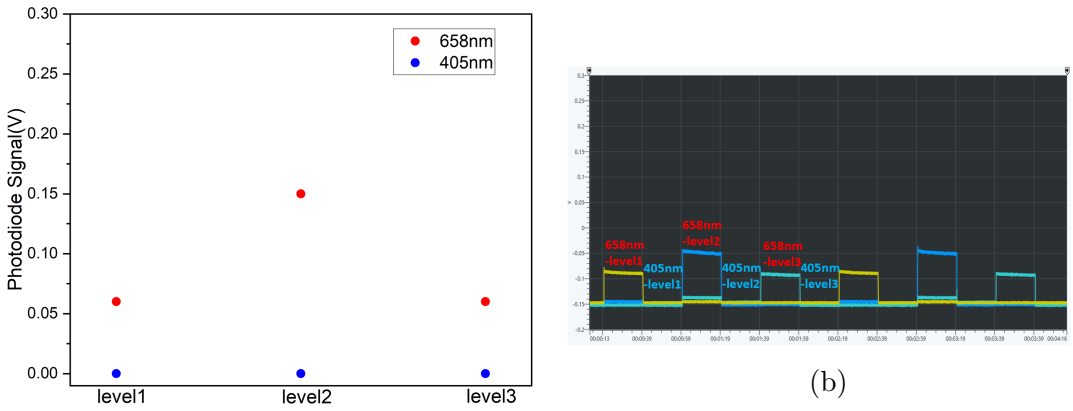

(a) (b)

Figure 3.1: Visible wavelengths (405nm & 658nm) LD water test in settling tank (a) extracted data (b) original data (photodiode signal versus time)

3.2.1 Kaolin sample experiment results and discussions

Dry Kaolin powder with 600nm particle size was mixed with tap water to make a 15wt% sample. This concentration was chosen because the sample could be settled within one day, thus reducing the experiment time. An 18-hour test and a 24-hour test were conducted, and the sample could be ultimately settled within this experiment time. The temporal evolution of scattered light intensity for the 15wt% Kaolin sample measured by visible wavelengths LD is shown in Figure 3.3. We also took pictures of the settling tank at around 1 hour intervals to track the temporal evolution of the water-solid interface. The temporal change in 658nm light scattering signal and the settling tank pictures are shown in Fig 3.2.

Measurements results at six different depths showed the light scattering intensity decreasing corresponding to the solids content settling process. During settling, the solids moved down, creating a water-solid interface with clean water above and solids

sample below. The water-solid interface continued moving down, leading to higher solids content in the solids zone. As seen from the 18hrs Kaolin settling data measured by 658nm LDs (Figure 3.3(a)), the scattered light signal of three levels on top decreased slowly at the beginning, then rapidly decreased (at transition points A, D and F for level 1 to 3, respectively) followed with an increase in intensity (at transition points B, E and G for level 1 to 3, respectively), and finally became stable. As shown in Figure 3.2, the scattering intensity decreased significantly when the water-solid interface passed through the 658nm LDs (at 1h, 2h and 3h time points) due to fewer particles attenuating the scattered light. Light scattering signal increased slightly in intensity when the water-solid interface passed through the PDs due to an increase in scattered light noise from the interface. The water-solid interface never reached the lowest three levels, and their scattered light signal did not change much throughout the experiment.

The 405nm LDs results (Figure 3.3(b)) showed similar trends to those of 658nm LDs. The scattered light intensity of level 1 to 3 decreased significantly at transition points A, D and G, respectively, as the water-solid interface passed through the PDs positions. The signal drops were corresponded to the solids settling. The scattered light signal increased significantly at transition points B, E and H when the water-solid interface moved down to the 405nm LDs positions. The laser light from 405nm LDs was scattered from the water-solid interface, and some of them bounced around the interface and finally arrived at the PD. Thus it caused the scattered light signal to increase. With the solids further settled, the 405nm LD was further away from the water-solid interface, and the scattered light noise from the interface decreased. Therefore, the scattered light signal decreased at transition points C, F and I for level 1-3, respectively.

As shown in Figure 3.3(c) and (d), the settling characteristics of the 24hrs experiment was similar to the 18hrs measurement, only with a different time scale. After the Kaolin sample settling process, the light scattering signal for both 405nm and

658nm was higher than the water test (Figure 3.1), indicating that a small amount of Kaolin particles remained in the water zone.

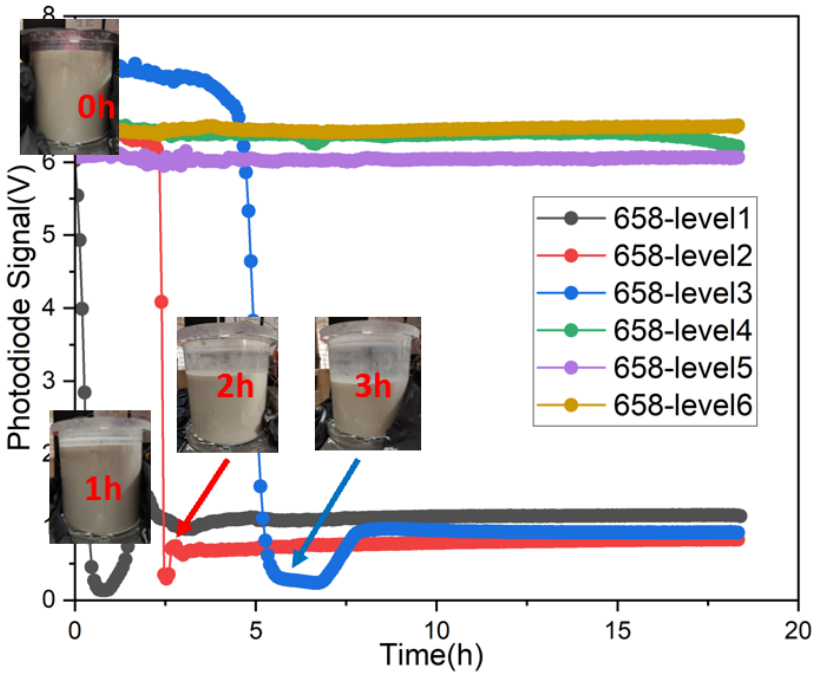

Figure 3.2: Settling process correlate to the 658nm relative scattering signal changes in 15wt% Kaolin sample measurement

3.2.2 FFT sample experiment results and discussions

The Fluid Fine Tailings (FFT) samples were measured with the same setup. The FFT samples are more complex, containing minerals, sand, clay, bitumen, and water. The settling tank experiments used two FFT samples (see Table 3.1). FFT-B sample (18.2 wt%) was used, and FFT-A sample was diluted to 21.7wt% solids content to fill the settling tank.

For the 18.2 wt% FFT-B sample, 658nm results at level 1 (shown in Figure 3.4(a)) showed the scattered light signal decreased correspondingly to the decrease of solids content. The position of the water-solid interface during the experiment for the FFT-B sample is shown in Figure 3.5. The water-solid interface moved rapidly for 4 cm in the first 10 days, then slowed down significantly and moved less than one centimeter

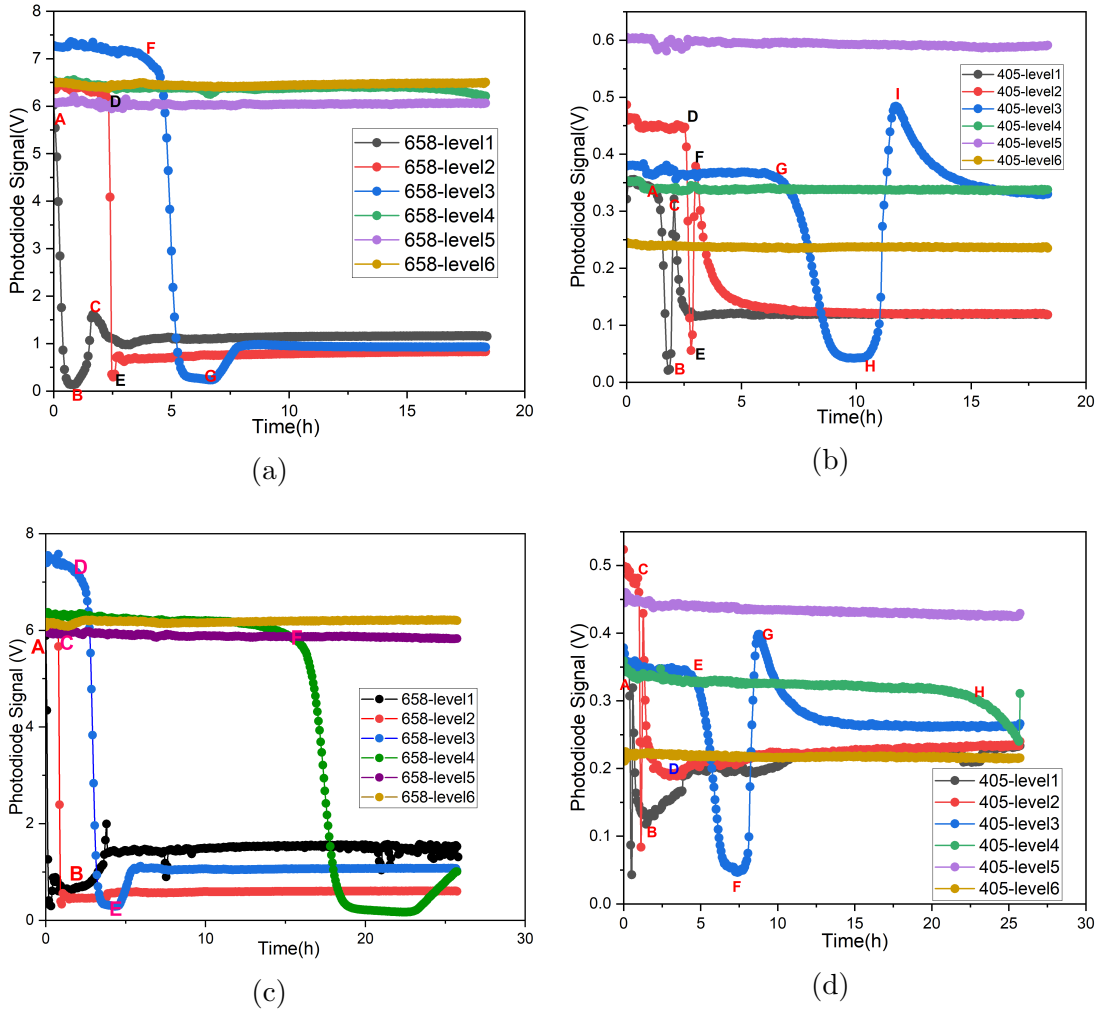

Figure 3.3: 15wt% Kaolin sample with 600nm particle size settling tank experiments results: (a)658nm LDs 18-hour test, (b)405nm LDs 18-hour test, (c)658nm LDs 24-hour test, (d)405nm LDs 24-hour test. This measurement was conducted by circuit1.

during the period from day10 to day30. It was observed that the significant drop in scattered light intensity at transition point A coincided with the water-solid interface at the depth of the first level LD location. The intensity increase happened when the water-solid interface moved to the first level PD location at transition point B. The scattered light noise from the water-solid interface caused the increase in intensity. Then with the solids continued settling, the scattered light from a large number of small particles remained in the water zone and noise from the water-solid interface caused the increase of scattered light signal (from point C). The significant drop of 658nm signal of level 1 sensor at turning point D was caused by the water evaporation making the LD out of the water and exposure to air.

For the 658nm signal at level2, the scattered light signal increased slightly from day1 to around day12 due to the solids settled from the upper level. Then the scattered light signal decreased at turning point E when the water-solid interface passed through the level2 658nm LD position. When water-solid interface reached the depth of the second PD location, the scattered light noise from the water-solid interface dominated and the signal increased at turning point F. After day25, the water-solid interface moved below the level2 LD position. The 658nm signal of level2 still showed a much higher signal than the water test (shown in Figure 3.1(a)), which indicated that a high amount of particles remained above the water-solid interface and no or very less bitumen fouling on the second level optical window. The other four levels were under water-solid interface during the measurements and show large signal fluctuations. One reason is the complicated settling process, and another possibility is the unstable output of the laser diodes caused by the circuit1.

For 405nm measurements at level 1 (Figure 3.4(b)), a decrease in intensity occurred when the sample settled at the PD position (turning point A), which corresponded to the sample settled. Then a significant increase caused by the high scattered light noise from the water-solid interface occurred (turning point B) when the water-solid interface passed the first 405nm LD location. At transition point C, the scattered light

noise decreased when the water-solid interface moved further down and away from the 405nm LD. After that, the scattered light signal started to increase gradually. The possible reason is that fine particles and oil drops whose density is minor than water floated upward, leading to increased scattered light. The scattered light intensity of 405nm LDs at the 2-6 levels decreased slowly over the whole period of the experiment. The first possibility causing the continuous decrease is that the output power of 405nm LDs decreased during the measurement process. The second possibility is the bitumen fouling effect. The fouling caused by residual bitumen in the tailing samples accumulated over time covered the optical windows and decreased the transmission of 405nm laser light.

The same setup was used to measure the 21.7wt% FFT-A sample. We did not get valid data of both 658nm and 405nm LDs due to the bad performance of circuit1. As described in chapter 2, the circuit was improved to avoid further problems.

3.2.3 Comparison with previous work

Some initial measurements used a similar setup were done by another graduate student, Timothy H. Ho, in our research group previously to monitor the settling behavior[6]. Kaolin 33wt% and Thickened Underflow Tailing (TUT) 35wt% samples were tested by 405nm LDs with power around 20mW at different heights (1cm, 6cm, 11cm and 17cm from the top), and the results are shown in Figure 3.6[6]. The scattered light intensity at the first level (1 cm from the top) decreased slowly up to 5 hours for the Kaolin and 50 hours for the TTU samples, then rapidly decreased and eventually showed a slight increase. In the settling process, the water-solid interface moved 1 cm in 5 hours and 50 hours for the Kaolin and TTU samples, respectively, consistent with the rapid scattered light signal decreases. The second level (6 cm from the top) showed qualitatively similar behavior to the first level but with a time delay.

For both TUT and FFT measurements, the scattered light signal increased slightly after the sample settled, caused by the remaining fine particles above the water-solid

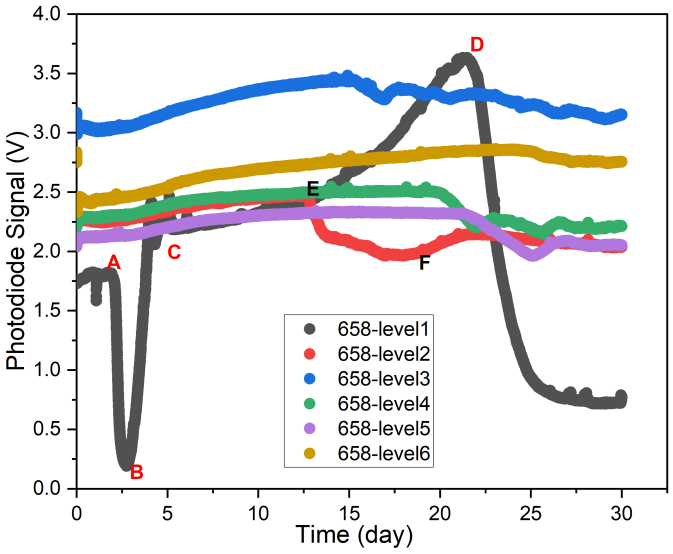

(a)

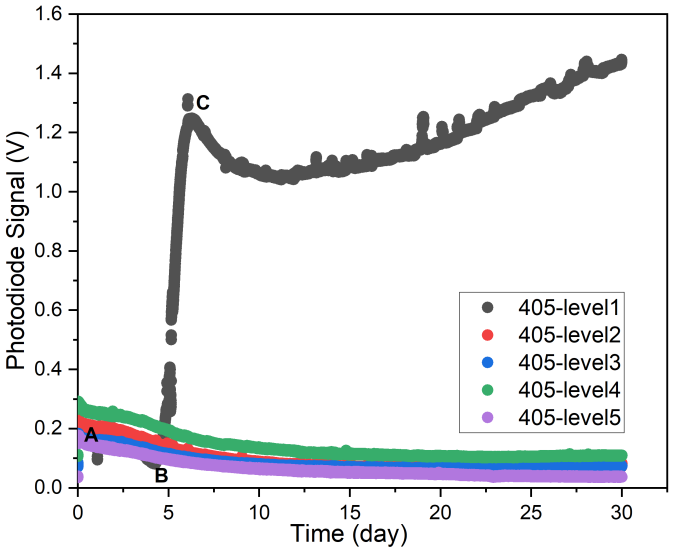

(b)

Figure 3.4: 18.2wt% and 21.7wt% FFT sample settling tank experiment results: (a)658nm LD 18.2wt% FFT test, (b)405nm LD 18.2wt% FFT test. This measurement was conducted by circuit1.

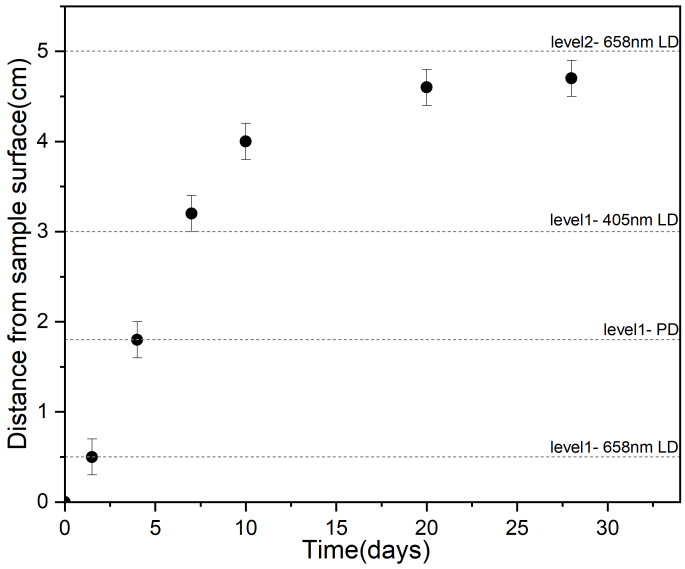

Figure 3.5: Water-solid position during the 18.2wt% FFT-B sample measurements. 658nm and 405nm LDs were used.

interface. And the scattered light intensity at bottom levels decreased slowly over the tests in TUT and FFT results. The possible reason is that the fouling at the sensor position accumulated by residual bitumen in TUT and FFT samples decreased the transmission of 405nm LD light. However, the high scattered light noise from the water-solid interface was only observed in the settling tank test. The time scale and scattered light intensity of the two sets of Kaolin tests were different due to the different Kaolin sample concentrations and 405nm LD output power. And the difference in time scale between TUT and FFT measurements were due to their different sample composition.

3.3 Near-infrared wavelength (980nm & 1550nm) experimental results and discussions

3.3.1 Wavelength optimization

The relative change in the light scattering intensity with the solids content measured by different wavelengths of LD was carried out in our research group by Dr. Tulika Sirvastava. The results indicated that the near-infrared (NIR) wavelengths at 980nm

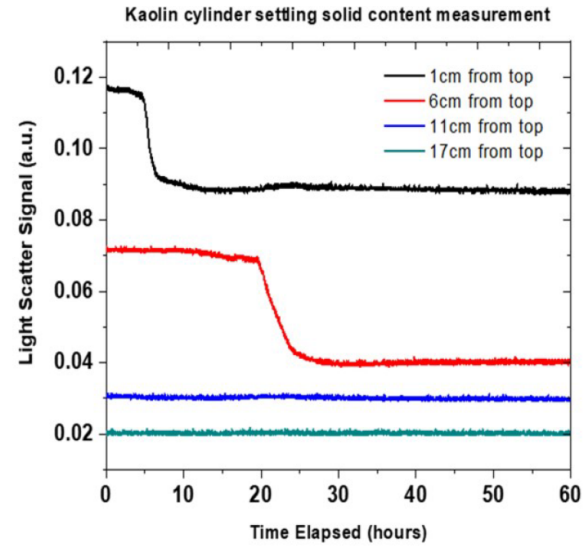

(a)

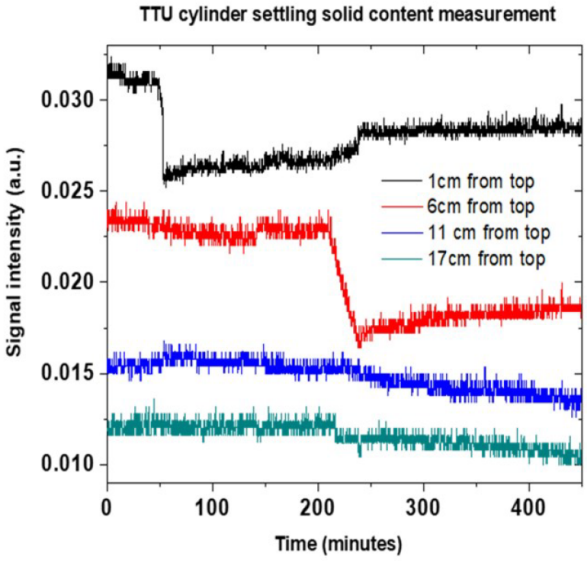

(b)

Figure 3.6: Measurement using 405nm laser diode at heights of 1 cm, 6cm, 11 cm and 17 cm from top respectively and measurement angle was at 20°. (a) Kaolin 33wt% starting solids content of hours elapsed versus relative signal strength. (b)TUT 35wt% starting solids content measurement.[6]

and 1550nm demonstrated higher sensitivity over the entire solids content range up to around 40 wt% compared to the visible wavelengths[31].

The visible wavelengths (405nm & 658nm) were not sensitive to solids content higher than around 2wt% (Figure 3.7(a)i), with the scattered light intensity remaining almost constant. On the other hand, water absorbs NIR wavelengths laser light due to the O-H stretching vibration[39]. Therefore the NIR wavelengths, especially 1550nm, could help detect a small amount of solids content change (Figure 3.7(a)ii). Pure water (shown in Figure 3.7(a) as 0 wt%) strongly absorbed the NIR wavelengths laser light, and the presence of small amounts of solids in the water resulted in non-zero scattering intensity. As shown in Figure 3.7(b), the results of two different FFT sample mixtures indicated the applicability of the light scattering technique regardless of the variation in the tailings' composition.[31]

The black fouling on the cuvette wall (Figure 3.8(a)) was accumulated by residual bitumen in the FFT samples over time. The 405nm and 1550nm data are compared in Figure 3.8(b) for the diluted samples of FFT-E. The results suggest that bitumen absorption of visible wavelengths (especially 405nm) caused the substantial variability of the scattered light signals and error in the measurements. In comparison, the NIR wavelengths (especially 1550nm) measurements were very repeatable and reliable. The results of the transmission study were conducted on the diluted (1 wt% solids content) raw FFT-E and cold-washed CW-FFT-E mixtures (Figure 3.8(c)). This further confirmed that bitumen fouling absorption caused the reduction of the visible scattered light signals, possibly leading to inaccurate solids content measurements. However, the transmittance spectra of FFT-E and CW-FFT-E were essentially the same for the NIR wavelength range, indicating little or no influence of bitumen fouling on the scattering measurements with the NIR wavelengths.[31]

Beyond 1550nm, laser diodes are expensive and not economically suitable for practical applications. Therefore, in this thesis, 980nm and 1550nm laser diodes were chosen to conduct the NIR wavelengths sample settling experiments.

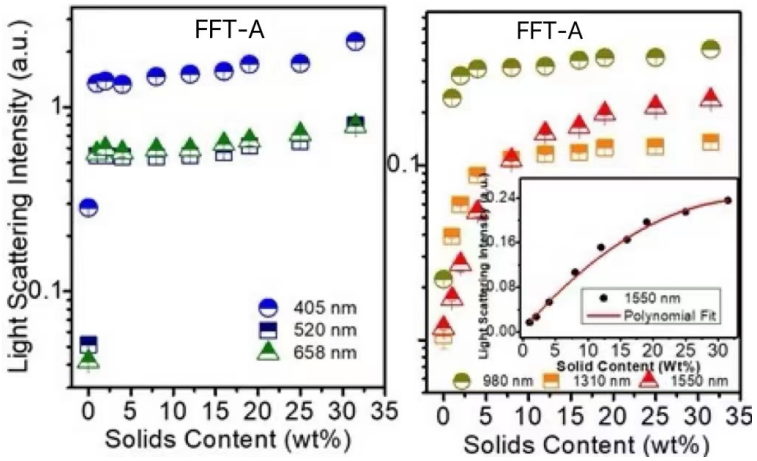

(a)

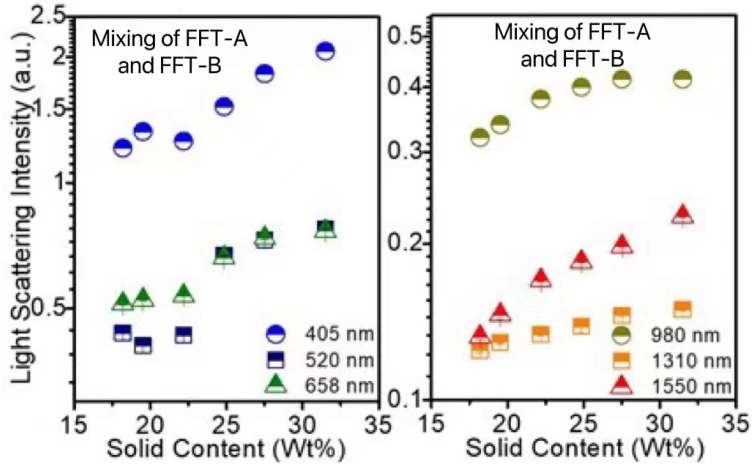

(b)

Figure 3.7: Relative change in light scattering intensity with the change in the solids content of (a) FFT-A diluted to different concentrations: (i) 405nm, 520nm and 658nm wavelengths results, (ii) 980nm, 1310nm and 1550nm wavelengths results. And (b) mixtures of FFT-A and FFT-B at different ratios. In each row the measurements had been shown for experiments conducted with: (i) visible wavelengths, and (ii) NIR wavelengths. The 0 wt% solids content in (a) represents distilled water used to test the background noise generated from the effect of the room light.[31]

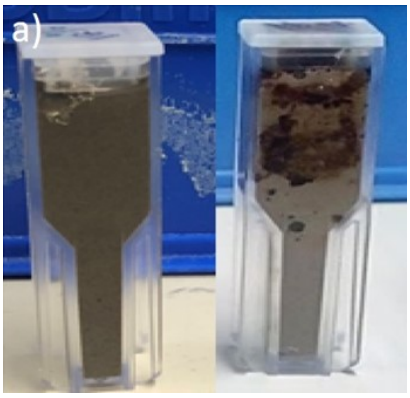

(a)

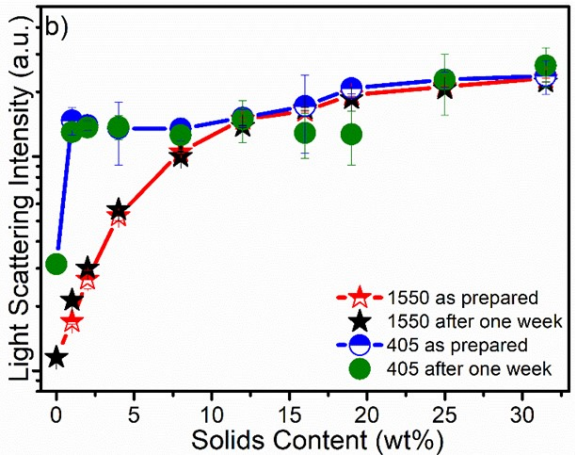

(b)

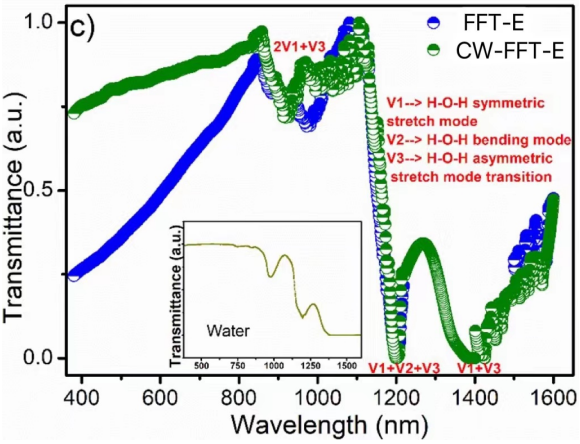

(c)

Figure 3.8: Effects of bitumen fouling on the measurement: (a) visual observations of the bitumen-fouled cuvettes (b) relative change in the light scattering intensity for as prepared and one week old bitumen-fouled samples for 405 and 1550 nm wavelengths, and (c) absorption spectra of raw and cold washed FFT-E (inset: absorption spectra of water).[31]

Lab-scale settling tank experiments were carried out with two NIR wavelength (980nm & 1550nm) LDs using Kaolin and FFT samples. The arrangement and height of the six measurement levels are shown in Figure 2.2(a). The 980nm-level6 data was abandoned because of the bitumen fouling on the laser spot position of the setup and cannot be removed. The electric current data of LDs was monitored in NIR wavelengths experiments by the current monitors described in chapter 2.

A water test (0wt%) was carried out by circuit1 before we conducted the sample experiments to compare with the results after the settling process. The tank was used to do the visible measurements, and the sample used previously was hard to remove completely. Therefore some sample particles remained in the tank and caused the water data of each level to be slightly different.

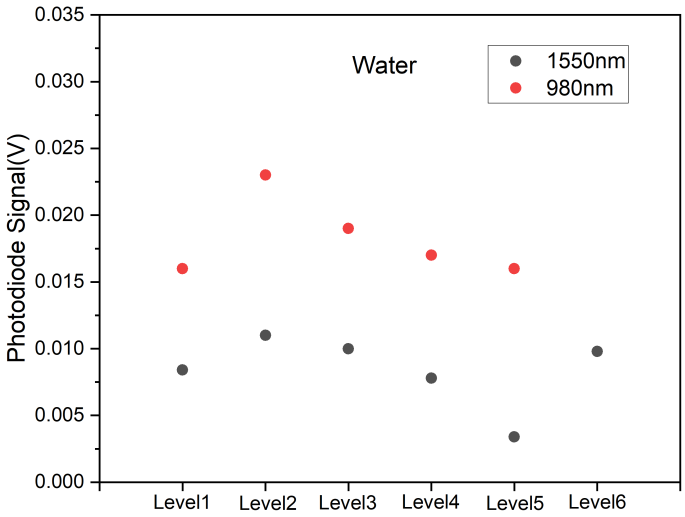

Figure 3.9: NIR wavelengths (980nm & 1550nm) water test results by circuit1.

3.3.2 Kaolin sample experiment results and discussions

The NIR experiment used the same 15wt% Kaolin sample with 600nm particle size. As seen from the Kaolin settling data (shown in Figure 3.10(a)), the 1550nm scattered light signal decreased (at transition points A, B and C for level1-3 sensors, respectively), corresponding to the settling process of solids content at the particular height. Similar to that observed for visible wavelengths, scattering intensity decreased

significantly when the water-solid interface passed through the LDs positions. Unlike previous visible wavelength experiments, noise scattered light was minor due to the strong NIR light water absorption. And after the sample settled, the light scattering signals became low due to the strong absorption by water, and the results were consistent with the water test results shown in Figure 3.9. At the third 1550nm level, there was an initial increase in the signal intensity before the signal dropped due to larger particles settled from the top levels. There was a signal drop at 1550nm-level4 at transition point D due to the sample at 4th level height starting settling. The lowest two measurement levels' signal increased with time because the larger particles settled, and the fraction rose gradually at the bottom levels leading to the slow increase of the scattered light intensity. The slow increase of bottom levels' light intensity indicated that the NIR wavelengths could detect tiny changes in solid contents in the sample. Except for the different timelines, the result curves of 980nm (shown in Figure 3.10(b)) were similar to 1550nm. Since the output power of 980nm LDs was higher than 1550nm LDs, the scattered light intensity of 980nm LDs was also larger.

3.3.3 FFT sample experiment results and discussions

The same settling tank setup also tested FFT samples. To fill the settling tank, FFT-A and FFT-C samples were diluted to 21.7wt% and 18.5wt%, respectively.

3.3.3.1 21.7wt% FFT-A experiment

This experiment used circuit1 to drive the laser system. The 21.7wt% FFT-A sample measurement results are shown in Figure 3.10, and LDs' current monitor data are shown in Figure 3.11. The gap in data on day9-12 was due to a power outage that stopped the data monitor. As seen in Figure 3.11 (a) and (b), the noise level in the FFT sample results was higher than in the Kaolin sample. One reason for high noise is the complex composition of the FFT sample, and it has small particles and bitumen droplets which cause fluctuations in the light scattering signal as they pass by the

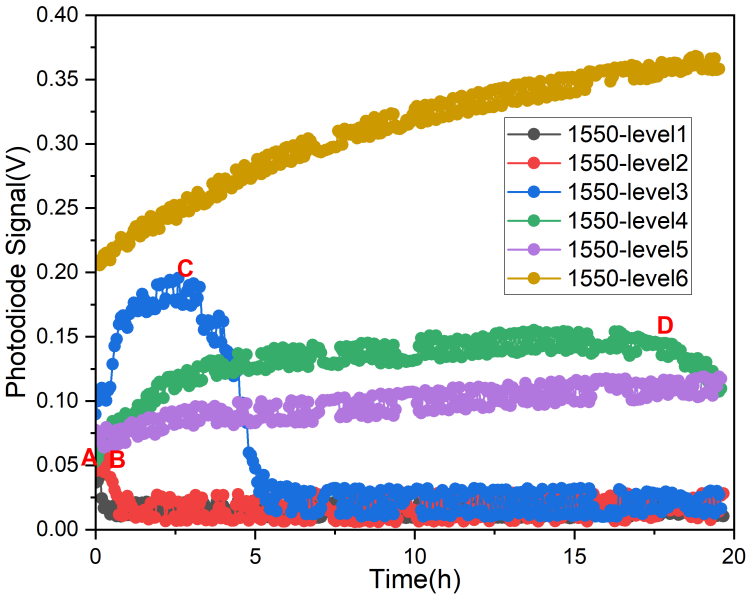

(a)

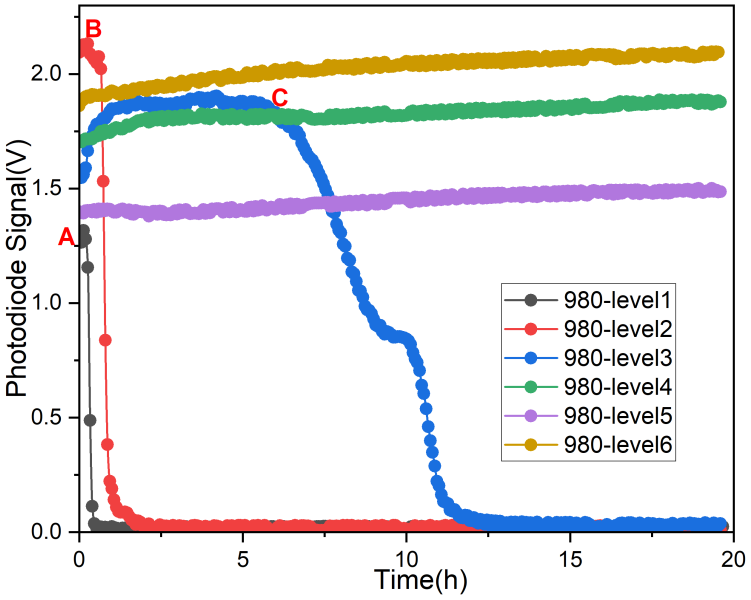

(b)

Figure 3.10: NIR wavelengths 15wt% 600nm Kaolin test results: (a) 1550nm (b) 980nm. This measurement was conducted by circuit1.

laser spot compared to the relatively homogeneous Kaolin sample. Another cause of the noisy appearance is the fluctuation in output power of the LDs driven by circuit1 (chapter 2.4.3), which can be observed in Fig 3.12.

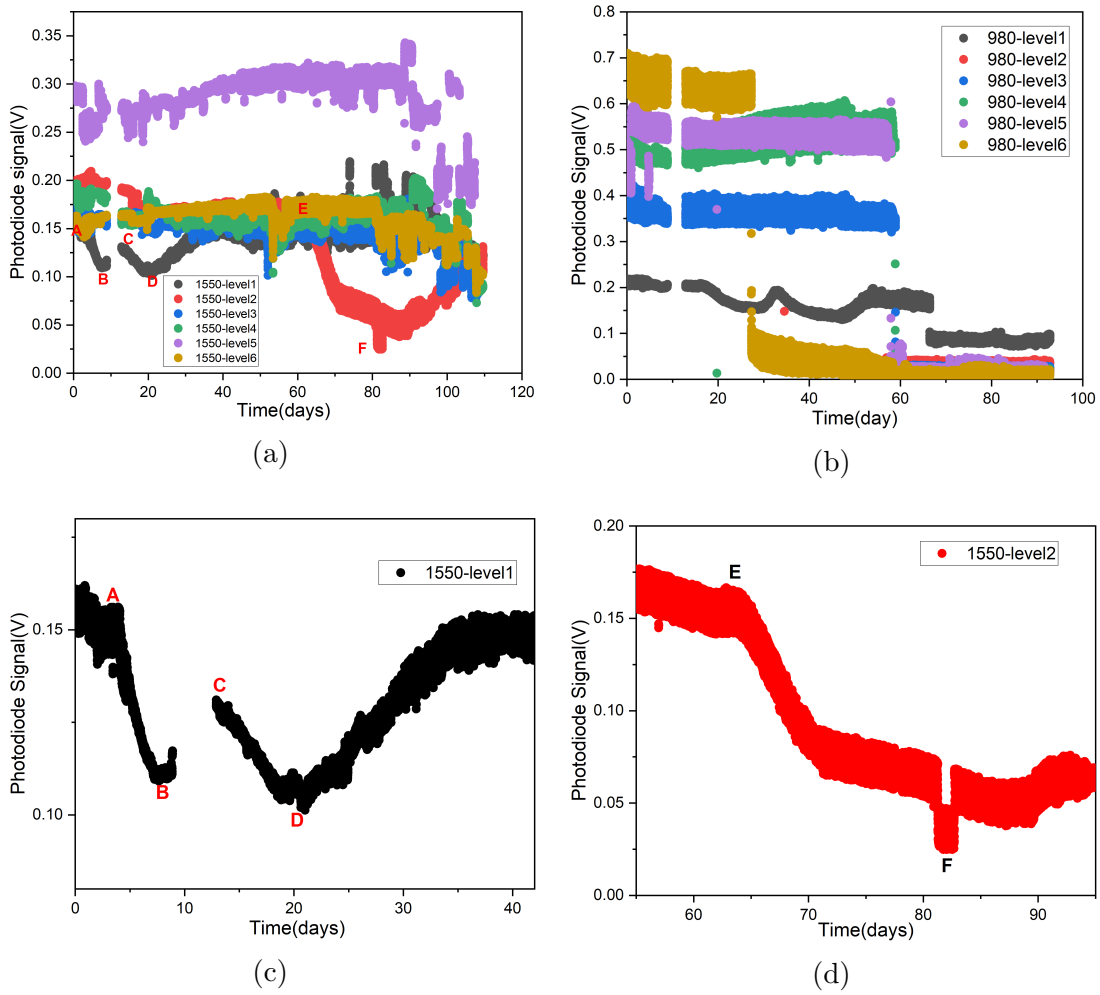

Figure 3.11: 21.7wt% FFT-A sample experiment results: (a)1550nm, (b)980nm, (c)1550nm-level1 detail result, (d)1550nm-level2 detail result. This measurement was conducted by circuit1.

In FFT-A sample measurement, it was also observed that the light scattering intensity decreased corresponding to the solids content settling process at different heights. As shown in Figure 3.11(c), the light scattering signal at 1550nm-level1 decreased from the beginning, corresponding to the sample settling at the 1550nm-level1 LD position. The larger-sized and heavier particles and particle clusters started separating and settling quickly, leading to the net drop of the signal at the transition point A. Fine

particles and oil droplets moved up into the water zone over time due to their low density, resulting in a lagging intensity increase at transition point B. The signal decreased at transition point C was because of the water evaporation. The light scattering intensity decreased with the water surface passed by the LD position. After day20, the sample surface was under the 1550nm-level1 laser. The scattered light from other sources like tank wall and sample surface dominated, resulting in an increase in scattered light intensity at transition point D.

The settling results of 1550nm-level2 were similar to the 1550nm-level1 except for the difference in the time scale and intensity. Figure 3.11(d) shows that the scattering light signal decreased when the water-solid interface moved to the 1550nm-level2 LD position. The sudden intensity decrease at the F point was caused by circuit instability and a sudden current drop. After the sample settling process, the scattered light signal of the second 1550nm LD was higher than the water test shown in Figure 3.10, indicating that fine particles remained in the water zone. According to the observation during the visible and NIR wavelengths experiments, NIR LDs were more sensitive to the unstable circuit and quickly went bad. For 1550nm LDs, the LDs current showed significant decreases at around day90.

The first 980nm LD was damaged on day23, and all of them were damaged after 65 days. 980nm LDs were out of work when the water-solid interface moved to their position. Therefore we did not get valid 980nm wavelength results. To carry out long-term monitoring of slurry samples, improvement of the LD circuit system is required. The details of the circuit improvements are discussed in chapter 2.

3.3.3.2 18.5wt% FFT-C experiment

This experiment used circuit2 to drive the laser system. The improved laser diode circuit is more stable and durable. The goal is to have a continuous and stable operation for a half year before maintenance is required. Some of the broken LDs were changed. Thus another water test was conducted before the FFT-C measurement,

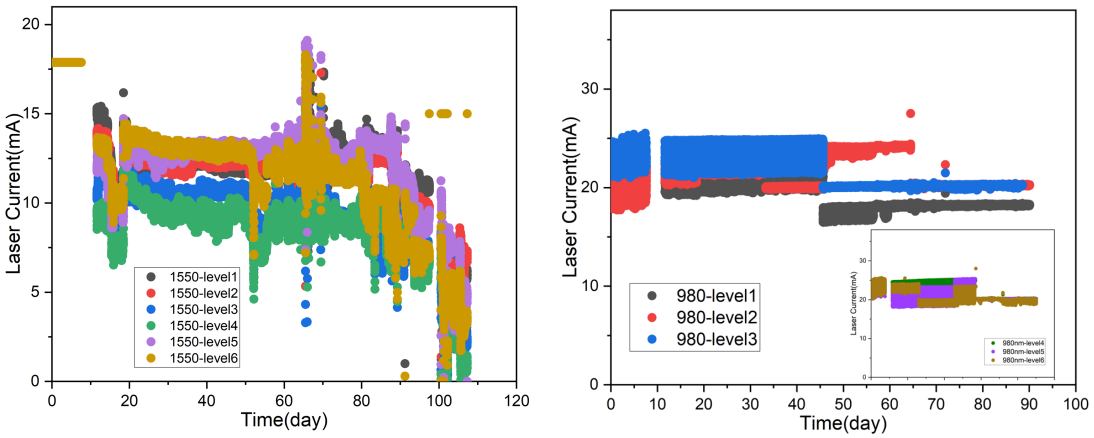

(a) (b)

Figure 3.12: LDs current moinitor data in 21.7wt% FFT-A test: (a) 1550nm (b) 980nm

and the results are shown in Figure 3.13.

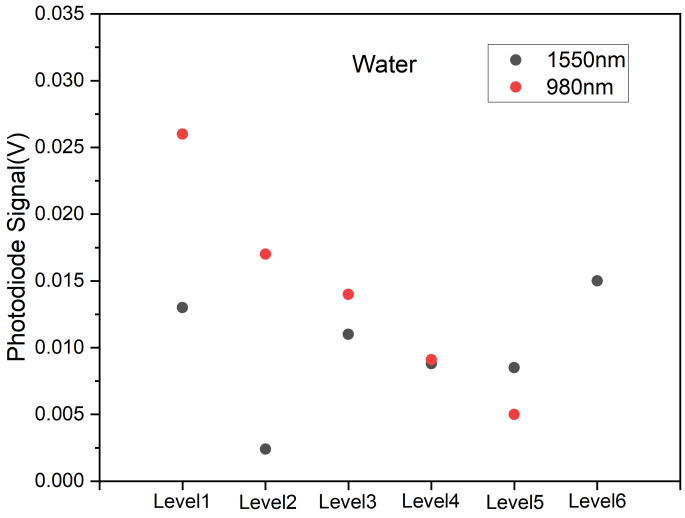

Figure 3.13: NIR wavelengths (980nm & 1550nm) water test results by circuit2.

In order to avoid water evaporation, the settling tank was sealed during the measurement. The 18.5wt% FFT-C sample measurement results are shown in Figure 3.14, and LDs current monitor data are shown in Figure 3.15. It was observed that the noise level decreased, and the lifetime of both 1550nm and 980nm LDs increased after the circuit was upgraded. Similar to the 21.7wt% FFT-A measurements, light scattering intensity changed corresponding to the sample settling, which was observed in top

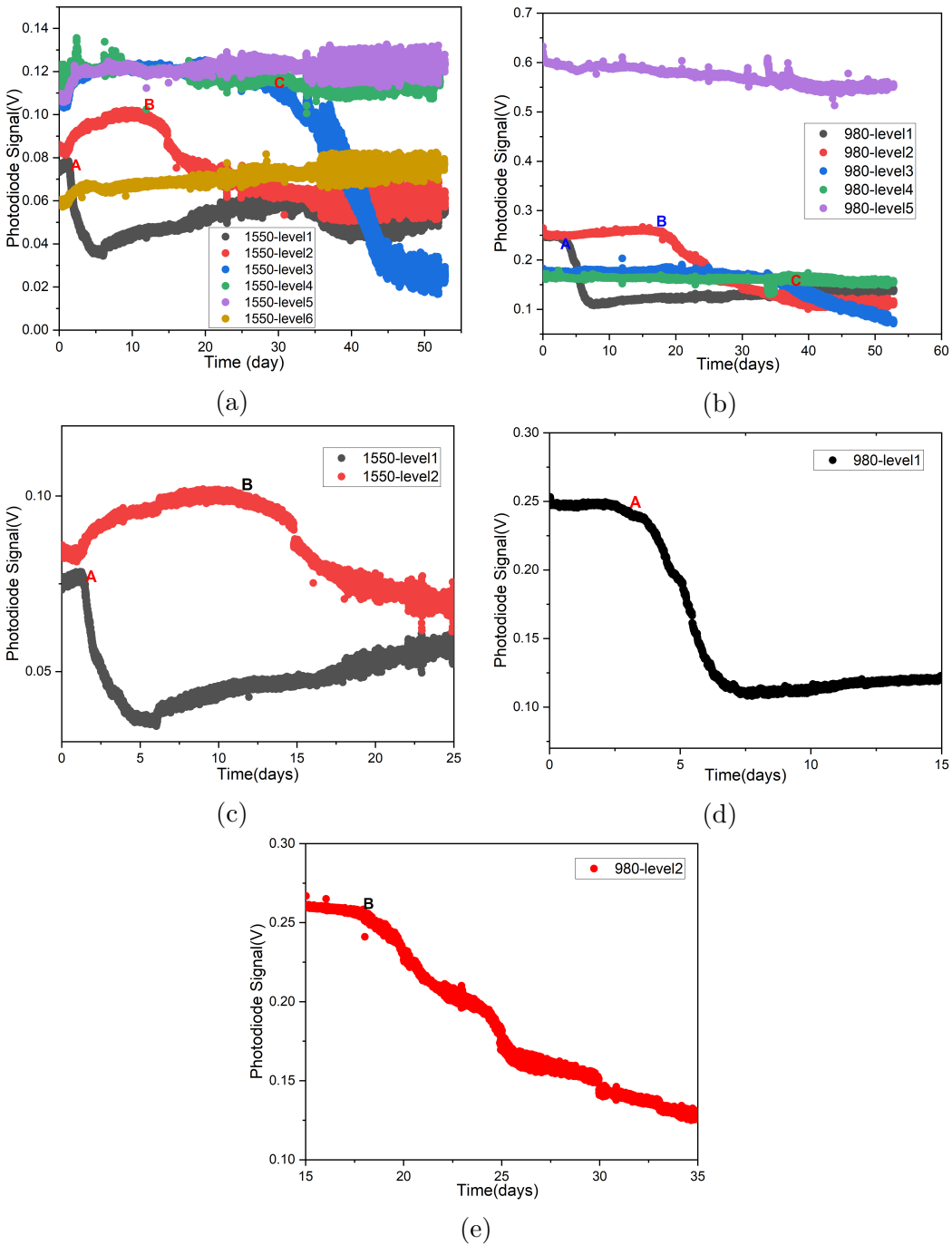

Figure 3.14: 18.5wt% FFT sample experiment results: (a)1550nm, (b)980nm, (c)1550nm-level1&2 detail results, (d)980nm-level1 detail results, (e)980nm-level2 detail results. This measurement was conducted by circuit2.

levels results. The settling characteristics of the two FFT samples were similar except for the difference in the time scales and intensities due to their different composition. Unlike the Kaolin experiment, the light scattering signal was not closed to water test results (Figure 3.13) after the sample settled due to the lighter fine particles and oil droplets remained above the water-solid interface.

The results from 1550nm sensors are shown in Figure 3.14 (a) and (c). For the 1550nm-level1 case, the signal decreased at transition point A when the water-solid interface passed through the LD position. Then the signal started to increase and became approximately constant to values higher than that for water. One possible reason is that fine particles floated up and scattered light. Based on the observation during the experiment, unlike the relative clear insertion tube observed in Kaolin test, there are bitumen and mud accumulated during the settling process covering plexiglass insertion tube near the region where LD and PD for level 1 are located. Figure 3.16 shows the picture of the insertion tube after 18wt% FFT-C sample settling experiment, the first level optical window has the most bitumen and mud deposition. Hence another possible reason is that the thick bitumen and mud fouling accumulated over time would scatter light and increase the measured light scattering intensity. At transition points B and C, the level2 and level3 sensors data dropped correspond to the sample settling. As shown in Figure 3.16, there were less bitumen and mud covering the region where the level2 and level3 sensors are located. Hence there are no increases observed following with the decrease in scattering light intensity. At level3 optical window position, the insertion tube was relatively clear, thus level3 observed the lowest scattering intensity after settling process. The scattering from the bitumen and mud fouling need further investigation. The scattered light intensity of level4-6 increased slightly at the beginning probably due to the large particles settling downward.

Except for the different time scales and intensity, the level1 and 2 980nm results (shown in Figure 3.14(d) and (e)) were similar to 1550nm. No significant changes in

the level4-6 signal since the sensitivity of 980nm is not as high as 1550nm, and small changes in solids content would not be detected.

Figure 3.14(a) shows that the noise level increased on day35. These changes were caused by loose wire connections over time in the sensor circuits. In Figure 3.15 (a) and (b), the current drop of level1 1550nm LD and three current drops of 980nm LDs were the results of wire connection issue of the current monitor. To solve these problems, a soldered circuit was built to make it more robust. The soldered circuit board will be tested in future experiments. Another issue of the circuit that needs to improve is discussed below. The initial sample was considered homogeneous. Thus all the levels' initial light intensity was expected to be the same. Obviously, this was not the case in our experimental results. The reason is that the output light intensity of the LDs was different. Although the LDs operated under constant power mode, their output power was not guaranteed to be the same due to the different characteristics of each LD. To solve this problem, the circuit design needs further optimization in the future. The calibration of settling tank results will be discussed in the next chapter.

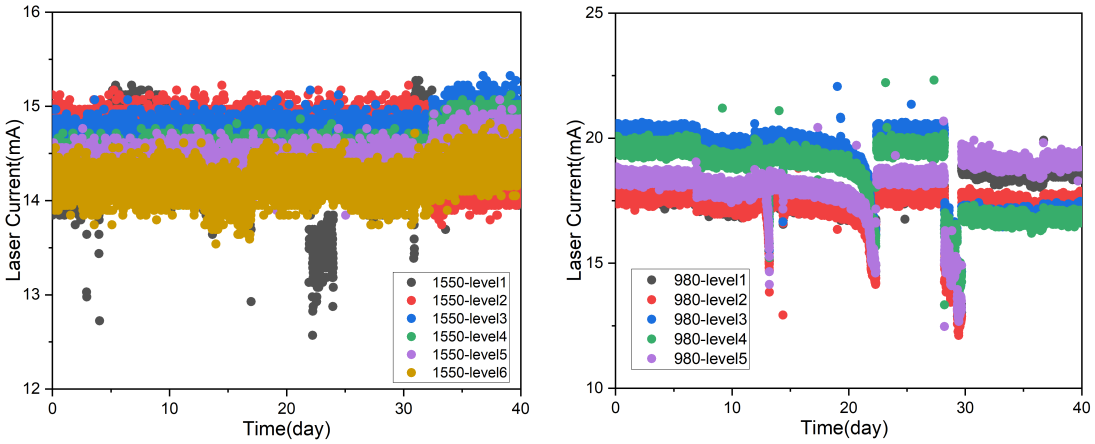

(a) (b)

Figure 3.15: LDs current moinitor data in 18.5wt% FFT-C test: (a) 1550nm (b) 980nm

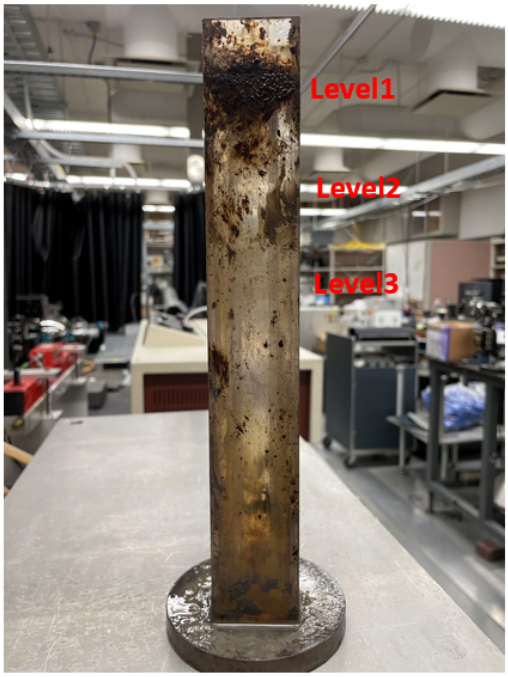

Figure 3.16: The picture of the insertion tube after the two months 18wt% FFT-C sample settling experiment.

Chapter 4

Calibration

Calibration of the optical solids content sensor is essential in this thesis. This chapter focus on five parts: (a) Experiments that were conducted using the calibration ring to optimize the best observation angle. (b) Calibration ring and calibration tank experiments were carried out to obtain calibration curves that can be used to convert light scattering signal data into solids content in wt%. (c) Discussion on the sensitivity of the optical sensor (1550nm). (d) Several experiments were conducted to find the correction factors due to variations in laser diode powers and photodiode sensitivities. (e) Comparison of results for settling tank experiments from the optical sensor and the gamma-ray sensor.

4.1 Calibrtion ring

To accomplish the angular distribution and calibration measurement, a ring setup was built (shown in Figure 3.1(b)). The incident laser diode was placed at the 0° position and focused on the surface of the sample cuvette. A cuvette with a slurry sample was positioned at the center of the ring. A photodiode was used to measure scattered light signal at different angles up to 90°. This setup is described in detail in chapter 2.1.

As discussed in chapter 2.2, angular distribution measurements were carried out to find the optimum observation angle of the scattered laser light signal using the cali-

bration ring setup.

Additionally, the sample settling experiments did not provide an absolute measurement of the solids content. Calibration measurements, such as those described below, are required to convert the signal into an absolute solids concentration. Calibration measurements were conducted using the calibration ring at the 20° backscattering angle.

Kaolin and FFT samples were used in the experiments. Laser diodes with different wavelengths (405nm, 658nm, 980nm and 1550nm) from Thorlabs were used. 405nm and 658nm LD were driven by the commercially available laser driver board FL591FL from Team Wavelength. 980nm LD and 1550nm LD were driven by a homemade MLD203P1E and MLD203P2E laser driver circuit, respectively. The MLD203P1E and MLD203P2E chips are from Thorlabs. Data acquisition was handled by a TDS210 oscilloscope from Tektroix.

4.1.1 Angular distribution of laser scattered light intensity measurements

Several experiments were carried out to determine the best observation angle using the ring setup. By using the ring setup, the scattered laser light intensities from a sample were measured from 10° to 80° with a 10 degree step. The experiments were carried out on both sides of the laser axis i.e. +/- 10 degree, +/- 20 degree ... etc. Due to the design of the calibration ring, measurements were done from 10° to 80° in the counterclockwise direction and from 10° to 60° in the clockwise direction. In general, the results from both sides agreed with each other. For each angle, ten measurements were conducted to obtain the standard deviation. The 25 wt% Kaolin with 600nm particle size, 25 wt% FFT-D (sample composition shown in Table 3.1), and water (0wt%) were measured. The angular test results are shown in Figure 4.1. The cos power law fit curves of Kaolin and FFT were obtained by averaging the results from both sides (shown in Figure 4.2).

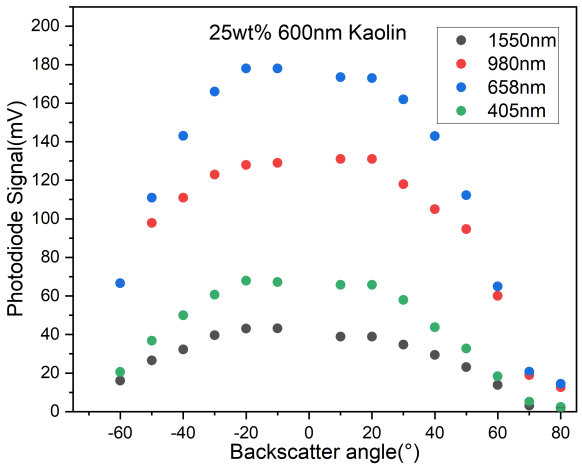

(a)

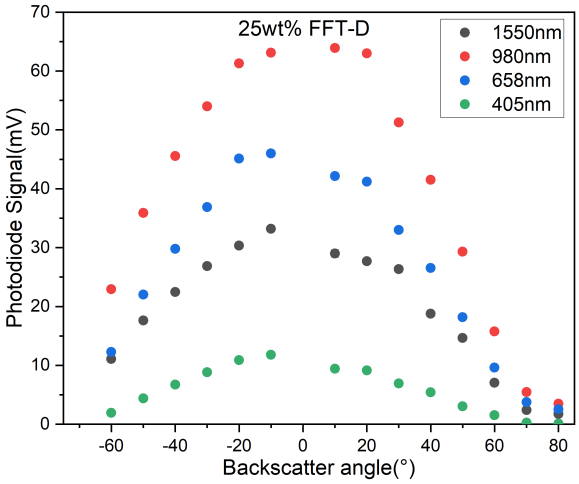

(b)

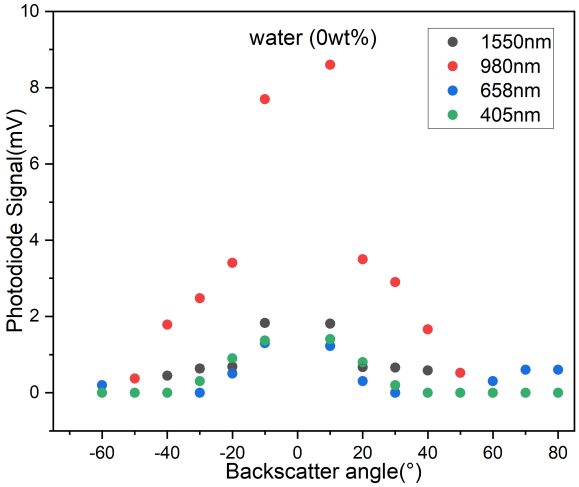

(c)

Figure 4.1: Light scattering signals from slurry samples and water as a function of angle: (a) 25wt% 600nm Kaolin sample (b) 25wt% FFT-D sample (c) water (0wt%). Measurements were conducted using 405nm, 658nm, 980nm and 1550nm LDs.

For the 25wt% 600nm Kaolin samples, the scattered laser light intensities decreased with the increase in the angle between the laser axis and photodiode (Figure 4.1(a)) for all wavelengths. The intensity was highest at the smallest observation angle of 10°. As shown in Figure 4.1(b), similar to the Kaolin sample, the scattered laser light intensity from the FFT sample was the highest at 10° and decreased with the increase in the angle for all wavelengths. According to the Lamberts law, the angular distribution of scattered light from an ideal diffuser follows the cosine law $I = I_0 cos(\theta)$, where I is the scattered light intensity at an observation angle θ and I_0 is the maximum scattered light intensity at θ=0.[33] Non-ideal diffusers such as slurry samples deviate from the cosine law and follow $I = I_0 cos^n(\theta)$.[40] For the 25wt% 600nm Kaolin sample measurement, n was 1.9, 1.9, 1.3 and 1.7 for 405nm, 658nm, 980nm and 1550nm wavelength, respectively (shown in Figure 4.2(a)). For the 25wt% FFT-D sample measurement, n was 1.9, 1.6, 1.8 and 1.8 for 405nm, 658nm, 980nm and 1550nm wavelength, respectively (shown in Figure 4.2(b)). As shown in Figure 4.1(c), the water (0 wt%) test results showed large scattered light signal at 10° than at other angles. Tap water was used to dilute the sample in this measurement so that some of the scattering signals came from the particles in the tap water. And some of the signals at small angle came from the specular reflection of the cuvette walls. The 20° scattered light angle was chosen because its best compromises between the high scattered light signal (depend on $cos^n(\theta)$) and the insignificant signal from specular reflection. Therefore, in the design of the optical sensors, the angle between laser diode and photodiode was set as 20°.

4.1.2 Light scattering measurements with different solids content at backscattering angle of 20°

The settling tank measurements allow the measurements of the relative changes in solids content but can not determine the absolute solids concentration in wt%. Calibration factors are needed to convert the scattered light signal into absolute solids

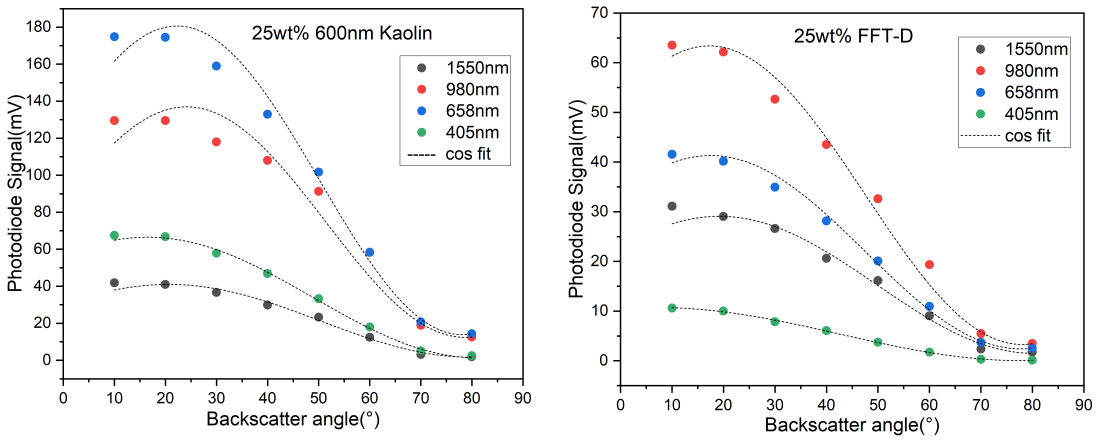

(a) (b)

Figure 4.2: Light scattering signals from slurry samples as a function of angle: (a) 25wt% 600nm Kaolin sample (b) 25wt% FFT-D sample. The black dot lines are cos fit curve. Measurements were conducted by 405nm, 658nm, 980nm and 1550nm LDs.

content. In principle, Mie theory can be used to determine the calibration factor if the sample is a single spherical scatterer. Since the samples in our experiments typically consisted of many particles and they are irregular in shape, Mie theory is invalid. The development of sophisticated models that can yield calibration factors for complex materials would require major efforts. We decided to obtain the calibration factors empirically. The samples for the calibration ring setup were progressively diluted and measured to empirically find the relative change in light scattered intensity when there was a change in solids content.[27] Kaolin sample with 600nm particle size was available as dry powder. The highest solids content tested was around 40wt% because it is difficult to make a homogeneous sample beyond 40wt%. FFT-A sample (see table 3.1) with 31.5 wt% solids content was diluted to different concentrations by mixing it with tap water. The 0 wt% solids content (water) was used to test the background noise generated from the effect of the room light and the scattering light from tap water, and the results are shown in the tables inset in Figure 4.3. There are small particles in tap water, such as minerals and dusk, and the scattering light from these particles is relatively small, as shown in Figure 4.3, and can be ignored. Changes in light scattering signal for 405nm, 658nm, 980nm and 1550nm wavelengths with solids

content changes were analyzed by examining data at 20°. These experiments were conducted by Dr. Tulika Srivastava in our group, and the results are shown in Figure 4.3.

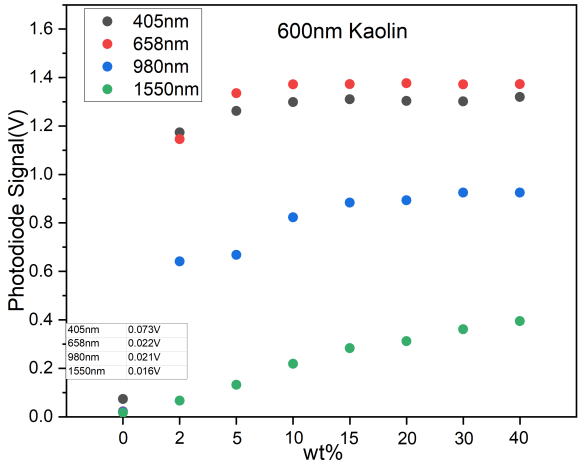

(a)

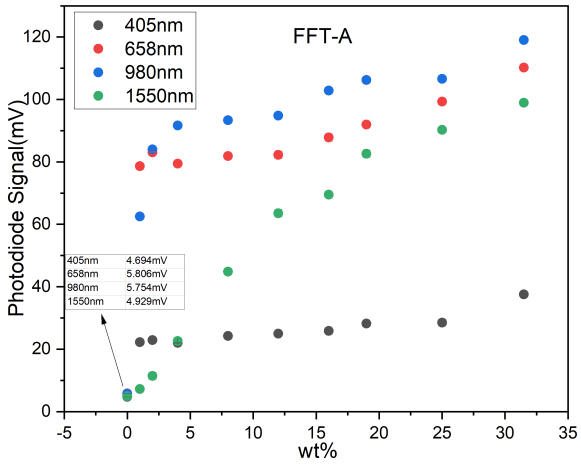

(b)

Figure 4.3: Relative changes in light scattering intensity with the change in the solids content at 20° backscattering angle (a) 600nm Kaolin sample (b) FFT-A sample. Measurements were conducted by 405nm, 658nm, 980nm and 1550nm LDs.

Generally, for all wavelengths, increase in the scattered light intensity corresponded to the increase in the solids content of a Kaolin or an FFT sample. However, for Kaolin samples, as shown in Figure 4.3(a), visible wavelengths (405nm and 658nm) were not sensitive at solids content >10wt%, as changes in the light scattering intensity were relatively small. Compared to 980nm, 1550nm demonstrated more noticeable scat-

tering intensity changes at high solids content. For FFT samples, as shown in Figure 4.3(b), the 405nm and 658 nm wavelengths were not sensitive at concentration <10 wt%, and the scattering intensity remained almost constant. On the other hand, the 980 nm wavelength was sensitive for low FFT concentrations, but the light scattering intensity became nearly saturated for solids content >10wt%. With a noticeable change in the scattering intensity at all test ranges, the 1550nm demonstrated the best sensitivity among all the wavelengths tested. In summary, using this ring setup calibration data, the relative change in light scattering intensity can be converted to the sample concentration. The 1550nm wavelength demonstrated the most consistent scattered light intensity increase with the variation of the solids content.

4.2 Correction factors for settling tank and calibration tank setups

In chapter 3, the experimental results of the FFT sample settling measurements using NIR (980nm and 1550nm) wavelengths were discussed in detail. Since we believe that the samples were agitated thoroughly before the experiment and the LDs worked under constant power mode, the initial experimental values of all 6 levels were expected to be the same. However, the initial values of the 6 levels were not the same (shown in Figure 3.14). Several tests were conducted to understand this.

4.2.1 LD power test

The LD output power was measured by a PM400 power meter using an S302C thermal power head from Thorlabs. The distance between LD and the power meter was 0.5cm. The beam size of 1550nm LD at 0.5cm is around 0.5mm x 0.6mm, and 980nm LD is approximately 0.2mm x 0.5mm. The beam sizes are significantly smaller than the 12mm x 12mm aperture size of the S302C thermal power head, and the power meter was centered by visible inspection to maximize the measured power signal. Power measurements for all LDs were conducted three times, and the results for all sets were

consistent with a small standard deviation, as shown in Table 4.1. Two groups of LD power measurements were conducted, one group was before the FFT-C sample settling experiment (described in chapter3.3), and another group was before the Teflon test described below. Test 2 was carried out several months after test 1, and during this time these LDs were used for other tasks including calibration tank measurements, etc. It was observed that variations of LD power could occur after using the LDs over a period of time. Before FFT-C sample settling tank measurements, the variations of six levels of 1550nm LDs power were within 53%, and the variations of five levels of 980nm LDs were within 36%. The variation in LD power was because when the laser control circuit was designed, all the same wavelength LDs were driven by one LD driver because of cost concerns. Only one PD current was able to set for one LD driver which is used in the constant power feedback loop. However, the characteristic of each laser diode is different, and the same output power requires different PD current settings. The circuit can be improved in the future by driving the LDs with a one-to-one LD driver. After a couple of months, the power of 1550nm LDs reduced except for the level4 and level6 LDs. The 1550nm LD power variations increased to within 66% instead of 53% in test 1 previously. The level1 and level4 of 980nm LDs power increased, and other levels LDs power decreased after several months. The 980nm LD power variations increased to within 51% instead of 36% in test 1.

4.2.2 PD sensitivity test

The sensitivity of 6 PDs was tested by a 1550nm LD with 2.5mW constant output power. The schematic of the setup used to measure PD sensitivities is shown in Figure 4.4. The LD and PDs were installed in the metal sensor tube, which was used in the settling tank experiments (shown in Figure 2.2(d)). A piece of Teflon, as a perfect Lambertian reflector, was placed in front of the LD and PDs. An additional reference PD was set adjacent to the measured PDs to monitor the output of the 1550nm LD. The distance between the measured PDs and Teflon was 5cm, and the distance

Table 4.1: Results of LDs power test: (a) 1550nm, (b) 980nm. Power test 1 was conducted before FFT-C sample settling tank measurement and power test 2 was conducted before Teflon test.

NO.	Power test 1	STDEV	Power test 2	STDEV
1550nm-level1	3.10	0.010	2.50	0.042
1550nm-level2	3.20	0.030	2.30	0.079
1550nm-level3	3.63	0.019	3.60	0.064
1550nm-level4	5.56	0.010	6.29	0.111
1550nm-level5	2.96	0.003	2.15	0.089
1550nm-level6	2.11	0.071	2.49	0.083

(a) 1550nm

NO.	Power test 1	STDEV	Power test 2	STDEV
980nm-level1	10.25	0.290	10.68	0.424
980nm-level2	12.60	0.013	8.6	0.456
980nm-level3	9.17	0.089	8.74	0.261
980nm-level4	11.60	0.410	17.56	0.199
980nm-level5	14.30	0.103	11.85	0.107

(b) 980nm

between the measured PDs and the reference PD was 2cm. The load resistance of the bias circuit (Figure 2.14) for level1 to level6 PD was 382, 372, 735, 735, 751 and 749 kΩ, respectively. During the measurement, the positions of measured PDs were fixed, and the 1550nm LD and the reference PD were changed to different levels. The results are shown in Table 4.2. The reference PD signal at six levels was consistent, indicating that the output power of the 1550nm LD was constant and the scattered light received by the six measured PDs was similar. PD signal is proportional to the load resistance. Level1 data was used as the benchmark and calculated the PD relative sensitivity of each level by dividing the load resistance value. The variation of PD sensitivities from level1, 2, 3, 5, 6 were small and within 6%, but the one from level 4 was relatively large and around 40%. During the measurements, the reverse-biased level4 PD gave an offset of around 70mV and then increased to around 220mV, which indicated that the PD might not operate properly and became worse over time. The level4 PD exhibited very low sensitivity and will need to be replaced in future experiments.

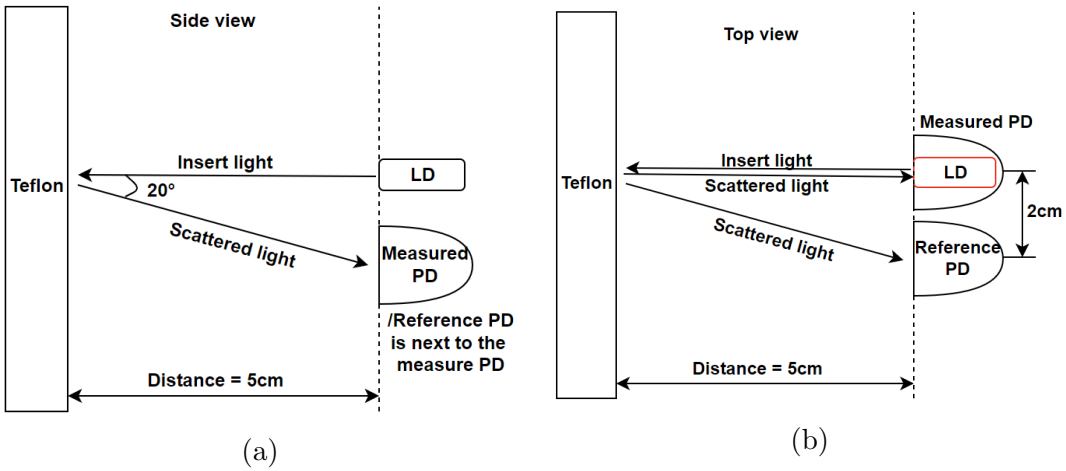

Figure 4.4: Schematic diagram illustrates the PD sensitivity test setup with a reference PD and one pair of the LD-PD: (a) Side view of the setup, (b) Top view of the setup.

Table 4.2: Results of 6 levels PD sensitivity test using 1550nm laser diode with output power of 2.5mW

PD NO.	Measured PD signal(MV)	Reference PD signal(mV)	Load resistance(kΩ)	PD relative sensitivity (Correction factor)
PD-level1	139.8	78.5	382	1
PD-level2	130.5	79	372	0.959
PD-level3	253.1	78.8	735	0.941
PD-level4	162.3	79.2	735	0.604
PD-level5	276.2	79.8	751	1.005
PD-level6	267.5	79	749	0.976

4.2.3 Teflon test

All the six levels of LDs and PDs were tested together with Teflon. The same PD sensitivity measurement setup was used except without the reference PD (shown in Figure 4.5). The distance between Teflon and the sensor mount was 5cm. In order to reduce the background noise of the room light, the setup was covered by a black box. The LDs were pulsed using the same circuit2 as in the settling tank experiments. The LD at each level was pulsed with 20s at on-states and 10s off-states in between. Six levels of 1550nm LDs and five 980nm LDs were tested. The 980nm-level6 data was abandoned because the laser was destroyed during a settling tank experiment when the slurry sample leaked into the insertion tube and shorted the 980nm laser at level6. The load resistances of the bias circuit (Figure 2.14) for level1 to level6 PD were all around 750 kΩ. To investigate the errors from minor changes during the setup installation, such as minor changes in distance and angle, the experiment was conducted twice by removing the Teflon and then remounting it, which is shown in Table 4.3 as Teflon1 and Teflon2. The measurement lasted 30 minutes continuously, and 5 data sets were obtained to get the standard deviation.

The DAQ device retrieved the signal from PDs.

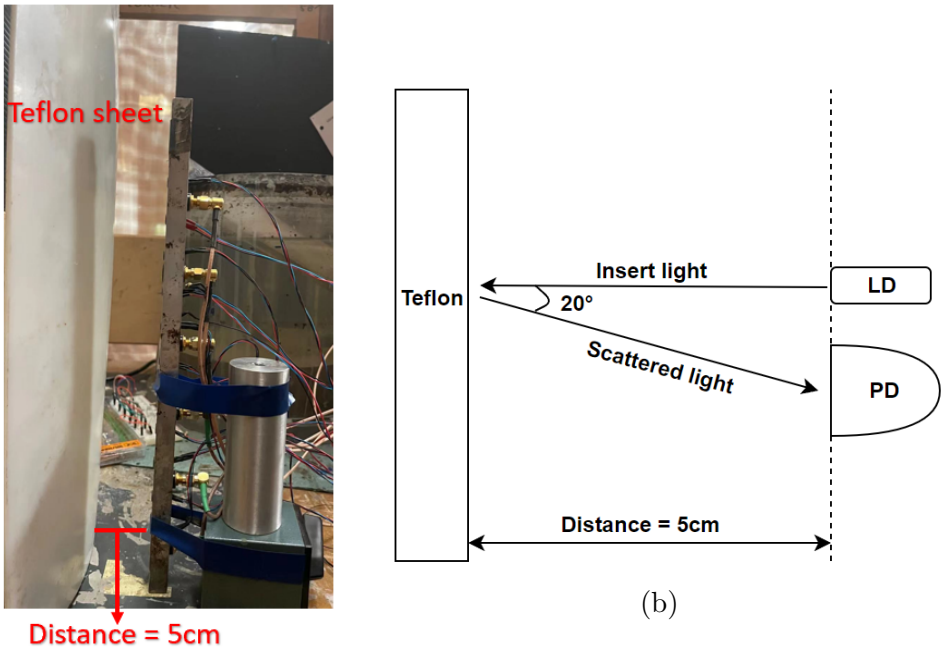

Figure 4.5: Teflon test setup: (a) picture of the overall setup, (b) schematic diagram illustrates the test setup for one of the LD-PD pairs.

4.2.4 Correction factors

LD and PD correction factors were calculated by the LD power and PD sensitivities. Using level1 data as the benchmark, the factors of other levels were obtained by proportional calculation for 1550nm, 980nm LDs, and PDs. The LD correction factors calculated using the data from table 4.1 are shown in Table 4.4. In addition to the PD sensitivity test, other experiments including settling tank experiments, calibration tank measurements and Teflon test were conducted with the PD biased circuit using 750kΩ load resistance for all six levels. The PD relative sensitivity shown in column4 data from table 4.2 were corrected by load resistance value shown in column3 data. Therefore, PD sensitivities can be used as PD correction factors.

The LD and PD correction factors were applied to the Teflon test results to verify their reliability. The LD power test 2 was done shortly before the Teflon test, thus

Table 4.3: Results of Teflon test using setup shown in Figure 4.5 with 1550nm and 980nm LD

LD NO.	PD signal(V)-Teflon1	STDEV	PD signal(V)-Teflon2	STDEV
1550nm-level1	0.145	0.008	0.139	0.0010
1550nm-level2	0.130	0.0006	0.119	0.0008
1550nm-level3	0.184	0.003	0.190	0.0019
1550nm-level4	0.226	0.0025	0.230	0.0036
1550nm-level5	0.128	0.0018	0.120	0.0016
1550nm-level6	0.138	0.0008	0.128	0.0011

(a) 1550nm

LD NO.	PD signal(V)-Teflon1	STDEV	PD signal(V)-Teflon2	STDEV
980nm-level1	2.17	0.026	2.10	0.018
980nm-level2	1.73	0.006	1.64	0.010
980nm-level3	1.69	0.016	1.75	0.034
980nm-level4	2.38	0.019	2.34	0.023
980nm-level5	2.41	0.059	2.36	0.045

(b) 980nm

Table 4.4: LD correction factors of (a) 1550nm and (b) 980nm from level 1 to 6 using data from table4.1

NO.	LD correction factor 1	LD correction factor 2
1550nm-level1	1	1
1550nm-level2	1.03	0.92
1550nm-level3	1.17	1.44
1550nm-level4	1.79	2.52
1550nm-level5	0.95	0.86
1550nm-level6	0.68	1.00

(a) 1550nm

NO.	LD correction factor 1	LD correction factor 2
980nm-level1	1	1
980nm-level2	1.23	0.81
980nm-level3	0.89	0.82
980nm-level4	1.13	1.64
980nm-level5	1.40	1.11

(b) 980nm

the LD correction factor 2 was utilized here. The PD signal depends on the LD power and the PD sensitivity for each level. After correcting for the relative differences of LD power and PD sensitivity, the Teflon test results (the average of two sets of the test) of six levels should be similar. The correction was done by dividing the product of the LD and PD corrections factors. After correction (Table 4.5), the variation of six levels of 1550nm Teflon results was within 7.4%, while the variation of 980nm results was within 6.4%. These variations might come from errors in LD power or PD sensitivity test or Teflon slices that are not perfectly flat. These variations are reasonable, indicating that the LD and PD correction factors can be used to correct raw settling tank experimental data.

Table 4.5: Teflon test results corrected by LD and PD correction factors: (a) 1550nm results, (b) 980nm results.

NO.	Teflon test results(V)	Teflon test results after correction(V)
1550nm-level1	0.142	0.142
1550nm-level2	0.124	0.140
1550nm-level3	0.187	0.138
1550nm-level4	0.228	0.149
1550nm-level5	0.124	0.143
1550nm-level6	0.133	0.137

(a) 1550nm

NO.	Teflon test results(V)	Teflon test results after correction(V)
980nm-level1	2.136	2.136
980nm-level2	1.684	2.168
980nm-level3	1.722	2.232
980nm-level4	2.360	2.282
980nm-level5	2.389	2.141

(b) 980nm

4.2.5 Correction for FFT-C sample settling experiment results

The correction factors were applied to the FFT-C sample settling experimental results (Figure 3.14). The LD power test 1 was done shortly before the FFT-C settling tank measurement. Hence LD correction factor 1, shown in Table 4.4, was used. PD sensitivities shown in Table 4.2 column4 were used as PD correction factors. The correction results were obtained by dividing the original data by the product of the LD and PD correction factors. After correction (Figure 4.6(a)), the variation of the initial points of six levels 1550nm decreased from 47% to 30.6%. The variations of the starting point of six levels 980nm from original data were relatively large and around 3.8 times. After correction (Figure 4.6(b)), the variations were around two times. The initial values of six levels are shown in the table of figures. Even after the correction, the starting point value of 1550nm and 980nm settling tank results were not the same. The LD and PD correction factors do not work well. One possible reason is that the insertion tube was reused several times, and some residual bitumen coatings may be left on the insertion tube. The optical properties of the insertion tube at various sensor locations may vary due to the residual bitumen coatings and/or scratches. The larger deviations for the 980nm case versus 1550nm would be consistent with bitumen fouling. Another possible reason is that there was a large time gap between the correction factors tests and the sample settling experiments. The conditions of LDs and PDs may change due to the circuit drifting. In future experiments, correction factors tests should be conducted right before and after any sample settling experiment, and the transmissions of the optical windows at various levels will need to be measured before and after experiments.

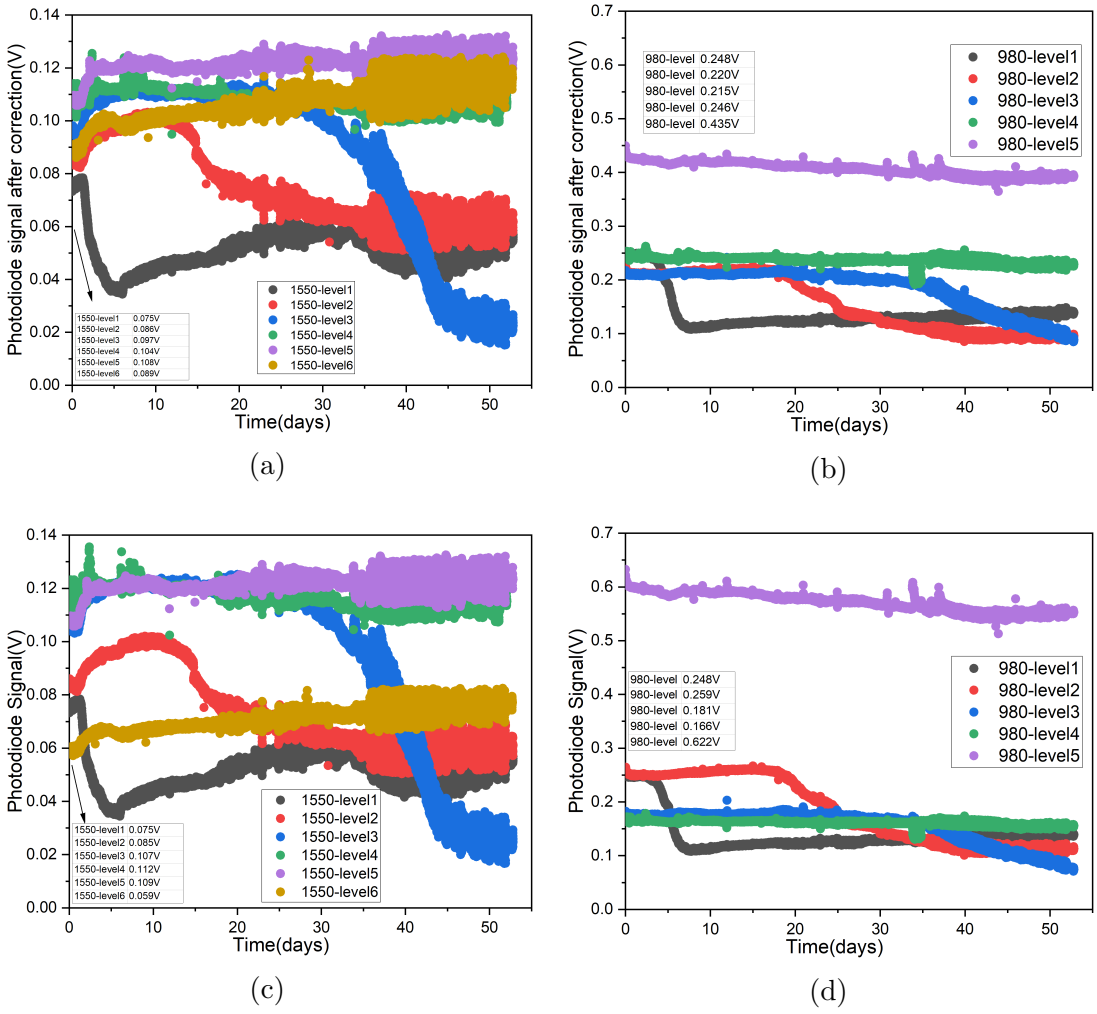

Figure 4.6: Corrected settling tank experiments (a) 1550nm (b) 980nm. Original settling tank experiments data (c) 1550nm (d) 980nm. FFT-C sample with initial solids content of 18.5wt% was measured. The tables in the figures show the starting value of each level.

4.3 Calibration of the optical sensor

4.3.1 Calibration tank measurements

A calibration tank was developed to keep the conditions as close as the settling tank experiment and convert light scattering signal into solids content in wt%(shown in Figure 2.3). Compared to the large setting tank with a volume of 30L, the calibration tank has a smaller volume of 2.8L, which is easier to homogenize the samples. Various samples with different solids content were prepared by diluting samples from higher solids content with tap water. Calibration experiments were conducted by both circuit1 and 2 (details are described in chapter2). Three levels - 30cm, 20cm and 10cm from the bottom were measured. Same as the settling tank experiment, the LD at each level was pulsed on for 20s alternately with a 10s delay in between. For each solids concentration, experiments were conducted three times and 10 minutes for each. Due to the fast sample settling rate in the calibration tank, the sample was agitated thoroughly before each test.

First, the calibration tank measurement was done by circuit1. However, we did not get the expected data curve (shown in Appendix B). As discussed in chapter 2, circuit1 was not commonly grounded, and the 980nm LD driver did not match the 980nm LD's case common grounded manufacturing requirement, and the signal obtained may not be accurate. Therefore, we improved the circuit to circuit2. Then the calibration tank measurement was conducted by circuit2. The initial concentration of the FFT-C sample is 32wt%. Then FFT-C were diluted with tap water to concentration of 30%, 24%, 18%, 14%, 8%, 2%, 0% where 0% is tap water.

1550nm and 980nm LDs were used. The results shown in Figure 4.7 are raw data. Due to the correction factors not work well for the settling tank experiment, hence we use raw calibration tank data here to create calibration functions. Note the effect of not including correction factors is small since the differences of LD power and sensitivity of PD between level1 and level2 are relatively small comparing with other levels.

As shown in Figure 4.7(a), the 1550nm wavelength level1 result curves demonstrated increasing trends with the increase of solids content for all concentrations. For level2, an increasing trend appeared at the sample concentration lower than 30wt%, whereas the light scattering decreased at >30wt%. FFT slurry sample with a concentration over 30wt% was challenging to agitate and make homogeneous. For both level1 and 2, the lower concentration data agreed better. The growth percentage between two concentrations of two levels under 30wt% were similar (Table 4.6), including that the slurry sample with lower solids content was likely more homogeneous. The results of the third level, at the bottom of the tank, did not show the same trend as those of the first and second levels. Since the small volume of this tank, we can only mix the samples by hand. Due to the limitations of manual mixing, it is impossible to ensure that the bottom layer concentration of the sample is same with the top layers. Some large particles may be deposited at the bottom and cannot be brought to the upper level by hand mixing. Therefore the experimental results of level3 may have a large error compared to the actual concentration. Thus the level3 data was discarded.

For three level's 980nm results shown in Figure 4.7(b), similar to the calibration ring results at 20° scatter position (Figure 4.3(b)), a sharp increase occurred at solids concentration <10wt% and became almost saturated for solids content >10wt%, indicating the 980nm wavelength was only sensitive to low FFT concentrations. The large differences of the scattered light signals among the different depths for solids content larger than a few wt% will need further investigations.

4.3.2 Calibration functions

During the water (0wt%) test, it was observed that small particles remained in the calibration tank. Hence the water data was abandoned in the calibration curves. The 1550nm and 980nm calibration curves (Figure 4.8) from 2wt% to 30wt% were obtained by averaging data from level1 and level2. The calibration function for the 1550nm case (equation 4.1) was determined by fitting a second order polynomial to

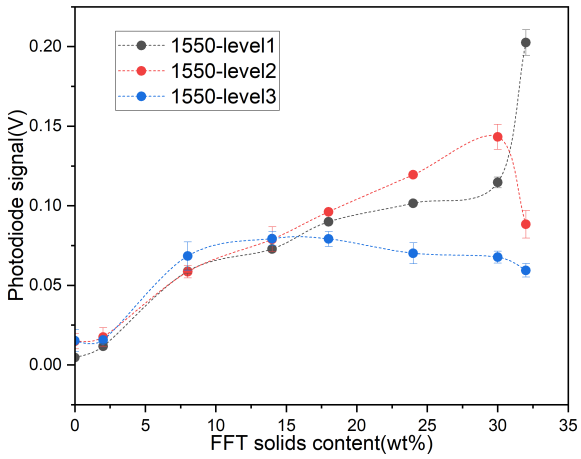

(a)

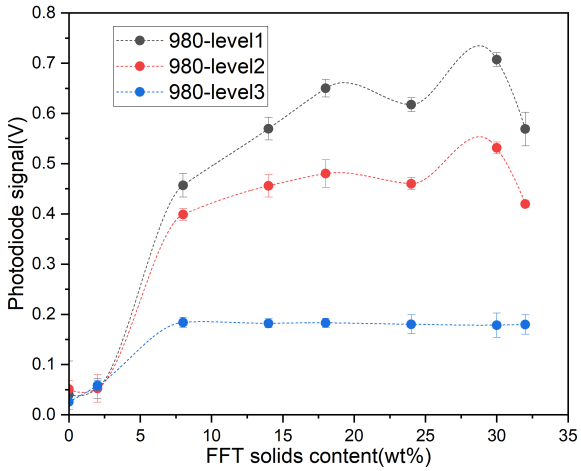

(b)

Figure 4.7: FFT-C sample calibration results measured at 20°backscatter angle using circuit2: (a)1550nm laser diode, (d)980nm laser diode. The results are raw data from calibration tank measurements.

Table 4.6: Growth percentage between two concentrations of FFT-C sample 1550nm calibration results.

Concentration to concentration (wt%)	Level1 growth percentage	Level2 growth percentage
2 to 8	305%	264%
8 to 14	24%	29%
14 to 18	23%	22%
18 to 24	23%	24%
24 to 30	22%	20%

the experimental data, and the R^2 is 0.989.

$$y = -0.000071x^2 + 0.006x + 0.006 \tag{4.1}$$

The calibration function for the 980 nm case (equation 4.2) was determined by fitting a second order polynomial to the experimental data, and the R^2 is 0.919. The 980nm calibration curve did not fit as well with the second order polynomial as the 1550nm.

$$y = -0.0011x^2 + 0.051x + 0.002 \tag{4.2}$$

Where y is the scattering signal data (V) from FFT-C sample of various solids content, x (in wt%).

4.3.3 Comparison of calibration tank and calibration ring results

The calibration tank results could compare with the calibration ring results (Figure 4.3(b)). Since the geometry of the two calibration setups (calibration ring and calibration tank) are different, comparing the data is impossible without correction. During the calibration tank measurements, it was observed that the homogeneity of the sample was good at 8wt%. Therefore, 8wt% data from the two setup measurements were chosen to obtain a normalization factor. The normalization factor of 1550nm LDs is 0.76, and for 980nm is 0.23. The normalized calibration function for the 1550nm case (equation 4.3) was determined by fitting a second order polynomial to the normalized experimental data from the calibration ring, and the R^2 is 0.993.

$$y = -0.00012x^2 + 0.008x + 0.004 \tag{4.3}$$

The normalized calibration function for the 980nm case (equation 4.3) was determined by fitting a second order polynomial to the normalized experimental data from the

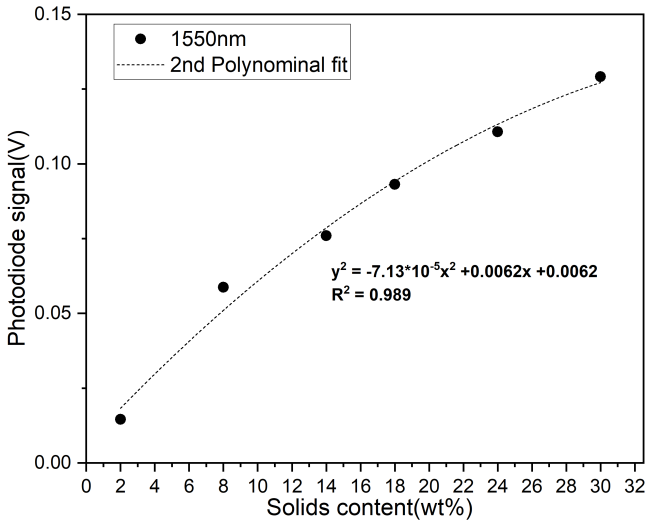

(a)

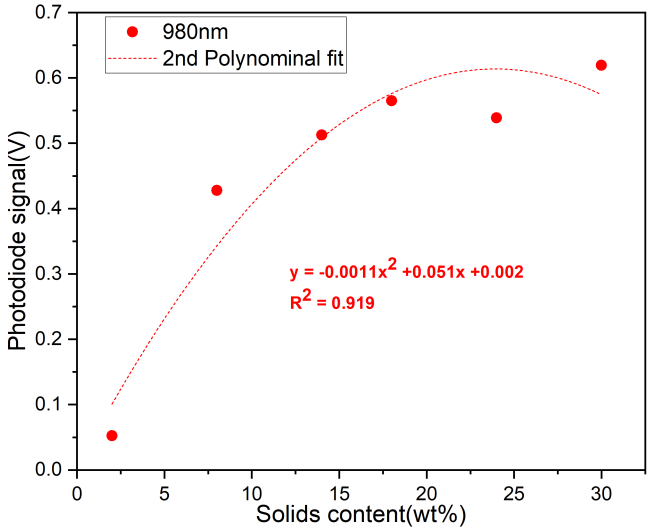

(b)

Figure 4.8: Scattering signal as a function of solids content. (a) The black symbols are data from 1550nm and the black curve is the 2nd order polynomial fit. (b) The red symbols are data from 980nm and the red curve is the 2nd order polynomial fit. The experiments are done by calibration tank.

calibration ring, and the R^2 is 0.883. The 980nm calibration curve did not fit as well with the second order polynomial as the 1550nm.

$$y = -0.000084x^2 + 0.041x + 0.066 \tag{4.4}$$

Where y is the normalized scattering signal data (V) from calibration ring using FFT-A sample of various solids content, x (in wt%).

The comparison of the calibration tank result curves and normalized calibration ring result curves is shown in Figure 4.9. For both 1550nm and 980nm, the calibration curves obtained by the calibration tank and calibration ring setups were consistent. The differences in the calibration curves from the two setups, in addition to measurement errors, may originate from the properties of the sample used. The calibration ring setup used a relatively small amount of the FFT-A sample, while the calibration tank setup used a significantly larger amount of the FFT-C sample. Compared to the relatively simple and reliable operation for calibration ring measurements using a small sample cuvette, the operation for calibration tank measurements is more complicated and error-prone. Therefore, we would recommend a future calibration procedure by conducting a full range of solids content of calibration ring measurements and one specific calibration tank measurement e.g., at solids content around 8wt%. Then the corresponding calibration tank curve can be obtained by normalizing the calibration ring results using the normalization factor. This calibration procedure can reduce the measurement sets using a calibration tank and obtain calibration curves through the easier-to-handle calibration ring measurements.

4.3.4 Application of 1550nm calibration function in the FFT-C sample settling experiment results

The relationship between scattered light signal and sample solids content (under 30wt%) was obtained through the calibration functions. The settling tank and calibration tank geometry are similar except for the volume, and the settling tank and calibration experiments used the same optical sensor system and FFT-C sample.

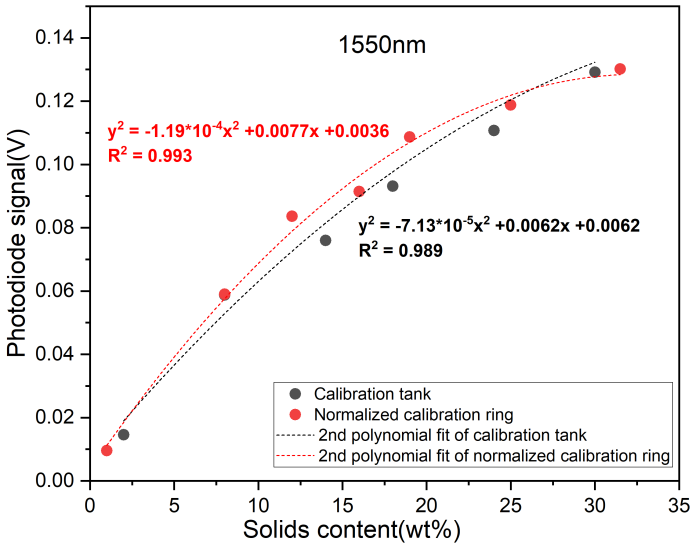

(a)

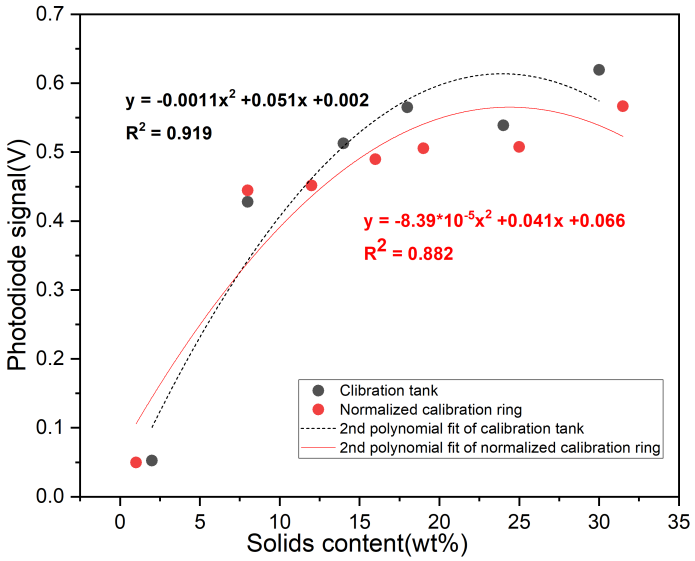

(b)

Figure 4.9: Comparison of calibration tank results curve and calibration ring results curve after normalization: (a) 1550nm, (b) 980nm.

Hence the 1550nm calibration function (equation 4.1) obtained by the calibration tank measurements was used to convert the settling tank data to solids concentration in wt% (Figure 4.10). For 980nm, a much higher scattered light signal in calibration tank measurements was obtained than in settling tank experiments. The reason for the different results is not certain at this time. In addition, the 980nm calibration curve did not fit as well with the 2nd order polynomial equation as 1550nm. The determination of the calibration factor for the 980nm case will need further investigations. This thesis focuses on the 1550nm case due to its high sensitivity to the changes in sample concentration and more negligible bitumen fouling effect (described in chapter 3.3). Hence only the experimental results of 1550nm was analyzed and they will be presented in the following section.

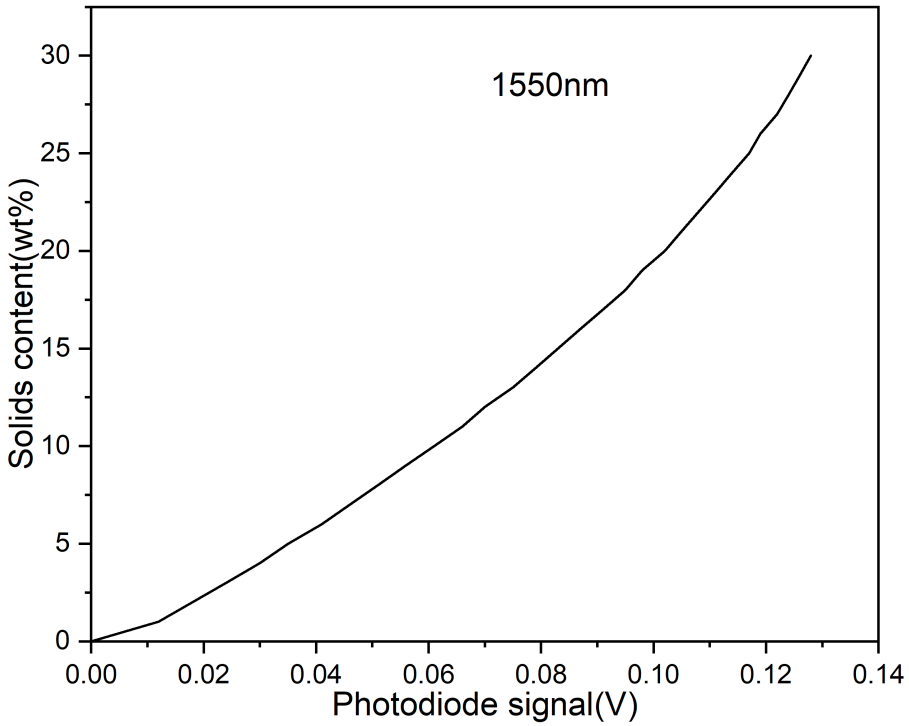

Figure 4.10: Relationship between sample solids content in wt% and scattered light signal in volt for 1550nm. Obtained from 1550nm calibration function4.1.

As discussed in chapter 4.2.5. The correction factors do not work well for sample settling experiment. We assumed that the sample was more or less homogeneous at the beginning. Therefore, the ratio of the initial points of six levels raw data (Figure

3.10(a)) is used to normalize the data respective to level 1 (i.e. level 1 signal is equal to 1) here. The normalization factors are 1, 1.13, 1.43, 1.49, 1.45 and 0.79 for level1 to level6, respectively. Using the calibration curve shown in Figure 4.10, the normalized 1550nm optical sensor data could be converted into solids content in wt%.

For 1550nm-level1 (Figure 4.11(a)), the calculated initial solids content was 14wt%. The scattered light signals gradually increased until day 1.2, and the calculated solids content was 15 wt% on day 1.2. Then the light scattering intensity decreased as the FFT sample settled. The calculated solids content was 8wt% and 6wt% on day 2 and 3, respectively. After day 6, large particles settled and fine particles remained at the level1 position, and the calculated solids content was 4.5wt%.

For level2 data, the initial solids content calculated was 14wt% (Figure 4.11(b)). The scattered light signal continued to increase until day 10, likely because of the settling of solids from the upper level. On day 10, the calculated concentration was 17wt%, then the signal began to decrease. The calculated concentration was 15wt% and 11wt% on day 15 and 25, respectively.

For level3 data, the initial calculated solids content was 14wt%. The scattered light signals rapidly increased in the first 2 days, and the signal was approximately constant from day 2 to day 25 with a solids content calculated to be 16 wt%. The signal began to drop on day 25. When the water-solid interface reached the level3 1550nm LD position, the solids content at level3 decreased to around 6wt%. The signal rapidly dropped from day 35 to day 43 and then flattened out. The solids content was calculated to be 2wt% at day50.

The calculated initial solids content of level4 to level6 was all around 14wt%. The scattered light for the three bottom levels showed rapid increases of a couple of wt% in the first few days. The level 4 data followed with a relatively gradual decrease, while the level 5 and 6 data followed with gradual increases.

In summary, the 1550nm calibration curve obtained from calibration tank data can be used to convert the 1550nm optical sensor data of the sample settling experiment

to solids concentration in wt%.

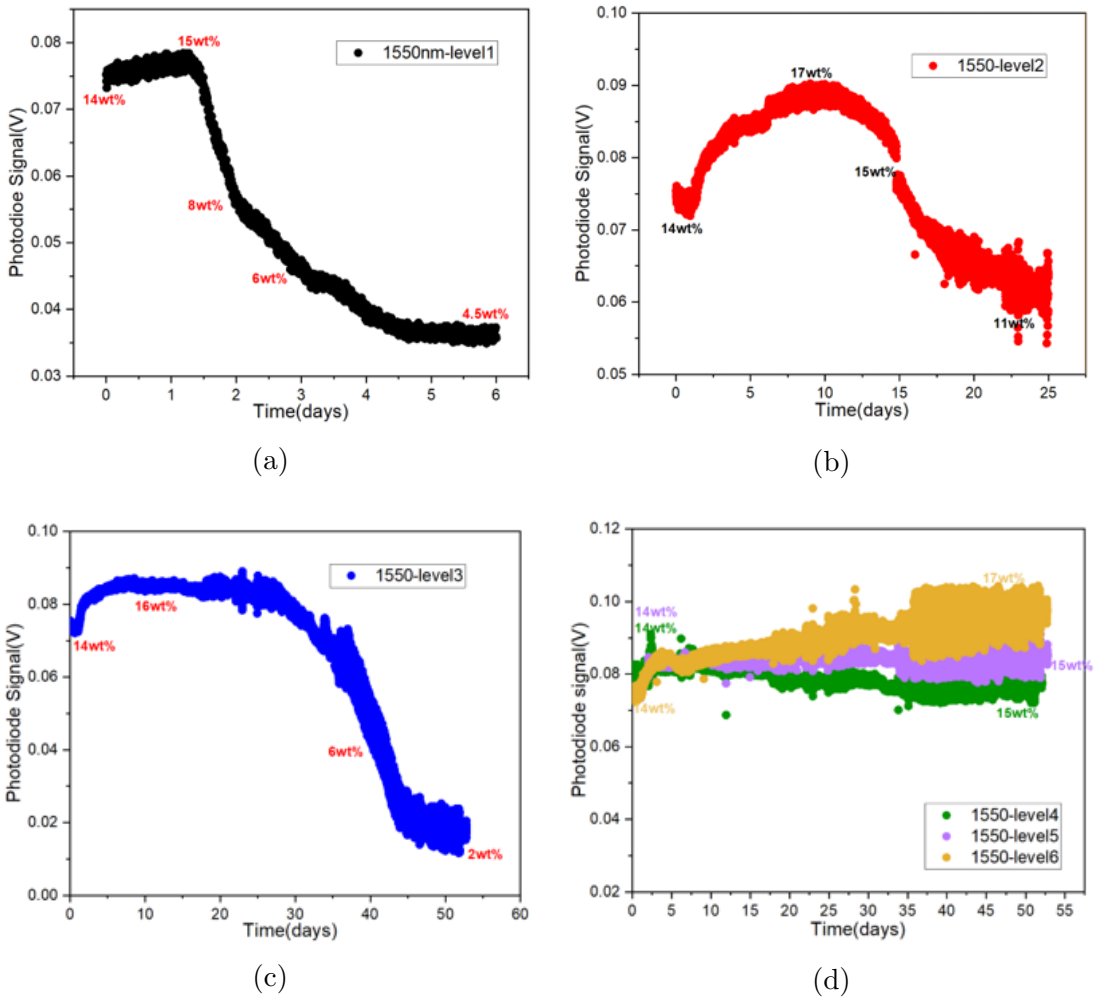

Figure 4.11: Temporal evolution of solids content in FFT-C sample settling experiment. (a)1550nm-level1 (b)1550nm-level2 (c)1550nm-level3 (d)1550nm level4 to level6

4.4 Sensitivity of optical measurements

It is essential to know the sensitivity of the optical sensor system. As discussed, the 1550nm wavelength demonstrated the most consistent increase in the light scattering intensity with the variation of the solids content. Figure 4.10(a) shows that solids content in wt% as a function of PD signal in volt can be obtained from the calibration equation 4.1. The sensitivity was determined by the slope of this curve. The corre-

sponding PD signal changes per 1wt% in different solids content ranges are shown in Table 4.7.

Table 4.7: The corresponding PD signal change per 1wt% in different solids content range.

Solids content range	PD signal change per 1wt%
1-6wt%	6mV
7-12wt%	5mV
13-20wt%	4mV
21-26wt%	3mV
27-30wt%	2mV

Table 4.8: 1550nm wavelength sensitivity in different solids content range.

Solids content range	Sensitivity (approximately)
1-6wt%	1wt%
7-12wt%	1wt%
13-20wt%	1.25wt%
21-26wt%	2wt%
27-30wt%	2.5wt%

The DAQ equipment can easily distinguish a 5mV change in PD signal even in the presence of noise. The noise level was under 5mV when the circuit was stable. The sensitivity of the scattering intensity projected to the solids content is about 1wt% to 2.5wt% (shown in Table 4.8), indicating that the 1550nm wavelength is able to detect the change of 1wt% to 2.5wt% in the solids content. The sensitivity is expected to be lower after install the optical sensor in the real tailings ponds, due to the complex solids content distribution. The FFT materials in tailings ponds are inhomogeneous and the uncertainty for the real world measurements can be significantly higher. Further studies are needed to better understand the issues.

4.5 Correlation of gamma ray and optical 1550nm measurements

The gamma-ray method based on the gamma-ray transmission provides an absolute measurement of solids content at different depths. A low radiation intensity source and a Cadmium Telluride detector were used to measure the solids content in tailings samples. The radiation source used in the experiment was a 1 Ci 133Ba.[16] All the gamma-ray technique experiments were conducted by group member Bo Yu.

Experiments were conducted in a settling tank (see chapter3) with kaolin and FFT samples to investigate the correlation between the optical scattering and gamma-ray transmission techniques. The temporal evolution for optical sensor and gamma-ray results for 15wt% Kaolin [41] and 18.5 wt%FFT sample are shown in Figure 4.12 and Figure 4.13, respectively.

For the Kaolin study, the tank was filled with 15wt% 600nm Kaolin sample initially. The gamma-ray source and detector were located around 6.5 cm below the water surface, and the 1550nm LD and PD were located 5.3 cm and 6.5 cm below the water surface, respectively. As the solids content increased, the light scattering intensity would increase and gamma-ray transmission would decrease. As shown in Figure 4.12, the light scattering intensity reduced drastically almost simultaneously when the gamma-ray transmittance increased significantly, indicating that the two techniques agreed qualitatively well with each other.

For the FFT study, the tank was filled with 18.5wt% FFT-C sample initially. For level2, the LD and PD were located 5.3 cm and 6.5 cm below the water surface, respectively. The gamma-ray source and detector should locate at 6.5cm same as the photodiode, but they were located around 5.5 cm below the water surface by mistake. Since the gamma-ray source and detector are on top of the PD, there was a lag in the decrease of light scattering intensity compared to the increase of gamma-ray transmission signals (Figure 4.13(a)). The noise in 1550nm optical data after 35 days

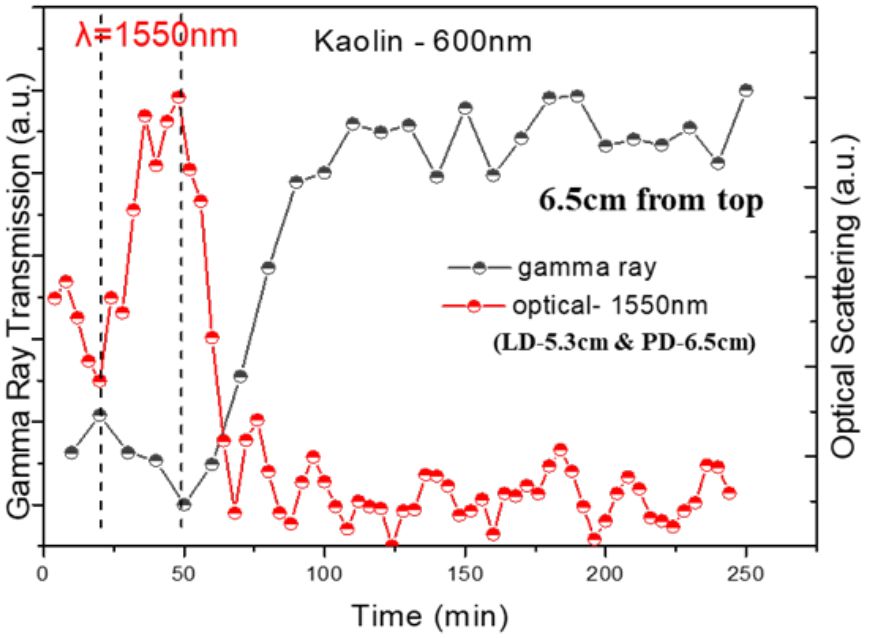

Figure 4.12: Optical scattering (1550 nm) signal versus gamma-ray signal at a depth 6.5 cm (level2) from the initial water surface for a 15wt% Kaolin sample.[41]

may be due to the unstable circuit or fine particles remaining above the water-solid interface. For Level 3, the gamma-ray source and detector were located around 11 cm below the water surface, and the LD and PD were located 10 cm and 11 cm below the water surface, respectively. Thus the gamma-ray source, detector and photodiode were in the same position. It was observed that the light scattering signal was reduced simultaneously when the gamma-ray transmission signal increased (Figure 4.13(b)). Similar to the Kaolin sample, for the FFT study, both the gamma-ray technique and optical sensor agreed qualitatively well with each other.

The calibration experiment was conducted by Bo Yu, a colleague in our lab, and the gamma-ray transmission signal could be calibrated by the linear curve equation shown in Figure 4.14[41]. The gamma-ray calibration curve was obtained by measuring different wt% of the FFT-B sample for 10 minutes (repeated 5 times) in the calibration tank with the same tube and distance as the settling tank (6.5cm below the water surface). The conversion of the gamma-ray signal to solids content in wt% can also be determined based on model calculations using simulation models such as

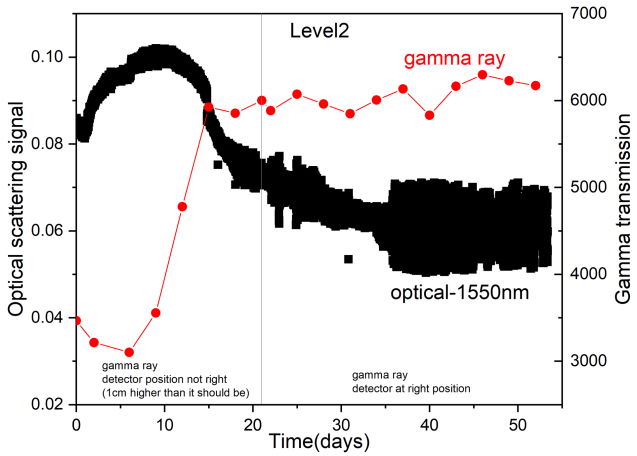

(a)

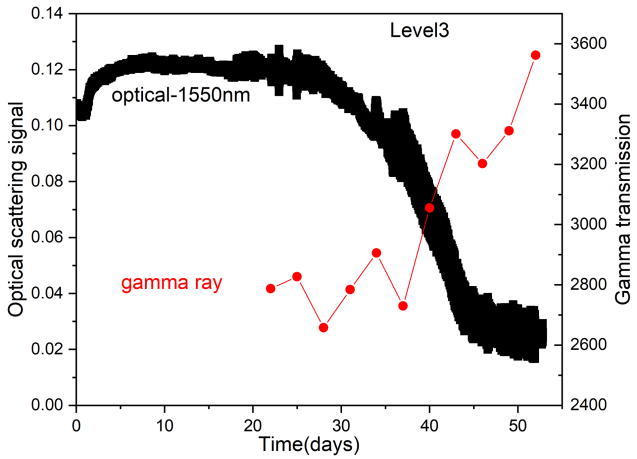

(b)

Figure 4.13: Optical scattering (1550nm) signal versus gamma-ray transmission signal at 2 different depths in the settling tank: (a) level2 (6.5cm below the water surface) and (b) level3 (11cm below the water surface). The settling tank was initially filled with 18.5 wt% FFT-C sample.

GEANT4. This approach was demonstrated by our group.[16]

To carry out a more detailed comparison, the optical scattering signal and gamma-ray transmittance signal were converted into solids content in wt% using the optical calibration equation (equation 4.1) and the gamma-ray calibration curve (Figure 4.14). The results are shown in Figure 4.15. The optical calibration function was obtained by the FFT-C sample, and the gamma-ray calibration function was obtained by the FFT-B sample. In general, the results from two techniques using different samples can be correlated.

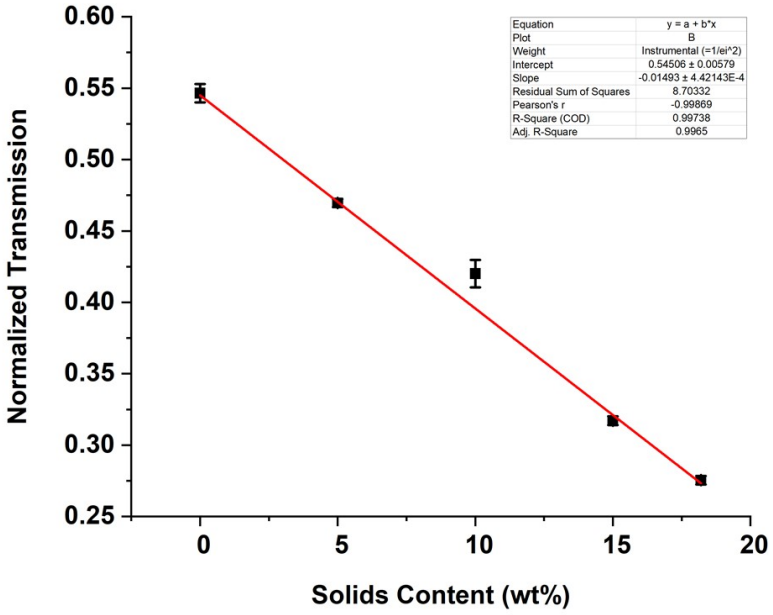

Figure 4.14: Gamma ray calibration curve obtained by measuring different wt% of FFT-B for 10 minutes (* 5 times) in calibration tank with the same tube and distance as the settling tank.[41]

The level2 results are shown in Figure 4.15(a). The trends of the two data curves agreed well in the first 5 days. The starting point of the concentration decrease of the optical curve was at day10, which lagged behind the gamma-ray curve (around day6). At day25, the gamma-ray data dropped to around 0wt% solids content while the optical data decreased to around 10 wt%. The gamma-ray sensor was 1cm above the photodiode and closer to the water surface. Therefore, the gamma-ray sensor would detect the drop in the concentration earlier than the photodiode. The differences between the two sensors for long settling time are not understood and will need further investigations.

The level3 results are shown in Figure 4.15(b). For level3, the gamma-ray source and detector were located 11cm below the water surface, and the 1550nm LD was located 10cm below the water surface. After day30, the water-solid interface reached 10 cm below the water surface. Both sensors showed decreases in solids content. The optical

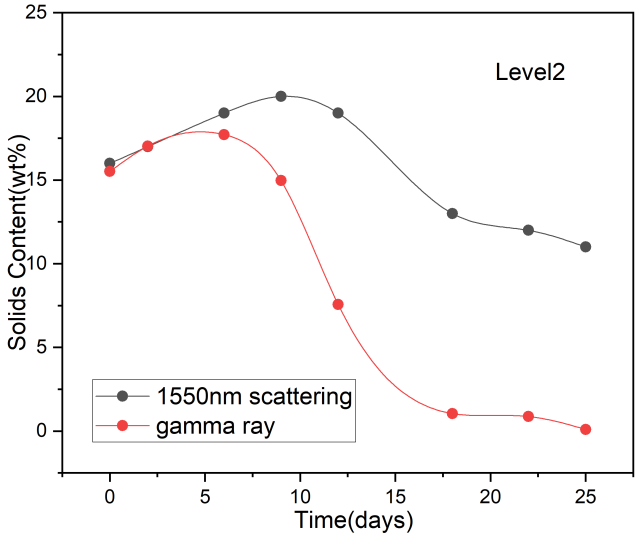

(a)

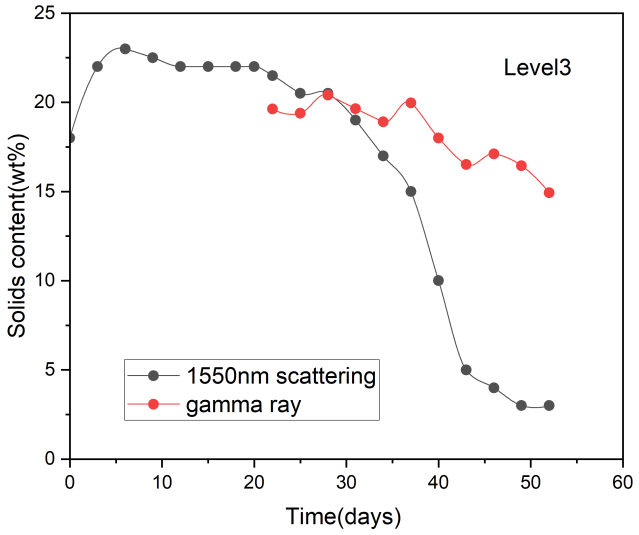

(b)

Figure 4.15: Temporal evolution of solids content varies for FFT-C sample at: (a)level2 (6.5cm below the water surface), (b)level3 (11cm below the water surface). The black symbols represent results calculated by the 1550nm calibration function and red symbol represent results calculated by the gamma-ray calibration function.

sensor showed a more rapid decrease of solids content than the gamma-ray sensor, which may be due to the bitumen fouling effect on the window of the optical sensor.

4.6 Summary

The 20° backscatter angle was chosen for the sensor design because it gives an optimal compromise between high light scattering signals and avoids specular reflection. Correction factors are needed to correct the raw data because of the difference in LD output (due to the limitations of the circuit design) and the different sensitivity of each PD (due to the inherent characteristic). Based on calibration ring and calibration tank results, calibration function for 1550nm was created, which can convert original data of settling tank experiments in volt into solids content in wt%. The 1550nm wavelength is highly sensitive and can detect 1wt% to 2.5wt% change in different solids content ranges. The results of the optical and gamma-ray techniques in general are consistent. The gamma-ray technique can be used for absolute calibration of the optical sensor system.

Chapter 5

Description of whole project

This project aims to design a relatively low-cost real-time in situ subsurface solids content analyzer suitable for large-scale implementation in oil sands tailings ponds and dewatering facilities. As discussed in the previous chapters, a relatively low-cost optical sensor system based on the light scattering technique was developed to detect the solids content and monitor the settling process. Optical window fouling, calibration, installation, power, and data communication are the major problems. This chapter will focus on how to deal with these major problems and the complete design of this project.

5.1 Optical window fouling

Bitumen fouling on the optical window is a challenge for proper measurement of the optical sensor system. Therefore, methods need to be developed to mitigate the effects of bitumen fouling. The following two different approaches can be considered:

Wavelength optimization

As discussed in chapter 3, wavelength optimization experiments were conducted by Dr. Tulika Srivastava. Cold solvent wash is a method to purify solids from a solvent at room temperature. By cold washing, the bitumen in FFT samples was removed, and solids remained. IPA/toluene mixture solvent was used for cold washing FFT samples to remove bitumen. The results of transmission experiments conducted with

FFT-A and the cold-washed FFT-A sample as well as water are shown in Figure 5.1. The absorption spectra of raw and cold washed FFT-A sample Figure 5.1(a)) indicate that residual bitumen in the FFT-A sample caused the reduction of light signals in the visible range while negligible light absorption by bitumen in the NIR range. In the NIR wavelength spectra (Figure 5.1(a)), there are two strong absorption bands at 1200nm and 1400nm. Due to the strong absorption features, it is difficult to detect minute solids content in the sample. Therefore 980nm and 1550nm wavelength LDs were chosen as the light sources. Especially 1550nm wavelength, the light scattering signal increases linearly with the increase of solids content, caused by the high absorption by water (Figure 5.2(b)) and the scattered light from solids particles. In summary, the NIR wavelengths, especially 1550nm, are the optimum choice due to their less bitumen absorption and high absorption in water.[31]

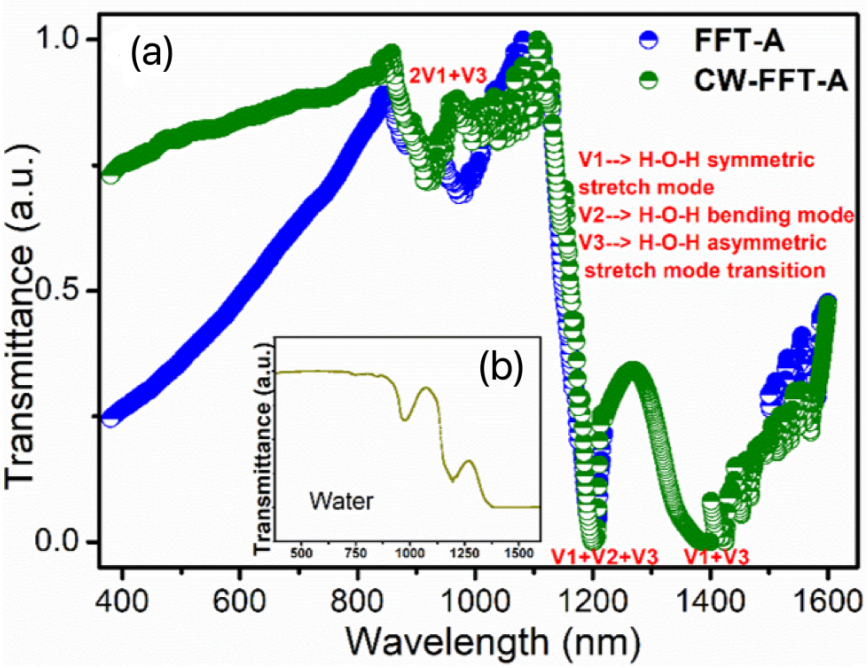

Figure 5.1: Effects of bitumen fouling on the measurement: (a) absorption spectra of raw and cold washed FFT-A, (b) (inset figure) absorption spectra of water).[31]

Fouling resistant window materials

Using bitumen fouling resistant optical window materials is another method for mitigating the effects of bitumen fouling. Antifouling materials for optical windows, specifically those made of oleophobic which can repel bitumen, and hydrophilic which attracts water, can be an option for reducing the bitumen fouling effect. Plexiglass, glass and sapphire windows were tested by Xiaoxun Liu and Dr. Tulika Srivastava, colleagues in the lab. Glass and sapphire windows exhibited hydrophilic and oleophobic behavior and had little or no degradation after a certain time period submerged in the FFT-B sample. Transmittance measurements for 1550nm laser light on the three materials were conducted. Clean window and window immersed in the FFT-B sample for 3 months were tested. As shown in Figure 5.2, glass and sapphire windows showed less bitumen fouling effects (as indicated by less black spots) than plexiglass window after being submerged in the FFT-B sample for 3 months. In summary, glass and sapphire are both suitable for the choice of bitumen fouling resistant optical window materials. However, glass is more inexpensive and accessible.[41]

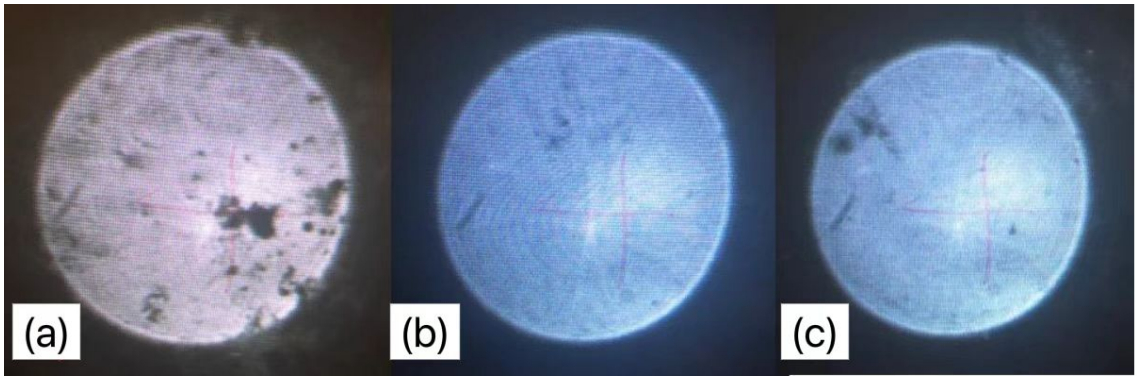

Figure 5.2: 1550nm photos of: (a) plexiglass, (b) glass, (c) sapphire. All the three materials were immersed in the FFT-B sample for 3 months.[41]

5.2 Calibration

In the chapter4, the calibration method of the optical system itself was discussed. However, after installing the subsurface solids contents analyzer into a tailing pond,

the performance of LD and PD can not be monitored continuously for calibration. Hence a real-time calibration method is needed for the optical system. The gamma-ray technique based on gamma-ray transmission is identified as a promising and safe method for measuring solids content in tailings ponds, and it can provide absolute calibration of the optical sensor system at different depths. The concept of the gamma-ray method is shown in Figure 5.3. The gamma-ray transmission measurements use a low radiation intensity Ba-133 (1μCi) source and a Cadmium Telluride detector. The intensity ratio of two peaks around 31 and 81 keV from a 1 Ci 133Ba source is used to measure the solids content. The 31 keV peak is sensitive to changes in the FFT's solids content, whereas the 81 keV peak is insensitive and serves as a source strength reference. The conversion of gamma-ray signals to solids content in wt% can be determined from simulations using GEANT4.[16] The gamma-ray signal is also not affected by the presence of bitumen fouling on the windows. A compact, portable, and low-cost detection system was developed for the solids content analyzer. Such a low-activity source is much weaker than that traditionally used in density measurement applications and is well below the regulatory licensing limit for radioisotope sources. This makes measurement instruments based on such sources safe to handle and easy to deploy in real field applications.[16] Good accuracy of 3 wt% was achieved, similar to commercially available options, but at a fraction of the cost. The custom-made gamma-ray system can detect a full range of solids content (0-100wt%). The effect of temperature on this gamma-ray detector gain was also investigated, and an effective gain compensation method was built.[41]

5.3 Preliminary fiber optic system

In general, the tailing ponds are very deep. Hence the LDs and PDs require long cables to connect to the circuits, making sensor installation difficult. The long cable is costly and will increase the cost of the system. It is possible that LDs and PDs may not perform well during the testing process and require replacement. Due to the

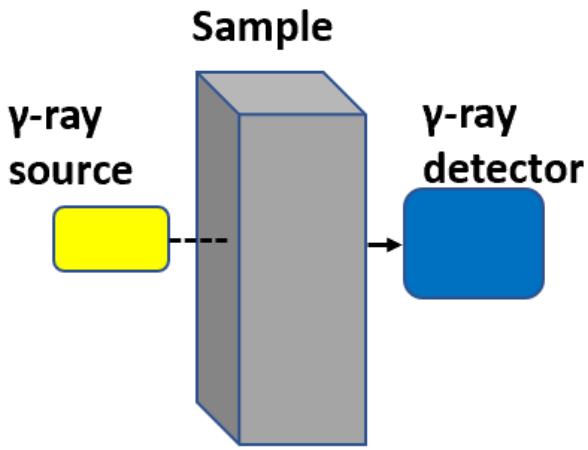

Figure 5.3: Simplistic diagram of the concept of the gamma-ray method.

difficulties in LD and PD installation and replacement during the monitor process in the deep tailing ponds, it may be desired to send and receive laser light and backscattering signal without submerging the LDs and PDs under the tailing ponds surface. Optical fiber is an option for sending and receiving light signals. Initial testing was conducted to see the difference in power received by photodiode with and without optical fiber. In the experiment, 658nm LD with 7mW power was used as a light source and a Teflon slice as a sample to completely reflect the light. The setup is shown in Figure 5.4(a). The comparison between the signal received through optical fiber and the signal directly captured by PD is shown in Figure 5.4(b). The small core area of an optical fiber limited the scattering light that could be captured. The results demonstrated that the optical fiber is suitable to send and receive light scattering signals when a 10-time amplifier (circuit shown in Figure 5.4(c)) was used. Therefore, optical fiber can be a good option for future improvement of the optical sensor.

5.4 Power and Communication

Tailings ponds are often located in remote areas with harsh weather conditions. To power the analyzer system and enable remote data transmission, an initial concept

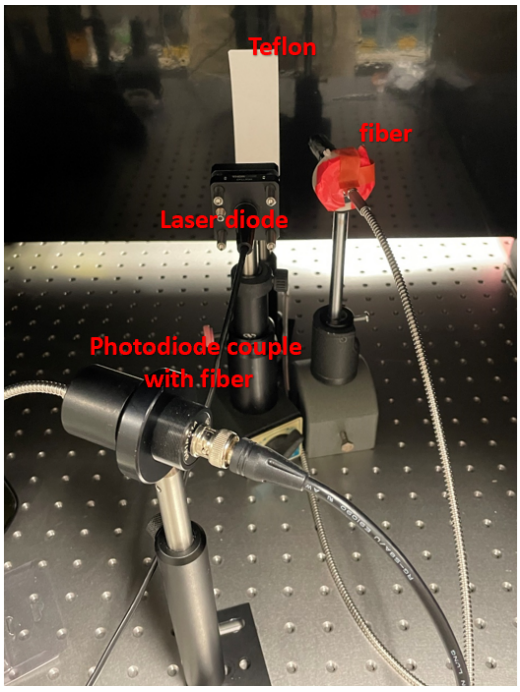

(a)

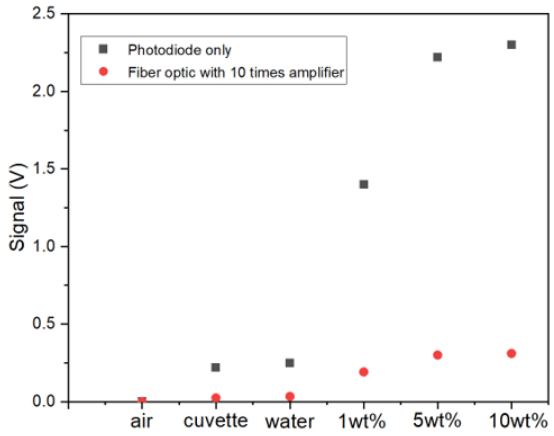

(b)

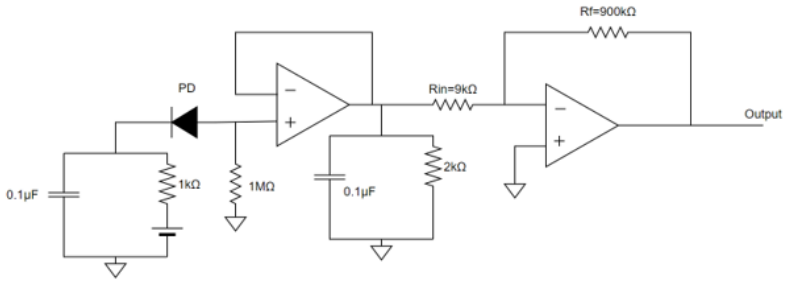

(c)

Figure 5.4: Optical fiber initial test with 7mW 658nm LD and Teflon slice: (a) Experimental setup, (b) results of comparison between the signal received through optical fiber and the signal directly captured by PD, (c) 10 times amplifier circuit

of power and communication units was developed by 4 senior electrical engineering undergraduate students (members include Allen Feng, Junlong Pan, Shyam Patel and Dillon Sweeney) as part of their final year capstone project. The system block diagram shows the connection of the entire system, and its various components (Figure 5.5) [42].

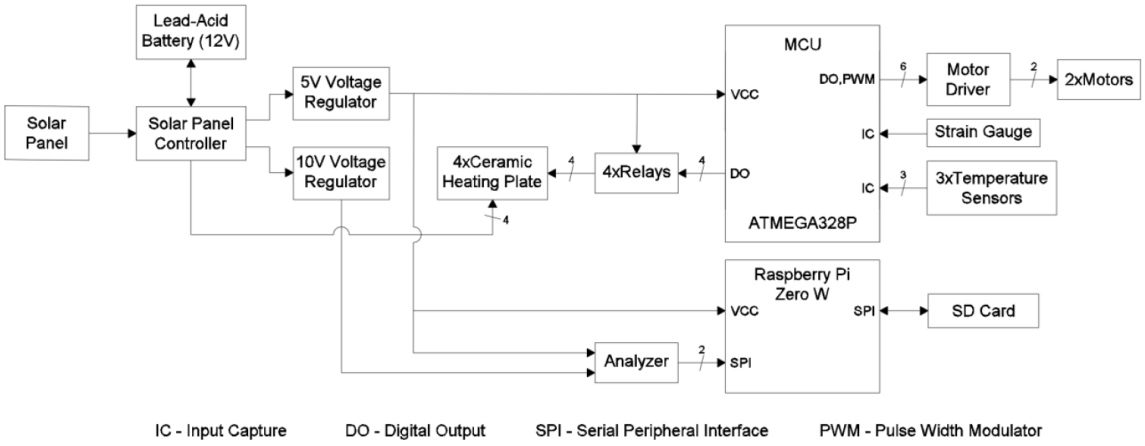

Figure 5.5: System block diagram for power and communications unit. This shows the connection of the entire system and its various components.[42]

The power unit consists of three main subsystems. The first is the battery-solar panel subsystem, which uses a 12V, 60Ah Sealed-Lead-Acid battery to power the entire system. An 18V, 150W solar panel is used to prevent the battery from running out of power, and a solar charge controller is used to prevent the battery from overcharging. The 12V of the battery is stepped down to 10V and 5V using two buck converter voltage regulators to satisfy the requirements of the solids content analyzer system. The second is the temperature control system, which is capable of keeping the components under the operating temperature range in winter. The temperature control subsystem consists of a temperature sensor and four ceramic heating plates, which are tested at multiple temperatures between -20to 22successfully. The third is the solar panel maintenance subsystem, which is critical in keeping the solar panel operational in winter by cleaning up the snow, which may prevent the sunlight from reaching the solar panel. A strain gauge is used as a basic snow sensor. If the pressure on the

gauge exceeds a threshold, two wiper-equipped motors will be activated to clean up the snow. A motor driver controls the speed and direction of the motors.

The communication unit contains two subsystems. The first is the data acquisition and transmission unit, which can receive data from the solids content analyzer system and send them to a remote website wirelessly. The data from the analyzer will be transmitted to a 16-bit analog to digital converter and recorded in the Raspberry Pi Zero W in real time, then wirelessly transmits the collected data in a single CSV file to an online website through Wi-Fi once per hour. The second subsystem is an online website written in HTML and PHP coding languages and can be accessed by clients. The power and communication units can operate for the foreseeable weather conditions and function for six months at a time before any maintenance activity needs to be performed.

5.5 Full design of the real-time in-situ subsurface solids contents analyzer

This project has built a real-time in-situ subsurface solids content analyzer based on light scattering and gamma-ray technologies. With a proper calibration procedure, the optical sensor system based on light scattering can measure relative changes in solids content at different depths, whereas the gamma-ray sensor based on gamma-ray transmission can provide absolute measurements of solids content at different depths for optical detector calibration in real time. The power and communication unit can power the entire system, keep the components within the operating temperature and transmit data remotely. This real-time in-situ subsurface solids content analyzer is relatively low cost and well-suited for large-scale implementation in oil sands tailings ponds and dewatering facilities. It is assumed that the solids content analyzer must operate continuously for a minimum of six months before maintenance is required. Figure 5.6 shows the concept of the overall analyzer system. The optical and gamma-ray systems are submerged under the tailing ponds within an insertion tube, and the

power and communication system is on a floating platform above the tailing ponds' surface.

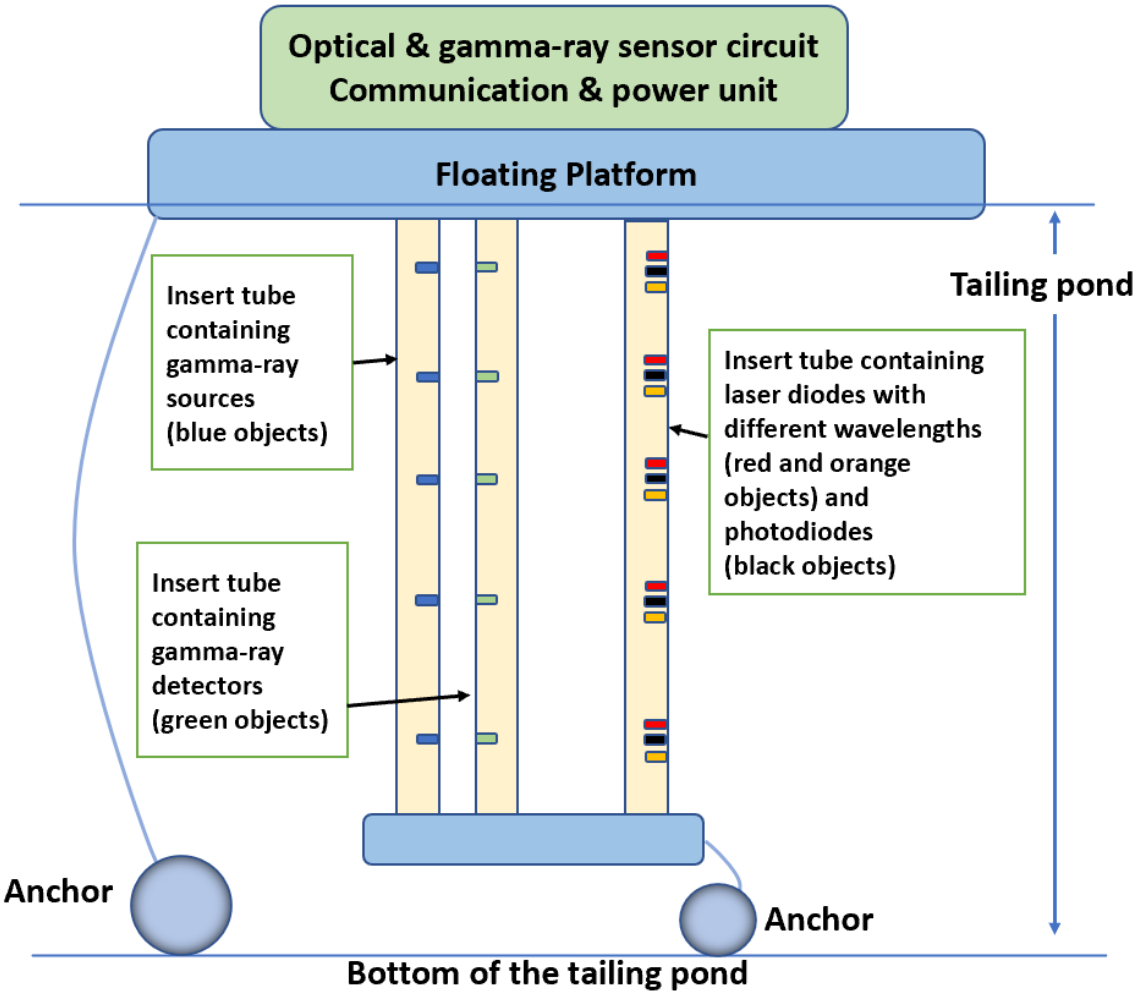

Figure 5.6: Cartoon illustrating the overall concept for the subsurface solids content analyzer. The main components are (i) the gamma-ray system with gamma ray sources (blue objects in the insert tube) and gamma ray detectors (green objects in the insert tube); (ii) the optical system with laser diodes with different wavelengths (red and orange objects in the insert tube) and photodiodes (black objects in the insert tube); (iii) optical and gamma ray circuits above the tailing pond surface; and (iiii) the communication and power unit above the tailing pond surface.

Chapter 6

Conclusion and Future Directions

6.1 Summary

The main goal of this thesis was to develop an in-situ subsurface and low-cost solids content analyzer based on the multi-wavelength light scattering technique (405nm, 658nm, 980nm and 1550nm) to monitor the settling process and solids concentration of FFT in oil sands tailing ponds at different depths.

In chapter 2, three setups: (a) ring setup for angle optimization and calibration, (b) settling tank for lab-scale sample settling experiments, and (c) calibration tank for calibration experiments, were discussed in detail. An optical sensor system includes an LD system with different wavelengths as the light source and a PD system as the light detection instrument was developed.

Chapter 3 focused on lab-scale settling tank experiments using the optical light scattering sensor. 15wt% 600nm Kaolin sample and FFT samples (21.7wt% and 18.5wt% in concentration) were tested using both visible wavelengths (405nm and 658nm) and NIR wavelengths (980nm and 1550nm). It was observed in both Kaolin and FFT measurements that the intensity of scattered light tends to decrease corresponded to the decrease in solids concentration. NIR wavelengths, especially 1550nm, showed better results due to their high sensitivity to the change in solids content and less bitumen fouling effecting.

In chapter 4, 20° backscattering angle was determined to be the optimum observation

angle for the optical sensor. Calibration experiments were conducted by both calibration ring and calibration tank to determine the functions needed to convert scattering light signals to solids content in wt%. To correct for the effect of difference in LD output power and different sensitivity of PD, LD and PD correction factors were obtained and were used to correct for results from calibration tank and settling tank experiments. The 1550nm wavelength is highly sensitive and able to detect 1wt% to 2.5wt% solids content change in different concentration ranges. Finally, the optical sensor results of FFT-C sample settling tank experiments were compared with the gamma-ray sensor results, and the results of the two techniques agree well with each other.

In chapter 5, two methods, wavelength optimization and choosing fouling resistant window materials, to mitigate the effects of optical window bitumen fouling were discussed. Then the gamma-ray sensor that provides real-time absolute calibration for the optical sensor system was introduced. A possibility of transmitting the light signal in the optical sensor system with fiber optics was proposed. Then a concept of power and communication system was discussed. Finally, the entire concept of the real-time in-situ subsurface solids content analyzer was discussed. The entire design of this analyzer includes an optical sensor system, a gamma-ray sensor system, and a power and communication unit. This real-time in-situ subsurface solids content analyzer is relatively low cost and well-suited for large-scale implementation in oil sands tailings ponds and dewatering facilities. The analyzer is expected to operate continuously for a minimum of six months before maintenance is required and can work in harsh weather conditions.

6.2 Future Considerations

In the future, the LD system can be improved to ensure that each LD has the same output by driving the LDs with a one-to-one LD driver. Because of the large potential temperature changes in the field, the temperature effects on LD and PD system

should be determined. Standard calibration and testing procedures for optical sensor system should be developed, including LD output calibration, PD sensitivity calibration, and insertion tube transmission calibration. Due to the difficulties in LD and PD installation and change during the monitor process in the deep tailings ponds, a signal transmission module based on fibre optic couplers should be investigated for improving the sensor's optical sub-system. Printed circuit boards should be built to improve the robustness and compactness of the sensor electronic sub-system. Optical materials and coatings should be further developed to mitigate bitumen fouling effects. Communication and power modules should be further developed for the field prototype. Then the next step for further development of the whole design of this solids content analyzer will be to test it at a large pilot scale. An optical and gamma-ray hybrid prototype was built, and we plan for field implementation and a long-term test. After further evaluation and optimization, it could be implemented in real tailing ponds.

Bibliography

[1] G. of Alberta, *Oil sands facts and statistics*, https://www.alberta.ca/oil-sands-facts-and-statistics.aspx, Accessed2019.

[2] B. P. Company, *Bp statistical review of world energy*, https://www.bp.com/content/dam/bp/business-sites/en/global/corporate/pdfs/energy-economics/statistical-review/bp-stats-review-2018-full-report.pdf, AccessedJune 2018.

[3] A. O. S. Technology and R. Authority, *Aostra: A 15 year portfolio of achievement*, https://archive.org/details/aostra15yearport00albe, Accessed1990.

[4] A. E. Regulator, *Water use performance*, https://www.aer.ca/protecting-what-matters/holding-industry-accountable/industry-performance/water-use-performance.html, Accessed2019.

[5] J. M.N., *Oilsands tailing ponds are a nasty challenge that cant be ignored. pembina institute.* https://www.pembina.org/op-ed/oilsands-tailing-ponds-are-nastychallenge-cant-be-ignored, Accessed2018.

[6] M. Gupta, T. Ho, T. Srivastava, A. Junaid, A. Sedgwick, and Y. Y. Tsui, "A real-time light-scattering technique for tailings solids measurement)," *Journal of Environmental Quality*, 2021.

[7] B. E. Inc., *Oil Sands Tailings Technology Review*. Oil Sands Research, Information Network, University of Alberta, School of Energy, and the Environment, Edmonton, Alberta, 2010.

[8] E. I. Valenzuela, A. C. García-Figueroa, L. E. Amábilis-Sosa, F. E. Molina-Freaner, and A. M. Pat-Espadas, "Stabilization of potentially toxic elements contained in mine waste: A microbiological approach for the environmental management of mine tailings," *Journal of Environmental Management*, vol. 270, p. 110 873, 2020.

[9] S. C. Motta Cabrera, J. L. Bryan, and A. Kantzas, "Estimation of Bitumen and Solids Content in Fine Tailings Using Low-Field NMR Technique," *Journal of Canadian Petroleum Technology*, vol. 49, no. 07, pp. 8–19, Jul. 2010.

[10] O. S. MAGAZINE, *Tailings ponds 101*, https://www.oilsandsmagazine.com/technical/mining/tailings-ponds, Accessed2021.

[11] A. R. Sorta, "Centrifugal modelling of oil sands tailings consolidation. (doctor of philosophy dissertation, university of alberta, department of civil and environmental engineering. canada)," 2015.

[12] T. E. Baxter, *Total solids by gravimetric determination*, https://www.alberta.ca/oil-sands-facts-and-statistics.aspx, Accessed2017.

[13] J. T. Bulmer and J Starr, "Syncrude analytical methods for oil sand and bitumen processing," 1979.

[14] A. Li and Z. Xu, "Determination of clay content in canadian oil sands using x-ray florescence spectroscopy for diagnosis of ore processability," *The Canadian Journal of Chemical Engineering*, 2019.

[15] J. Costa, J. Borges, and L. Pires, "Soil bulk density evaluated by gamma-ray attenuation: Analysis of system geometry," *Soil and Tillage Research*, vol. 129, pp. 23–31, 2013.

[16] Y. Bo, W. Wei, S. T. K., S. Tulika, S. Andrea, J. Abu, G. Manisha, F. Robert, and T. Y. Y., "X-ray radiation monitor for measuring solids content in fluid fine tailings," *Journal of Environmental Quality*, vol. 50, no. 4, pp. 945–954, 2021.

[17] M. Luycx and C. Torres-Verdín, "Physics, applications, and limitations of borehole neutron-gamma density measurements.," *Geophysics*, pp. 39–56, 2019.

[18] B. D. Clercq, P. A. Lant, and P. A. Vanrolleghem, "Focused beam reflectance technique for in situ particle sizing in wastewater treatment settling tanks," *Journal of Chemical Technology and Biotechnology*, 2004.

[19] D. Acevedo, W.-L. Wu, X. Yang, N. Pavurala, A. Mohammad, and T. F. O'Connor, "Evaluation of focused beam reflectance measurement (FBRM) for monitoring and predicting the crystal size of carbamazepine in crystallization processes," *The Royal Society of Chemistry*, 2021.

[20] M. Li, S. L. Barbour, and B. C. Si, "Measuring Solid Percentage of Oil Sands Mature Fine Tailings Using the Dual Probe Heat Pulse Method," *Journal of Environmental Quality*, pp. 293–298, 2015.

[21] Berne, B. J., and R. Pecora, *Dynamic light scattering: with applications to chemistry, biology, and physics.* Courier Corporation, 2000.

[22] H. Mubashir, Z. Songsheng, Y. Ping, A. Yukun, L. Zhiyang, A. Irshad, L. Bin, S. Han, and H. Nongyue, "Rapid detection system for hepatitis b surface antigen (hbsag) based on immunomagnetic separation, multi-angle dynamic light scattering and support vector machine," *IEEE Access*, vol. 8, pp. 107 373–107 386, 2020.

[23] A. A. Nastulyavichus, S. I. Kudryashov, E. R. Tolordava, L. F. Khaertdinova, Y. K. Yushina, T. N. Borodina, S. A. Gonchukov, and A. A. Ionin, "Dynamic light scattering detection of silver nanoparticles, food pathogen bacteria and their bactericidal interactions," *Laser Physics Letters*, vol. 18, no. 8, p. 086 002, 2021.

[24] S. J., M. S.A., and P. T.R, "Dynamic light scattering: A practical guide and applications in biomedical sciences," *Biophys Rev 8*, 409–427, 2016.

[25] C. M. Maguire, M. Rösslein, P. Wick, and A. Prina-Mello, "Characterisation of particles in solution – a perspective on light scattering and comparative technologies," *Science and Technology of Advanced Materials*, vol. 19, no. 1, pp. 732–745, 2018.

[26] E. Hecht, *Optics 4th Edition*. CA: Pearson Education, 2002.

[27] T. Ho, "Development of compact fluroescent spectrometers and field deployable opticle solids content monitoring devices. (master dissertation, university of alberta canada)," 2015.

[28] B. P., *Chapter 19 - Colloid and Surface Chemistry. In Biermann's Handbook of Pulp and Paper (Third Edition)*. 2018.

[29] R. P. Donovan, *Chapter 4- Light Scattering Theory. In Particle Control for Semiconductor Manufacturing*. CRC Press, 2018.

[30] M. R. J., K. K. L., B. R. D., and M. M. D., "Nature and fate of oil sands fine tailings," in *Suspensions: Fundamentals and Applications in the Petroleum Industry*, ch. 14, pp. 677–723.

[31] T. Srivastava, J. Zhang, B. Yu, A. Junaid, A. Sedgwick, R. Fedosejevs, G. Manisha, and Y. Tsui, "A real time in situ light-scattering technique for tailings solids content measurement: Nir versus visible wavelengths," 2021.

[32] Newport, *Laser diode technology.* https://www.newport.com/t/laser-diode-technology, Accessed2022.

[33] Oren, M., Nayar., and S. K., "Generalization of lamberts reflectance model," *SIGGRAPH '94: Proceedings of the 21st annual conference on Computer graphics and interactive techniques*, pp. 239–246, 1994.

[34] *Datasheet and operating guide of fl591fl laser diode driver*, https://www.teamwavelength.com/download/Datasheets/fl591.pdf.

[35] *Data sheet of miniature laser driver mld203p2*, https://www.thorlabs.com/drawings/d91e954b9c85381f-6BEE5301-EE83-F1A0-1FEB1455D7A30213/MLD203P2-DataSheet.pdf.

[36] *Data sheet of miniature laser driver mld203p1*, https://www.thorlabs.com/drawings/d91e954b9c85381f-6BEE5301-EE83-F1A0-1FEB1455D7A30213/MLD203P1-DataSheet.pdf.

[37] *Mounted si photodiode: Sm05pd1a*, https://www.thorlabs.com/drawings/d91e954b9c85381f-6BEE5301-EE83-F1A0-1FEB1455D7A30213/SM05PD1A-SpecSheet.pdf.

[38] *Mounted ingaas photodiode: Sm05pd5a*, https://www.thorlabs.com/drawings/d91e954b9c85381f-6BEE5301-EE83-F1A0-1FEB1455D7A30213/SM05PD5A-SpecSheet.pdf.

[39] S. J., M. S., K. C. V. K., and R. A. Holser, "Application of nir reflectance spectroscopy on rapid determination of moisture content of wood pellets," *Am. J. Anal. Chem.*, 2015.

[40] M. G. [presenter], R. Fedosejevs, A. Sedgwick, and Y. Tsui, "Technology for in-situ real time measurements of solids content in settling tailings," in *COSIA Tailings Project Dissemination Review*, 2019.

[41] Y. Tsui, R. Fedosejevs, M. Gupta, A. Sedgwick, A. Junaid, T. Srivastava, T. K. Sraw, C. Kaur, X. Liu, B. Yu, J. Zhang, and M. Islam, "In situ real time measurements of solids content in settling tailings," 2022.

[42] A. Feng, J. Pan, S. Patel, and D. Sweeney, "Power and communication units for solids content analyzer," 2020.

Appendix A: Codes

This appendix includes the Arduino code for signal channel selecting, the Matlab code for settling tank data experimental results processing.

A.1 Arduino code for signal channel selecting

```
void setup()
pinMode(3, OUTPUT); //INH
pinMode(4, OUTPUT); //C
pinMode(5, OUTPUT); //B
pinMode(6, OUTPUT); //A
pinMode(8, OUTPUT); //INH'
pinMode(9, OUTPUT); //C'
pinMode(10, OUTPUT); //B'
pinMode(11, OUTPUT); //A'

void loop()
digitalWrite(8, HIGH);
digitalWrite(3, LOW);
digitalWrite(4, LOW);
digitalWrite(5, LOW);
digitalWrite(6, LOW);
delay(20000);
digitalWrite(3, HIGH);
digitalWrite(8, HIGH);
delay(10000);
digitalWrite(3, HIGH);
digitalWrite(8, LOW);
digitalWrite(9, LOW);
digitalWrite(10, LOW);
digitalWrite(11, LOW);
delay(20000);
digitalWrite(3, HIGH);
digitalWrite(8, HIGH);
delay(10000);
digitalWrite(8, HIGH);
digitalWrite(3, LOW);
digitalWrite(4, LOW);
digitalWrite(5, LOW);
digitalWrite(6, HIGH);
```

```
delay(20000);
digitalWrite(3, HIGH);
digitalWrite(8, HIGH);
delay(10000);
digitalWrite(3, HIGH);
digitalWrite(8, LOW);
digitalWrite(9, LOW);
digitalWrite(10, LOW);
digitalWrite(11, HIGH);
delay(20000);
digitalWrite(3, HIGH);
digitalWrite(8, HIGH);
delay(10000);
digitalWrite(8, HIGH);
digitalWrite(3, LOW);
digitalWrite(4, LOW);
digitalWrite(5, HIGH);
digitalWrite(6, LOW);
delay(20000);
digitalWrite(3, HIGH);
digitalWrite(8, HIGH);
delay(10000);
digitalWrite(3, HIGH);
digitalWrite(8, LOW);
digitalWrite(9, LOW);
digitalWrite(10, HIGH);
digitalWrite(11, LOW);
delay(20000);
digitalWrite(3, HIGH);
digitalWrite(8, HIGH);
delay(10000);
digitalWrite(8, HIGH);
digitalWrite(3, LOW);
digitalWrite(4, LOW);
digitalWrite(5, HIGH);
digitalWrite(6, HIGH);
delay(20000);
digitalWrite(3, HIGH);
digitalWrite(8, HIGH);
delay(10000);
digitalWrite(3, HIGH);
digitalWrite(8, LOW);
digitalWrite(9, LOW);
digitalWrite(10, HIGH);
digitalWrite(11, HIGH);
delay(20000);
digitalWrite(3, HIGH);
digitalWrite(8, HIGH);
delay(10000);
digitalWrite(8, HIGH);
```

```
digitalWrite(3, LOW);
digitalWrite(4, HIGH);
digitalWrite(6, LOW);
delay(20000);
digitalWrite(3, HIGH);
digitalWrite(8, HIGH);
delay(10000);
digitalWrite(3, HIGH);
digitalWrite(8, LOW);
digitalWrite(9, HIGH);
digitalWrite(10, LOW);
digitalWrite(11, LOW);
delay(20000);
digitalWrite(3, HIGH);
digitalWrite(8, HIGH);
delay(10000);
digitalWrite(8, HIGH);
digitalWrite(3, LOW);
digitalWrite(4, HIGH);
digitalWrite(5, LOW);
digitalWrite(6, HIGH);
delay(20000);
digitalWrite(3, HIGH);
digitalWrite(8, HIGH);
delay(10000);
digitalWrite(3, HIGH);
digitalWrite(8, LOW);
digitalWrite(9, HIGH);
digitalWrite(10, LOW);
digitalWrite(11, HIGH);
delay(20000);
digitalWrite(3, HIGH);
digitalWrite(8, HIGH);
delay(10000);
```

A.2 Matlab code for data processing

```
rawdata = readtable('rawdata.csv');
column = 6
level = rawdata(:,column);
level(1:17,:) = [];
leveldata = level;
interval = 330;
l = size(leveldata);
l = l(1);
count =1;
leveldata = leveldata:,:;
for a =1:interval:l
leveldata(a+3:a+16,1);
```

```
avg(count) = mean(leveldata(a+3:a+16,1));
count = count + 1;
end
plot(avg);
```

Appendix B: Calibration tank results of circuit2

This appendix includes the FFT-C calibration tank results using circuit2 with 1550nm LDs.

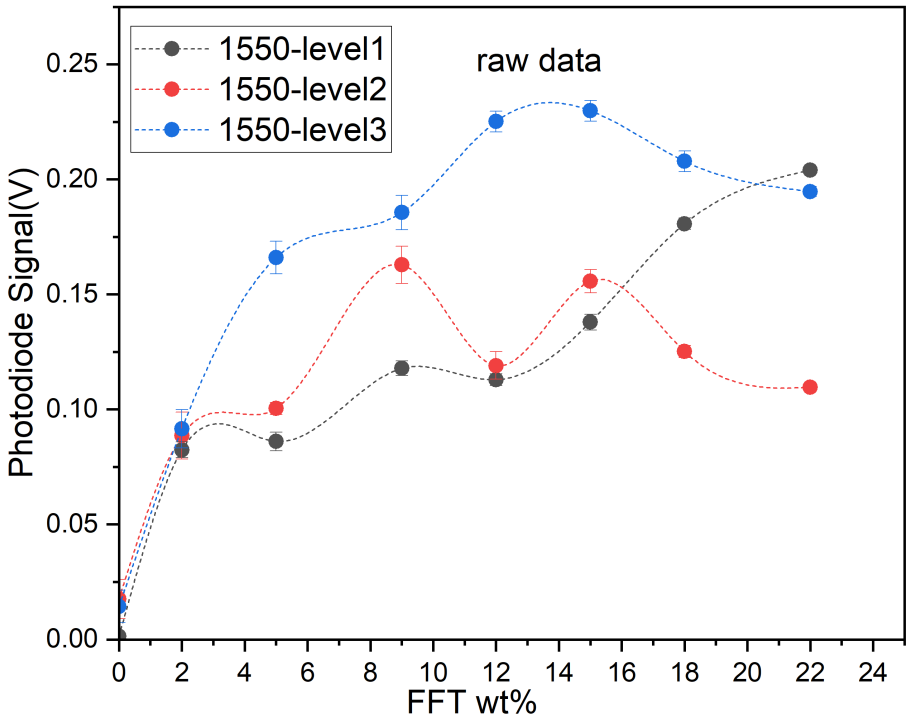

Figure B.1: FFT-C sample calibration results measured at 20°backscatter angle using circuit1 with 1550nm laser diode.